The importance of pore throats in controlling the permeability of magmatic foams

DOI:
10.1007/s00445-019-1311-z

Citation for published version (APA):
Baker, D., Brun, F., Mancini, L., Fife, J. L., LaRue, A., O'Shaughnessy, C., Hill, R. J., & Polacci, M. (2019). The importance of pore throats in controlling the permeability of magmatic foams. *Bulletin of Volcanology*. https://doi.org/10.1007/s00445-019-1311-z

Published in:
Bulletin of Volcanology

Bulletin of Volcanology

The importance of pore throats in controlling the permeability of magmatic foams

--Manuscript Draft--

Manuscript Number:	BUVO-D-18-00145R1
Full Title:	The importance of pore throats in controlling the permeability of magmatic foams
Article Type:	Research Article
Corresponding Author:	Don Baker McGill University Montreal, Quebec CANADA
Corresponding Author Secondary Information:	
Order of Authors:	Don Baker
	Francesco Brun
	Lucia Mancini
	Julie L. Fife
	Alexandra LaRue
	Cedrick O'Shaughnessy
	Reghan J. Hill
	Margherita Polacci
Funding Information:	Natural Sciences and Engineering Research Council of Canada — professor Don Baker
Abstract:	Foam formation during vesiculation of hydrous magmatic melts at 1 atm was studied in situ by synchrotron X-ray tomographic microscopy at the TOMCAT beamline of the Swiss Light Source (Villigen, Switzerland). Four different compositions were studied; basaltic, andesitic, trachyandesitic and dacitic hydrous glasses were synthesized at high pressures as starting materials and then laser heated on the beamline. The porosity, bubble number density, size distributions of bubbles and pore throats, as well as the tortuosity and connectivity of bubbles in the foams, were measured in three dimensions based on tomographic reconstructions of sample volumes. The reconstructed volumes were also used in lattice-Boltzmann simulations to determine viscous permeabilities of the samples. Connectivity of bubbles by pore throats varied from ~100 to 105 mm-3, and for each sample correlated positively with porosity and permeability. Although permeability increased with porosity, the relationship is complex; consideration of the results of this and previous studies of the viscous permeabilities of aphyric and crystal-poor magmatic samples demonstrated that at similar porosities the permeability could vary by many orders of magnitude, even in similar composition samples. More than 90 % of these permeabilities are bounded by two empirical power laws, neither of which identifies a percolation threshold. Comparison of the permeability relationships from this study with previous models (Degruyter et al. 2010; Burgisser et al. 2017) relating porosity, characteristic pore-throat diameters and tortuosity demonstrated good agreement. However, modifying the Burgisser et al. (2017) model by using the maximum measured pore-throat diameter, instead of the average diameter, as the characteristic diameter produced a model that reproduced the lattice-Boltzmann permeabilities to within 1 order of magnitude. Measured correlations between the average bubble diameter and the maximum pore-throat diameter as well as between porosity and tortuosity in our experiments produced relationships that allow application of the modified Burgisser et al. model to predict permeability based only upon the average bubble diameter and porosity. The experimental results are consistent with previous studies suggesting that increasing bubble growth rates result in decreasing permeability of equivalent porosity foams. The effect of growth rate on permeability is hypothesized to substantially contribute to the multiple orders-of-magnitude variations in the permeabilities of natural magmatic samples at similar porosities.

Response to Reviewers:	Please note that in the attached file the Editor's and the reviewers' comments are in italics, quotations from the previous version of the manuscript are in bold, and our responses are in regular text; this file is linked to the submission package but does not print with it. The locations of changes in the revised text are highlighted in the attached file, and the line numbers refer to the version of the manuscript where the changes have been made, but not accepted, so that it is easier to directly compare the previous version of the manuscript to the revised one. Editor's and reviewers' comments: ….. Editor:The reviewers agree that this revised manuscript is improved relative to the original, but that there are still some important issues that need to be addressed. I am recommending moderate revisions, although I do not see the need for another round of reviews. However, I hope that you will address the comments and suggestions provided by myself and the two thoughtful reviews. First and foremost, the manuscript requires a better discussion of how the vesiculation-by-heating experiments presented here can be related to the vesiculation-by-decompression conditions that accompany most volcanic eruptions. This is not just a matter of converting an equivalence between heating rate and decompression rate, but instead requires some assessment of the effect of heating on melt viscosity and, in turn, on the kinetics of bubble growth and coalescence (pore development). Response: The revised manuscript now has a section that implicitly discusses the differences between isobaric heating and isothermal decompression vesiculation experiments on lines 364-418. Another important point relates to the measurement and spatial location of maximum pore throat size. How are pore throat sizes measured? Response: The pore throat sizes were measured using the "concept of a maximal inscribed sphere (Hildebrand and Rüegsegger 1996)" as stated in the previous version of the manuscript (l. 229-230). We have slightly expanded this explanation in the revised manuscript on lines 254-264; additional details are provided in Hildebrand and Rüegsegger. Because these samples can be modeled as random media the location of the maximum pore size does not have to be specified for the type of modeling presented in this research (e.g., lines 361-362 in the revised manuscript). How large a volume needs to be measured to accurately assess the maximum size? Response: This is a very important question; the maximum size of either a pore (vesicle) or pore throat was measured in the central volume of the expanding sample. For any specific sample (chosen from each sample to be most representative of the central volume of the sample) we find the maximum sized objects in it, not in the entire experimental sample. Clearly the sample needs to have multiple bubbles and pore throats within it to be measured and modeled and the maximum size of the pores and pore throats must be significantly less than the volume of the sample. We have checked this and all samples, except possibly the dacite with the highest permeability fit these requirements. The impact of the size of the sample on lattice-Boltzmann permeabilities is assessed in lines 334-355; further details can be found in Bai et al. (2010), which is cited in the text. Isn't the spatial distribution of pore throats important? Response: Porous media are some of the classic examples of random networks in which the pores and the connections between them (pore throats) are randomly distributed (e.g., Stauffer and Aharony 1994). Although locally the locations of pores and pore throats are important, when the sample is large enough the locations do not matter. In this study, the observations of no preferential orientation of pores or pore throats, and that the permeability varies by less than a factor of 2 between the three orthogonal directions, indicates no preferential alignment of pores or pore throats and thus supports the treatment of these samples as random networks. This argument is

presented on lines 356-362 in the revised manuscript.

That is, is the largest pore throat is connected to the porous network via a series of smaller pore throats, then presumably it would be the smallest pore throat in the connected network that would be limiting?

Response: Flow rate control by the smallest pore diameter would occur if the pores are connected in a series. In the samples studied the connectivity is high and there are multiple interconnecting pore throats, so that transport through the pores is a parallel (rather than a sequential) process. In such a case transport appears controlled by the largest diameter pore. We have expanded this discussion in lines 876-892 in the revised manuscript:

Finally, the paper is still very long. Tightening up both the overall structure and shortening the discussion would make this much more readable. As a component of this, the terminology should be chosen carefully. As I comment on below, permeabilities that are described in the text as “determinations” or even “measurements” are actually Lattice-Boltzmann simulations from small sub-volumes. It is perfectly valid to compare these simulations with results from models (e.g., Degruyter, Burgisser). But the do refer to them as simulations and not as measurements, for the sake of clarity.

Response: We have both tightened up the overall structure and reduced the length of the manuscript, as well as changing the terminology as requested. In particular, we have removed both the discussion of Namiki and Manga model from the revised manuscript and the comments on inertial viscosity.

l. 124-127 A comment: permeability anisotropy may also be important in gas loss from volcanic conduits (e.g., Schneider et al., 2012).

Response: We have now referenced the paper by Schneider et al. (2012) on line 819, but in this contribution we are only dealing with permeability in isotropic samples.

l. 145- I infer from Fig. 2 that the sample was allowed to expand freely? This should be stated, as free vs. confined expansion is an important distinction from the perspective of bubble-bubble interaction and anisotropy generation.

Response: The samples freely expanded; this has been explicitly stated in the revised manuscript on line 183.

l. 166-176 See comments above, and of one reviewer, about changes in melt viscosity during heating, which is also relevant to the thermal gradients mentioned in l. 204.

Response: The revised manuscript now has a section that explicitly discusses the differences between isobaric heating and isothermal decompression vesiculation experiments on lines 364-418 that includes a presentation of the changes in melt viscosity and water diffusivity during bubble growth.

l. 204-225 By my calculation, it looks like all of your experiments were at a resolution of 2.89 μm/pixel, or 24 μm3/voxel? Is the criterion of > 2 voxels (>~50 μm3) sufficient to image pore throats in all samples?

Response: Yes, we were able to image all pore throats whose sizes were greater than 2 voxels in the samples. However, small pore throats below the imaging resolution could not be detected.

Another question about resolution: how do the volumes used for the LB simulations compare with the mean and maximum bubble sizes?

Response: With only one exception, the highest porosity dacitic sample, the maximum bubble volumes are less than 6 % of the volume used for the LB permeability simulations. This has been stated in the text on lines 467-470.

It would help to provide a slightly more detailed description of the “inflation of spheres” method. Inflation seems an odd word to use… from an image processing perspective, is this a dilation? It is also a bit difficult to see the difference between Figs. 1f and g… can you provide a quantitative comparison as well as a visual?

Response: We chose the word "inflation" explicitly to imply that the spheres are enlarged isotropically until they touch the walls of the bubble or the pore throat. We did not use the word "dilation" because dilation can be anisotropic. We have now used the phrase "isotropic inflation" because one of the reviewers wondered if the inflation was isotropic (line 271 in the revised manuscript).

l. 264 Define the Betti number

Response: We have deleted use of the term Betti number in the revised text as one of our space-saving modifications so a definition is no longer needed.

The section on Lattice-Boltzmann modeling of permeabilities contains quite a long discussion of Bai et al. (2012); can you shorten to the most salient points?

Response: The discussion has been shortened (lines 334-355 in the revised manuscript).

Figure 2 is not particularly informative (although interesting that the sample maintains sharp edges during expansion), and it is not possible to see the details of bubble growth (e.g., l. 342). My suggestion would be to use fewer images, but to include labels in each image of sample volume and/or vesicularity. Also useful would be a diagram showing the nominal change in melt viscosity over the temperature interval of 600-1100˚C.

Response: We have modified Figure 2 and added vesicularity of the subsample investigated, as well as estimated viscosities (calculated following Giordano et al. 2008) into it.

l. 349 What is meant by "Bubbles coalesced and typically grew to a maximum size, creating a foam of thin-walled bubbles"? Are you simply saying that heating under free expansion creates high vesicularities? I note, however, that the maximum vesicularities reported in Table 2 range from 64-84%, which are not unusually high, with the lower not technically a foam.

Response: Yes, that is what we mean. We have changed our wording, but retain the use of the word foam in some instances throughout the manuscript to describe the samples.

l.356 If surface area is important, did you experiment with different resolutions of tomographic images?

Response: We did not experiment with different resolutions. We used the maximum possible resolution on the beamline in order to obtain the best images possible of the representative sample volumes.

The section on BNDs, BSDs, and PTDs could be condensed.

Response: This section has been condensed, primarily by removing the sentences describing average values in the samples.

I must be missing something… in Table 2, the superscript 1 is supposed to be for the volumes measured, but I don't see any column that reports this; the only reported volumes appear to be those used for permeability measurements.

Response: This was my mistake. I submitted an older version of Table 2 that included other mistakes. The table has been revised in the current version of the manuscript.

l. 368 I don't see the connection between continuous nucleation (during heating) and water content?

Response: There has been some discussion in the literature concerning continuous nucleation versus a single nucleation event in the experimental literature. Because this topic is not particularly important to the study at hand we have removed this sentence to shorten the manuscript.

l. 381-383 Why present mean and standard deviation of bubble sizes when you have already stated that none of the distributions are Gaussian? The mode (or even the median) is probably more useful.

Response: The mean and standard deviation were supplied to provide the reader with a means to compare the current results with those of previous studies (see lines 378-382 in previous version of the manuscript). We have now also provided the median value of the bubble and throat diameters in Table 2. And, we provide all of our measurements in the Supplementary data table so that readers can make their own calculations.

Also important are the volume-based (rather than number-based) distributions (e.g., Klug et al., 2002), as these will give a sense of the samples where a few large bubbles contribute much of the volume; this may be important for thinking about sub-sampling for permeability calculations.

Response: We certainly agree that volume-based distributions such as those used in Klug et al. (2002), are extremely useful. However, in the context of this manuscript we do not think that their inclusion would help the reader better understand the experiments, and the discussion of volume-based distributions would add unnecessary length to the manuscript.

Additionally, for both number- and volume-based distributions, I find it easier to compare samples if you put several together on a cumulative distribution plot, rather than numerous separate histograms. Cumulative distributions also circumvent problems of binning, and allow direct comparison of median values.

Response: We have now put the cumulative distributions back into Figures 3-6 because we agree that the cumulative distributions circumvent the problems of binning. We did not include a single plot with the cumulative distributions in this manuscript previously because we did not concentrate our investigation on the changes in the distributions, and a single plot containing all of the cumulative distributions is extremely "busy". Because all of the data are included in the Supplementary Materials the reader can create such a plot if they are interested.

l. 402-412 I'm a bit confused. You explicitly state that you avoided counting "anomalously" large bubbles, and then focus on the large number of small bubbles (which, by definition, are the only ones you are counting?)

Response: We have rewritten these sentences to stress that we chose representative volumes of the sample near its the center and avoided regions with anomalous bubbles that were found near sample edges (lines 516-520 in revised text).

l. 445 Your reported β values are very high, which presumably relates to the volume normalization? I don't have an intuition for this number (or its purpose)… average coordination numbers of 4-6 are interesting and actually lower than expected theoretically for uniform spheres (which should be 12). I am a bit puzzled by the maximum number of 600, however… is this an artefact of the processing or is it simply one very large bubble in a mesh of tiny bubbles?

Response: The high numbers come from large bubbles with a mesh of interconnected tiny bubbles. A two-dimensional example of this can be seen in Figure 1. See lines 576-578 of the revised manuscript.

l.470-487 You are mixing apples and oranges here. Relevant for your analysis are samples that have experienced only simple vesiculation histories, in the absence of abundant crystals or bubble deformation. The low percolation value from Saar and Manga, in contrast, is a sample from a basaltic lava flow that is both highly crystalline and has lost most of its original porosity. What is the rationale for extending even your andesite line to infinitely small porosity (which would require crack-like geometries), rather than assuming that samples with lower porosities are actually not permeable (that is, lack a connected bubble network)?

Response: As stated on lines 482-483 in the previous version of manuscript and in multiple places in the revised manuscript, the critical porosity threshold for any specific sample is unknown. This is due to the size distribution and shape of the vesicles (mentioned on lines 479-480 and more thoroughly discussed on lines 575-600 of the previous version and lines 602-612 in the revision). Because the critical porosity threshold is unknown for our samples we chose to use an empirical fit as done in some previous studies (see lines 484-485 of the previous version and lines 602-612 in the revision) and acknowledge that other studies have estimated the critical porosity and used it in their fitting (lines 485-487 in the previous version and 606-612 in the revision). In the previous version we also included a fit with a critical porosity to the andesitic data (see line 491 of the previous version) and keep that fit in the included revision (line 616).

As mentioned above, I found the discussion of Fig. 7 confusing, in that you discuss simulated porosity-permeability relations as if they were measured. Be clear about this, especially as this section follows a long section on measurements, and you don't let the reader know that you are now switching to LB simulations.

Response: We have now reworded the revised version to make clear in the discussions of Figures 7 & 8 that the reported permeabilities come from lattice Boltzmann simulations.

Regarding Fig. 8; again, I would suggest being more discriminating here, so that you make your comparisons only with crystal-poor samples that have experienced a simple vesiculation history (which is the more appropriate comparison for your samples).

Response: Following this suggestion we have modified Figure 8 to present only aphyric-to-crystal-poor samples. The changes in Figure 8 have no effect on the conclusions reached in this study, although the power-laws that encompass the measurements change from when both aphyric-to-crystal-poor samples and crystal-rich samples are included.

Discussion – at almost 19 pages, the discussion is too long, even for someone like me who is interested in the topic!

Response: We have significantly shortened the discussion in the revised version of the manuscript and removed the discussion of the Namiki and Manga model. The discussion has been reduced to 11 pages in the revised manuscript.

I would start by shortening the section on permeability "determinations". This is an odd word, because it sounds like you measured them… I would use the word "simulated".

Response: We have shortened the section and changed our wording to make clear that our permeabilities are the product of lattice Boltzmann simulations.

I don't know the Bai et al. paper well so I won't comment on these data. However, the highly variable permeabilities at very low porosities in the Saar and Manga data set are certainly crack-dominated, as mentioned about (they are completely solidified and mostly degassed lava flow interiors). Similarly, as we have pointed our (Rust and Cashman, 2004; Wright et al., 2009; see also Wright et al., 2014), the permeability of effusive samples and/or densified (domes, flows, welded tuffs, etc.) samples is the end result of both vesiculation (sometimes in the presence of numerous crystals) and compaction, gas loss (densification) and, sometimes, later crack formation. For this reason, it does not make sense to fit them all to the same porosity-permeability law. Finally, the hard sphere percolation concept neglects the fact that bubbles become permeable either by deforming (as in tube pumice) or by coalescing; the latter requires melt film thinning and rupture, which will occur at rates that depend on melt viscosity and the pressure differential across the melt film (rate of bubble-bubble expansion). Setting out these general constraints at the beginning of the section would allow you to reduce, substantially, the amount of time spent discussing individual sample suites.

Response: We have followed these suggestions in the revised version of the manuscript by only discussing aphyric-to-crystal-poor samples and avoided “effusive samples and/or densified samples”. We also do not think that the hard-sphere percolation threshold is important, but think that the readers need to be informed of its existence so we have kept it in the revised version.

The section on model comparisons could also be shortened, as there are places that are repetitive.

Response: We have shortened the section on model comparisons.

l. 657 Define “channel circularity”. To me this is a 2D parameter based on a comparison with a circular cross-section. How, then can this have the value of 10? What sort of geometry does this imply (if it is even physically reasonable?)

Response: Channel circularity was defined in the previous version in Equation 4 (Line 658 and in the revised version in Equation 7, line 841-844). It is defined by both the equivalent circle radius of the throat, r, and its major axis, l, following Degruyter et al. (2010), so it is basically a 2D parameter measuring deviations from circularity.

Note that for a major axis 4 times the equivalent circle radius the value of χ is 16. Also, we now discuss the value of 10 as a functionof 2 x a fitting constant of 5.

l. 676-678 Here again you refer to simulation results as “measurements”. As noted above, this would be clearer if you used the term simulation.

Response: We have made the changes to indicate the permeabilities are from lattice-Boltzmann simulations.

l.682-734 This is an excessively long paragraph. L.682-692 could be omitted, as a start.

Response: We have shortened this paragraph greatly in the revised manuscript (Lines 743-774), but think we need to include the description of percolation theory in the beginning of this paragraph to help the reader better understand the discussion.

Explain how the largest pore throat can dominate permeability. As noted above, it doesn’t matter how large the PT is, if it is connected to the larger network by only tiny PTs. Indeed, we know that permeability is not controlled by the largest bubble. The more common way to think about this is that the largest(most permeable) pathway dominates.

Response: Our experiments, with their high connective densities, provide evidence the the bubbles in the samples are multiply connected and that therefore they can be modeled as parallel circuits. In such a parallel circuit the transport will be dominated by the pathways of lowest resistance, the largest pore throats. (see lines 876-892 in the revised manuscript)

Figure 9c. Again, I don’t know the Bai data very well but they do not show a very convincing fit (wrong shape?)

Response: We agree that the Bai et al. data do not show a convincing fit and wish that the Bai et al. data did fit the model better. However, they are some of the few data to which we can compare our model, and we think it important to present the comparison between the model and the Bai et al. (2010) data. In the previous version of the manuscript we made the quantitative comparison between the model and data and commented upon its limitations (Lines 718-728 in the previous version and lines 914-923 in the revised version). We specifically stated that the model accuracy was degraded when using equation 6 to estimate the permeability and demonstrated that the predictions were only accurate to approximately 1 order of magnitude.

l.729 The caveats are good but belong earlier!

Response: We moved the caveats to an earlier position in the discussion (lines 867-875 in the revised manuscript).

l. 748 I would expect a relation between bubble growth rate and pore throat size simply on the basis of the relation between bubble growth rate and ∆P (e.g., Klug and Cashman 1996).

Response: That certainly makes sense, but unfortunately our results are too limited to test this hypothesis.

Omit the discussion of inertial permeability, and reference Zhou et al. (2019) instead.

Response: This has now been done in the Introduction where we also discuss Polacci et al. (2014) who found the same relationship as Zhou et al. (2019). Please see lines 135-139 in the revised manuscript.

Again, it would make more sense to use a porosity-permeability model based only on expanding (vesiculating) crystal-poor samples in the Namiki and Manga model, rather than muddying the waters with all measured data. Additionally, with the very slow rates of magma ascent used, both two-phase flow (in low viscosity melts) and loss of gas to walls rocks (e.g., Schneider et al.) could be important.

Response: We have now dropped this discussion. Note that our bounding values for the crystal-free to crystal-poor permeability-porosity data are not significantly different from found when crystal-bearing samples are also used for the fit.

I also have a question about the modelling, particularly with reference to Fig. 10. The patterns of gas flow shown here, with peak Vgas/Vmelt for basalt at 7km depth and 12km for rhyolite, do not make sense with respect to the stated range of water solubilities (70 MPa and 180 MPa; which are equivalent to 2.8 and 7.2 km for a generously low crustal density of 2500 kg/m3). Is this all a function of reduced density in the conduit because of the steady state assumption?

Response: Yes, the density becomes quite low because of the bubbles in the magma.

It would be helpful to include a plot of exsolved gas fraction as a function of P. Also, you might state that the form of the Vgas/Vmelt curve is a direct reflection of the assumed shape of the permeability curve, which increases by several orders of magnitude between 0.0 and 0.07 volume fraction porosity.
As you note, however, if this were actually the case, then we'd never see bubbly magma reach the surface. This does not necessarily mean, however, that your average permeability curve is correct. A more plausible explanation for the abundance of bubbly samples of all compositions is the existence of a porosity threshold for the onset of permeable gas loss.

Response: The Vgas/Vmelt curve is a direct reflection of the assumed permeability curve shape, which is why only the highest values of permeability cross the threshold for potential gas loss. What is interesting is that irrespective of the exact type of porosity/permeability relationship, the threshold is crossed only for the most permeable magmas and this permeability threshold is approximately 1013 m2 (see Figs. 10 and 8 in previously submitted version of the manuscript). The Namiki and Manga model is very interesting and predicts very interesting magma behavior that is far beyond the scope of the current manuscript. Therefore, because we cannot fully discuss the model under different porosity-permeability conditions without making the manuscript substantially longer (e.g., comparing magmas with and without porosity thresholds for permeable behavior), with regret that we have dropped the Namiki and Manga model from the revised manuscript.

Klug, C., Cashman, K.V, Bacon, C.R. (2002) Structure and physical characteristics of pumice from the climactic eruption of Mt. Mazama (Crater Lake), Oregon. Bulletin of Volcanology 64:486-501.

Schneider, A., Rempel, A.W., and Cashman, K.V. (2012) Conduit degassing and thermal controls on eruption styles at Mount St. Helens. Earth and Planetary Science Letters 357-358: 347-354.

Wright, H.M.N and Cashman, K.V. (2014) Compaction and gas loss in welded pyroclastic deposits: evolution of porosity and permeability in the Shevlin Park Tuff Geological Society of America Bulletin 126: 234-247. doi:10.1130/B30668.1

………

Reviewer #3: Review of "The importance of pore throats in controlling the permeability of magmatic foams" by Baker and others.

This paper presents results of new incremental heating vesiculation experiments of crystal-poor volcanic samples. The samples are progressively imaged using three-dimensional tomography in order to characterize the evolution of pore size, connectivity and volume through time. The authors present the results of image analyses, permeability modeling, comparison with published measurements for other volcanic samples, and apply the results to models of syn-eruptive conduit flow.

The one major shortcoming of this paper is the lack of direct connection between the experiments presented herein and their applicability to natural systems. Furthermore, although the authors repeatedly suggest that porosity is not the only control on permeability, the discussion applies a single fit (and bounding upper and lower limits) between porosity and permeability to all data from the literature. No attempt is made to separate out subgroups lumped according to hypothesized controlling factors (bubble growth rate, crystal content). As such, the application of the final model from Namiki and Manga (2008) feels disconnected from the experimental results presented herein.

Thanks for the opportunity to review,
Heather Wright

Please find detailed comments below and new plots created from data in Table 2 presented in the attached excel file.

Line 75. Loss of gas can occur through porous networks or via two-phase flow. Perhaps reword this statement by saying 'gas loss' and removing the porous network portion of the sentence.

Response: We have changed the sentence following the reviewer's suggestion (Lined 82-83 in the revised manuscript)

Line 80. This is true only when bubbles cannot move through the melt on their own. As above, two-phase flow can also prevent pressurization that causes explosions.

Response: We have slightly changed the sentence in question to: “Relatively impermeable magmas can lead to violent eruptions whereas permeable ones may not (Sparks 2003; Mueller et al. 2005, 2008).” on lines 87-88 of the revised manuscript.

Line 89. This sentence is vague. How about: 'proposed separate power-law relationships"…

Response: In order to condense the manuscript this line was deleted from the revised version.

Line 99. Change number of pore throats to number density of bubbles?

Response: Line 98 of the previous manuscript (which is part of the same sentence as line 99) mentions the importance of bubble size distributions and we decided to keep the phrase “the number and size of pore throats” because of their importance in the understanding of the permeabilities of the studied samples”.

Line 134. Is there any additional information about the chosen samples? Where is the MORB sample from? Are the Atkan andesite and dacite samples from historic eruptions? Were the samples low-crystallinity or high-crystallinity samples?

Response: We do not have data on the exact location of MORB. The Atka andesite and dacite are not
from historic eruptions and we do not know their exact localities. We also do not have measures of the crystallinities of these samples before totally melting them during the high pressure experiments reported in the manuscript.

Line 221. The precision of what method of vesicularity measurements? What sample is the 0.503 porosity measurement from?

Response: We have now specified that at this point in the manuscript we are discussing the precision of vesicularity measurements using X-ray microtomography. Baker et al. (2011), specifically investigated the reproducibility of porosity measurements using X-ray tomography, and the sample used in that study is unrelated to those studied in this manuscript. We have rewritten this sentence to make this more clear (lines 245-248).

Line 223. Why do you expect similar uncertainties? Vesicularity is dominated by large bubbles. Pore throat numbers and sizes are not necessarily dictated by largest bubbles.

Response: Similar uncertainties are expected because the same techniques are used for the measurements and in many cases the sizes are similar. We have rewritten this sentence to make this more clear (lines 250-251).

Line 239. How are branch diameters calculated/estimated? If I understand correctly, branch diameter = pore throat diameter. In 1h, each branch looks like a line with single pixel width. Are pore throats define by maximum inscribed cylinders that connect spheres?

Response: Figure 1h only shows the skeleton, which by definition is 1 voxel in width. The pore throat diameters are defined by the diameter of a sphere that can be fit through their narrowest part. We do not define the length of the pore throat so the idea of fitting them with a cylinder is not valid We have explained our techniques more fully on lines 254-259 of the revised manuscript. Please also see the caption to Figure 1.

Line 240. Can a cartoon be added here to help the reader follow this discussion? How does pore shape affect the overlapping sphere distinction? What if pores are non-spherical? Are all pores that have begun to coalesce then grouped as a single pore?

Response: We have not included a cartoon, but in the revised text refer the reader to Figure 1 in the revised text (lines 270, 274-275). The steps in this process are graphically shown in the example presented in Figures 1d-1h.

Line 243. What is the formula for degree of inflation? What does 'the amount of inflation can be controlled' mean? Is the inflation degree a proxy for the size of bubble centered on each node? Is this inflation process isotropic?

Response: Spheres were inflated isotropically; this is now stated in the revised manuscript (line 271). The papers cited in this section of the manuscript provide many more details of the techniques used for the measurements used in this study than can be included in this manuscript.

Line 247. What does maximum inflation mean? Further, you state that "this parameter only weakly affects the computed values"… computed values of what?

Response: Maximum inflation is largest sphere that would fit the bubble, but this size sphere can underestimate the number of bubbles (as written on lines 245-246 on the previous version of the manuscript), so typically a value less than the maximum is used, as explained in the manuscript. The "computed values" are those of the bubble and throat numbers and sizes. This is now stated in the revised text on lines 257-258.

In Figure 1h, it looks like the use of spheres that completely fit within bubbles creates

	underfit bubble sizes. So bubble sizes are minima? But pore throat sizes may be maxima? (Line 252). Is that correct? Response: No, bubble sizes fit to the maximum of the pore and so are the average pore throat sizes because the same techniques are used to measure both (see lines 227-230 in the previous version of the manuscript and lines 255-259 in the revised version). This is a standard technique . We have changed the sentence on lines 255-259 to make this more clear. All details of the techniques are provided in the reference at the end of the sentence in the manuscript (Hildebrand and Rüegsegger 1997), which is a often-used reference for such measurement techniques (1435 citations as of 20 April 2019). Another of the standard references cited in this portion of the text is Lindquist 2002 (45 citations). Line 277. This may be simpler to read if written in equation form. Response: Great idea. We have made the change (line 309-313 of revised manuscript). Line 296. In the Bai et al. study, it appears that the difference between modeled and measured permeability is minimized at <65%. Where does 50% come from? Response: We only chose 50% for comparison because we thought the reader might be interested in the comparison of measured and modeled permeabilities in the exact center of the permeability range. Obviously, this comparison is confusing the reviewer and will probably confuse many readers so we have deleted the sentence. Line 298. From Bai et al. "The ability of simulations to predict the macroscale Darcian permeability is limited by two independent characteristics. The first is the intrinsic grid resolution, as measured by the physical voxel size a with respect to the characteristic length of the pores (e.g., as determined by bubble size, surface curvature and surface roughness). The second is the physical sample size (quantified by the product of the number of lattice points along each edge NL and the voxel size a), with respect to the geometrical correlation length (e.g., as determined by bubble connectivity and volume fractions)". This statement suggests that the important parameter is the ratio of voxel edge length to edge length of subvolume with respect to geometrical correlation length, essentially a measure of sample heterogeneity. How does that play in here? Response: The intrinsic grid resolution of these measurements is at least as fine as that used in Bai et al. (2010) because the of the higher resolution imaging and, in most cases similar ranges of bubble sizes and sample sizes used for lattice Boltzmann simulations. Additionally, the mean bubble diameters in this study are similar, or smaller, as those measured in Bai et al. (2010), indicating that the geometrical correlation lengths in both studies are similar. Therefore, the arguments in this section of the manuscript support the use of lattice Boltzmann permeabilities based upon the findings of Bai et al. (2010). Please also note that, following the Editor's suggestion, this section of the manuscript has been significantly condensed in the revision. Line 310. Even if there are no anomalously large bubbles, isn't the controlling factor the range in bubble size distribution between subvolumes? Response: One of the controlling factors is the range in the bubble size distributions between different subvolumes, but the importance of pore throat size distributions is stressed in this manuscript. Please note that in order to save space this sentence has been deleted in the revised manuscript. Line 315. In order to apply the test for effect of lattice size used in Bai et al. 2010, don't the geometrical correlation lengths need to be similar? Is that so? Response: Yes, please see response above to comment on line 298. Line 319. Does no significant difference with respect to orientation mean that permeability values were within a factor of 2 of each other? Factor of 3? Response: We have explicitly state what we mean by a “significant” difference, a

factor of 2 on line 358 of the revised manuscript.

Line 327. Does this mean that there was a delay? Was the delay due to heating time? Or was there a further delay after the sample reached Tg?

Response: We could only estimate minimum glass transition temperatures at the heating rates used for these experiments. We have changed this discussion concerning nucleation delay in the revised manuscript (lines 438-442)

Line 329. What is 'onset of glass transition temperature', do you mean simply 'glass transition temperature' or onset of ductile behavior?

Response: The glass transition does not occur at a single temperature but over a range of temperatures that is influenced by the heating, or cooling, rate (Moynihan et al., Journal of Physical Chemistry, 1984, 78:2673-2677; Giordano et al. 2005—reference in the manuscript). The onset is the first evidence of the glass transition during heating as shown in Giordano et al. (2005--reference in manuscript). We have referenced Giordano et al. (2005) after use of this terminology in the manuscript (Line 428)

Line 362. Put in a distance here…? How many um?

Response: We have now put in the approximate distances away from the edges. See line 466 of the revised manuscript.

Line 365. This is true for each individual sample, not for aggregate of samples.

Response: We have now started this sentence with the words “In general, in each sample the ”. Line 470 in the revised manuscript.

Line 400. Perhaps add a clause to the beginning of this statement, like "If the 2 samples can be thought to represent points on a single evolutionary trend". But note that bubble size doesn't even increase between basaltic runs (see graphs in my attached excel file).

Response: We have added the suggested wording (line 513-514 in the revised text). We agree that the bubble size does not increase between the two runs, in fact the maximum bubble size and the average bubble size decreases as shown in Figure 3a.

Line 418. "evenly distributed" meaning what?

Response: We have rewritten the sentence on this line to make the meaning more clear (lines 534-536 of the revised manuscript).

Line 422. Using a single bubble as indicative of process is less convincing than multiple… can you broaden the size bin to <15 um?

Response: We prefer to keep our bin size at approximately the same value as the imaging resolution. However, we agree that one bubble is not convincing (which is why we specifically stated that the interpretation was based upon one bubble in the previous version of the manuscript). We have slightly modified the sentence to indicate that the one bubble “suggesting continuing bubble nucleation” (line 539-541 of the revised text).

Line 425. Is this the spatial density?

Response: Yes it is because the figures are bubble number densities. To make our meaning of the sentence more clear we have added “in the same sized volume” to the sentence (line 543).

Line 505. What is the uncertainty on permeability measurements? Have you tried calculating permeability of 2 subvolumes in the same sample in order to characterize variability? Is the difference between these permeabilities actually 'significant'?

Response: Our uncertainties in the permeability measurements are discussed on lines 348-352 of the revised manuscript. We have not calculated the permeabilities on 2 subvolumes from the same sample because our goal was to fully characterize the subvolumes we thought best represented each sample's center, not investigate the variations in the sample properties (see lines 205-206 in the previous version and lines 230-231 in the revised manuscript).

Line 507. Why surprisingly?

Response: We wrote “surprisingly” because the lowest porosity dacitic foams display lattice Boltzmann permeabilities similar to the andesites but the two highest porosity ones do not (see Figure 7). We have deleted the word “surprisingly” from the revised text (line 637).

Line 515. Incomplete sentence fragments. This paragraph from Line 510 on is discussion and should be removed from this section.

Response: This “paragraph from Line 510” presents our observation that viscosity does not appear to simply control permeability at equivalent porosities. We have moved this paragraph into the beginning of the Discussion section (Lines 669-676 in the revised version).

Line 519. This paragraph is the place for general observations that could be displayed in figures. For example, in single sample experiments as average bubble sizes increase, pore throat increases, in some cases linearly (see andesite sample for example). In general, pore throat diameters are about half the diameter of bubbles (using values from Table 2, see excel file). What are the implications of this relationship? Figure 1h doesn't seem consistent with pore throats being half the diameter of bubbles though…

Response: We prefer to keep the simple summary paragraph at the end of the “Results” section on lines 519-527 of the previous manuscript. We don't want to discuss the average bubble sizes and pore-throat diameters because we don't think the averages are meaningful and only included them so that readers can compare those values with similar values published in other studies. Figure 1h does not present all of the pore throats found throughout the sample, which is why the average pore-throat diameters do not appear to be ½ those of the bubbles.

Line 532. Mention the other controlling variables here that you discuss later.

Response: We have done this in the revised text (lines 663).

Line 536. Be clear here that you are discussing experimentally reheated aphyric basalts and dacites, not basaltic and dacitic eruptive products in general.

Response: This line has been deleted in the revised text.

Line 546. The previous discussion does not address the fit of new data to power-law relationship in general. The dataset presented here appears to follow a non-power law trend. In the attached excel file, an exponential fit to the andesite porosity-permeability appears to fit the data better. Why would that be? Is it due to experimental reheating in contrast to natural decompression? Note that other experimental reheating of clasts has led to bubble collapse in other experiments (Kennedy et al. 2016).

Response: We agree with the reviewer that the andesitic data can be better fit with an exponential relationship, but there is no theoretical foundation of which we know to support such a fit. On the other hand there are theoretical foundations for a power-law fit and that is why we chose such a fit. We are aware of the Kennedy et al. study on the collapse of porous samples, but think that discussion of it will not significantly enhance this manuscript and will unduly lengthen the manuscript.

Line 573. "appears to account for…" - can you quantify this relationship instead? Use a plot of BND?

Response: No, we cannot quantify the relationship between the high bubble number and pore throat number densities of the trachyandesitic sample with a porosity of 0.35 in any meaningful way. However, we do present the BND and the PTD in Table 2 and display the size distributions in Figures 5a and 5b of the manuscript. Note that this sentence has been deleted from the revised manuscript.

This section is verbose; shortening the text would add clarity.

Response: The section has been shortened.

Line 575-600. Repetitive of the section at Line 475; simplify and condense. Do you have data to support determination of percolation threshold?

Response: We have modified this section in response to this comment, but think that the discussion of percolation theory and its predictions of interconnectivity of objects is needed. The data for the determinations of the percolation threshold of random objects in 3 dimensions is provided in the references provided in this part of the text. Our studies have not identified a percolation threshold in the samples investigated; all of our experimental samples are permeable, with the exception of one sample containing a single bubble and another whose permeability could not be measured due to its extremely fine structure. However, we reference other studies of permeability in magmatic foams that have found percolation thresholds in both the previous and revised version of the manuscript.

Line 581. "statistical nature of percolation threshold" - what does this mean?

Response: Mathematically, true percolation thresholds are only exact for infinite systems. Finite systems can display variations about these thresholds (as discussed in the references on line 582 of the previous version of the manuscript). We have modified this sentence to make this more clear (Lines 747-751 in the revised text).

Line 606. I don't think you can generalize about basaltic bubble growth from these four distinct runs (as in attached excel sheet that shows no bubble size pattern between the 4 volumes). This is an over-interpretation of this increase.. delete Lines 606-612?

Response: We think that it is important to discuss these experimental results on the basaltic bubble growth and we conclude this paragraph by stating that we do not think the permeability increase between 0.5 and 0.55 porosity seen in the basalts is significant, so we are in agreement with the reviewer. We also note that while the mean bubble sizes in experiments at 0.5 and 0.55 are similar, the bubble size distribution changes significantly (Fig. 3a).

Line 622. Again, this could be combined with discussion above and shortened significantly. If your data does not add to the discussion - delete?

Response: We have made the combination as suggested by this reviewer (new version on lines 731-742).

line 692. Delete sentence "Such a calculation…" - unnecessary.

Response: We have removed the sentence and modified the previous on slightly (Lines 883-887)

Line 728. Add demonstration of the improvement of this model over the DeGruyter or Burgisser models for all of the samples plotted here (Fig. 9C).

Response: We have modified the text above line 728 in the previous version of the text to indicate that our quantitative comparisons are for all of the samples, except for when explicitly stated otherwise (Lines 920-923). We do not have the data for the Bai et al. (2010) samples to make a comparison with the Degruyter et al. and Burgisser et al. models. We have now added a sentence comparing the results of this model to the results reported by Burgisser et al.

Line 732. Why 0.3?

Response: We chose 0.3 because it is the sphere percolation threshold and have now specified the reason this in the revised manuscript. This paragraph has been moved to earlier in the section following the suggestion of the Editor (Line 872).

Line 738. You say that you concur; on what basis? Or perhaps rephrase.

Response: We have rephrased this sentence. Our reasons for concurrence are detailed later in the same paragraph (line 937-942 of the revised manuscript).

Line 749. Again, without an estimate of uncertainty of your permeability calculations, the relative difference between samples is difficult to characterize.

Response: The uncertainties in the permeability calculations were stated in the experimental techniques section (lines 315-317 in the previous version of the manuscript) and in this new version (lines 348-352). Additionally, the caption to Figure 7 states that the permeability uncertainties are “typically the same size, or smaller than, the symbols”.

Line 757. What composition is this melt film thickness threshold estimated for? And is that for crystal-free melt?

Response: We have specified that the melt composition was rhyoltic in the revised text (line 958 in the revised text).

Line 771. Perhaps 'compared' is more apt than 'correlated' here… several authors examined covariations between the two parameters in order to better understand the role of path effects on permeability.

Response: This section on inertial permeability has been deleted. Nevertheless, we think that because the “earlier” studies produced mathematical relationships between viscous and inertial permeability the use of the verb correlated is correct.

Line 774. Is it only pore shape and size? Could it not also be connectivity?

Response: This line (entire section) has been deleted from the revised manuscript

Line 777. What composition of pumice? Crystal-rich or crystal-poor?

Response: This line (entire section) has been deleted from the manuscript.

Line 783. As above - is that for all data? Composition? Crystal content?

Response: This line (entire section) has been deleted from the manuscript.

Line 793-7. It's not clear why these sentences are here. Inertial permeability is not considered in modeling later in paper. Perhaps remove these sentences and justify lack of inertial permeability in models.

Response: This line (entire section) has been deleted from the manuscript.

Line 847. Again, why use all data lumped together? You state earlier that there are many controls on permeability, including crystal content and bubble growth rate. Given these variations, why not simplify the discussion in this paper and focus solely on aphyric samples with bubble growth rates that you think are similar to your experiments?

Response: This line (entire section) has been deleted from the manuscript. In the revised manuscript we only used aphyric-to-crystal-poor samples.

Line 869. How do these results present an improvement over the Namiki and Manga (2008) conclusions? What is the take-home message from using different porosity-permeability relationships than the Rust and Cashman formulation?

Response: This line (entire section) has been deleted from the manuscript. In the previous version of the manuscript we used the model of Namiki and Manga to demonstrate to the reader that only high-permeability magmas would be expected to lose their driving gas and instead that most magmas would retain it. This was not done by Namiki and Manga. The difference from the Rush and Cashman formulation is that the equations provided in the manuscript demonstrate the wide range in permeability possible at a single given porosity.

Line 885. This introductory sentence to your conclusions is in contrast to your application of general porosity-permeability relationships that encompass all data from the literature, without separating datasets based on your assessment of the factors that control permeability most strongly.

Response: Our application of the general results was not to demonstrate that they could be applied to any specific magma, but instead to show that they constrained the range of possible permeabilities at any specified porosity. In the previous version of the manuscript we used the model of Namiki and Manga to demonstrate to the reader that only high-permeability magmas would be expected to lose their driving gas and instead that most magmas would retain it.

Line 891. This study does not prove a primary bubble growth rate control on permeability.

Response: We have changed this line to state that our results "are consistent with" (line 1093 in the revised manuscript).

Line 896. Is this a remarkable finding of the original Namiki and Manga paper or one asserted for the first time here?

Response: This is a remarkable finding of this work. But we have deleted this line because we no longer discuss the Namiki and Manga model in the revised manuscript.

Table 2. Note that average bubble diameter and average throat diameter for dacite samples are the exact same numbers - one of the columns must be incorrect for dacite samples?

Response: Yes, this was an error that has been corrected and for which I apologize.

Figure 1. Add a scale bar parallel to the front face of imaged volumes.

Response: Done

References:
Kennedy, Ben M., et al. "Surface tension driven processes densify and retain permeability in magma and lava." Earth and Planetary Science Letters 433 (2016): 116-124.

…..

Reviewer L. Chevalier
Dear editor,
I have carefully read the paper from Baker et al., and detail in the following letter my comments and
suggestions on their work. I hope this will help you to decide whether it should be published in the Bulletin of Volcanology.
The work presented in this paper aims at better understanding the diversity of permeability-porosity relationships from the analysis of the foam structure for samples of basaltic to dacitic compositions. In-situ micro-tomography scans of vesiculating basaltic to dacitic foams were analyzed for characterizing the foam structure, and used for estimating the samples permeability from lattice- Boltzmann flow simulations. The resulting data provide the chance to follow the evolution of the foam structure and sample permeability with time for these different compositions, which would be of great interest to the readership of the Bulletin of Volcanology. The analysis of these data

highlights the dominating role of large pore-throats in permeable flow. The study also supports the idea that the bubble growth rate impacts significantly the development of permeability. Readers interested in magma permeability development and degassing processes will be particularly interested in these results. Finally, the study provides results from a numerical model that demonstrate that only the most permeable magmas would be able to lose gas while ascending in the conduit. This is of high interest to readers interested in understanding the evolution of eruption intensity and its link with gas loss.

Since I got the chance to review a first version of this paper about a year ago, I could notice important changes and improvements in the paper:
– The methods section gained a lot in clarity and precision, and is now very easy to read. The results section and the first parts of the discussion were also intensively revised.
– Although the importance of pore throats for understanding the porosity-permeability relationship remains a result of first importance, it is now suggested that the maximum pore- throat diameter, rather than the cumulative pore-throat area, should be used for estimating permeability.
–The influence of the melt composition on permeability development became of minor importance in this new version, and bubble connectivity is much less highlighted.

In general, the research is presented in a clear and accurate way, with developments of high interest and potentially high outreach. I feel, however, that the soundness and coherence of the article could be improved to emphasize and strengthen the ideas developed here, and increase its impact in the following way:

1.Considering the important changes in the paper, I think that the introduction should focus more on the link between foam structure and permeability, and less on the question of composition, which looks to be no more priory in the rest of the article.

Response: We have made the suggested changes in the Introduction (lines 98-106 in the revised manuscript).

2.The experimental procedure, which provides the exiting possibility of following permeability evolution with time, would worth some more discussion to highlight its complementarity and differences from the more common decompression experiments.

Response: We have added an entire new section comparing our isobaric heating experiments to the more usual isothermal decompression experiments (lines 364-418)

3.Using the maximum pore-throat diameter as the characteristic diameter for permeability raises some concerns to me that I detail below. In my opinion, some questions need to be answered and discussed to strengthen this interpretation of the data and its future impact in the community.

These main comments are detailed below, and other comments and suggestions are listed in the following pages. Overall, I think that this paper, providing some modifications, has the potential to be a great contribution to the understanding of magma permeability evolution. I therefore
recommend considering it for publication after a moderate revision.
Laure Chevalier

Main comments
Introduction

Considering the changes made in this new version of the paper, I think that the introduction needs some adaptation to refocus on the message delivered in this paper and emphasize its importance. Although the introduction addresses the very interesting question of the influence of melt composition, it is no more a priory result in this new article version (see the other comments section below). Conversely, the influence of the pore-throat maximum diameter, which is a key result, is emphasized in the introduction. I think that focus should be redirected to introduce and emphasize the message delivered in the article. Besides, a review of the influence of porous network parameters in permeability development would strengthen the introduction of the work on foam structure presented here (most of the relevant references are already cited in the article).

Heating procedure for bubble growth

With increasing heat, melt viscosity decreases. Lindoo et al. (2016) conclude from experiments using various melt compositions that viscosity has no effect on the percolation threshold, but may significantly impact permeability. Melt viscosity evolution with heating raises some questions on the experimental procedure that would worth some discussion:

– Could you estimate the influence of this viscosity evolution on bubble coalescence and permeability development along with porosity increase ? Does the bubble growth rate increases as the temperature increases ? Could you estimate the relative importance of such viscosity changes (after vesiculation starts), compared with differences of viscosity due to composition ?

Response: We have added an entire new section comparing our isobaric heating experiments to the more usual isothermal decompression experiments (lines 364-418) We see no evidence of increasing bubble growth rate as temperature increases. We add some estimations of viscosity changes during heating and vesiculation, but state that there are uncertainties in the values for intermediate temperatures and time (lines 373-378).

– How far is viscosity limited bubble growth (vesiculation due to heating) comparable with solubility controlled bubble growth (vesiculation due to decompression) ? What about pore throat development in each condition ?
Response: We have added an entire new section comparing our isobaric heating experiments to the more usual isothermal decompression experiments (lines 364-418)

– If temperature was maintained constant at the end of the rhyolite experiment, would bubbles have been visible after some time ?

Response: No. The sample could not be heated because it did not absorb the laser radiation. This is written in line 213-215 of the revised manuscript:

Maximum pore throat diameter

Using the maximum pore-throat diameter as the characteristic diameter for permeability raises some questions to me.
– How well is this maximum pore-throat diameter representative for the sample ? If it is the real maximum value (of a single pore), increasing the sample size may favor the presence of an even larger pore throat, leading to an increased sample permeability ? What if the larger pore throat is in a series with very small ones ?

Response: The maximum pore throat diameter in the specific subvolume analyzed is characteristic of that subvolume, and that subvolume was chosen to be representative of the central portion of the sample (far from sample surfaces). We agree that increasing the largest pore throat would increase the sample permeability at constant porosity as our model indicates. Such a problem also occurs using the model of Degruyter et al. (2010) or of Burgisser et al. (2017), where if a larger volume was to be chosen and a larger average pore throat diameter is found the permeability would increase. If the largest pore throat is in series with very small ones, then the small ones would control the permeability, however our analysis of the samples indicates that there are mulitple pore throat connections between bubbles and that permeability correlates with the largest pore throat. Regretfully, our samples are too small to chose significantly larger volumes.

– Playing Devil's advocate: Would andesitic permeability retrieval also fit that well if the volume location had changed between the different measurements ? Is there any risk that the importance of the maximum pore throat is a singularity present for this experiment that would reveal not so good for others ?

Response: It might, but we could not effectively test this as we chose the largest volume possible that we thought was representative of the sample's center for all of the measurements and the lattice-Boltzmann simulations of the permeability.

– If, instead of the maximum throat diameter, a value deduced from bubble size distribution (e.g. 90 th percentile) was used, would results still be satisfying ? How does the number of large pore throats affect permeability ?

Response: We did not test these hypotheses in this manuscript because they are beyond the scope of this manuscript. We would not be surprised if the 90th percentile distribution of the bubble sizes would produce a satisfying model and expect that if a sample has many large pore throats that the permeability at equal porosity would be greater than for a sample with only one large port throat in parallel with smaller ones.

– I compared the maximum pore-throat diameter value obtained from bubble average diameter using eq. 6 with actual pore-throat average sizes, and 84th percentile value for pore-throat sizes (meaning that 84% of pore sizes are below this value, and the rest is above), given for isotropic samples in Burgisser et al. (2017, Supplementary Information). The values obtained with eq. 6 range from -8 to about 30 µm, and correlate rather with the average pore-throat size than with the 84th percentile size given in Burgisser et al. (2017). Have you tried estimating permeability for the Burgisser et al. (2017) samples using the 84th percentile value for pore-throat size value they give ? How would fig.9c be modified ?
Response: In think the reviewer is referring to the 84th percentile of the bubble diameter, not the pore diameter. The Supplementary Information for Burgisser et al. (2017) does not include the 84th percentile for pore throat sizes, instead they only show the 84th percentile for bubble (pore) sizes. Additionally, we found a typo in Equation 6 of the older version of the manuscript (now corrected and now Eq. 9 in the revised version). This mistake of ours led to the low values calculated by the reviewer. The included table is the comparison of the average bubble size (which we used—see line 714 in the previous version of the manuscript), the mean bubble size, the average bubble size of the 84th percentile, and the throat diameter from Burgisser et al. (2017) together with the estimated maximum pore throat diameter from Equation 9 of the revised manuscript.

This table supports the reviewer's conclusion that the maximum pore throat calculated by our equation is similar to the average bubble diameter in the 84th percentile. Thus we expect that using the diameter of the 84% percentile would yield results similar to using the calculated maximum throat size. However, we have not done this because the 84% percentile is rarely reported in the literature and to our knowledge is rarely measured, whereas we chose to use the average bubble size to estimate the maximum throat size because the average bubble size is commonly reported.

Other comments
quotation comment
Lines 51-52: Connectivity [...] for each sample correlated positively with porosity and permeability. Although this result is really interesting, it is only implicit in the rest of the article (Lines 462-465 “The relationship between increasing porosity and decreasing tortuosity ... and a correlation between increasing connectivity and decreasing tortuosity” and Lines 525-527 “Increasing vesicularity increases connectivity and decreases tortuosity. All of these changes in foam structure result in higher permeabilities that are not simply related to the melt compositions investigated.”). Could you highlight this result in the article by giving more details on your observations of connectivity-permeability correlation ?

Response: We have now included Supplementary Figure 1 that presents the connectivity-porosity relations for each sample and therefore, because permeability increases with porosity (Fig. 7) an idea of the connectivity-permeability relations. Supplementary Figure 1 demonstrates that increasing connectivity is, in general, associated with increasing porosity (and permeability) for each of the compositions studied. However the relationship is not clear because high permeability basaltic samples have lower connectivities than lower-permeability andesitic ones (Supplementary Figure 1 and Figure 7). Because of this lack of simple correlation we chose not to expand our discussion of connectivity-permeability relationships in the text to minimize the length of the manuscript.

Line 75 : The competition between magma expansion due to exsolution of gas, and the loss of that gas …
In natural systems, magma expansion is also tightly linked to gas expansion due to decompression.suggest to rephrase as : « magma expansion due to gas exsolution and inflation »

Response: We have made a change similar to the suggested one (line 82 in the revised manuscript).

First paragraph :
The first paragraph of the introduction addresses the very interesting question of the influence of melt composition on bubble network and permeability development. Having four different compositions is a strength of this article, however in this new version the question of its influence on permeability development is not priory, and results do not evidence a strong influence on permeability. The evolution of connectivity and bubble connection with composition is no more addressed, and as the maximum pore-throat diameter is now used instead of the cumulative pore throat area, its implication for permeability development looks very minor. I would therefore suggest either to refocus the introduction on the more general influence of porous network parameters, or to give more visibility to the observed influence or absence of influence of composition in the rest of the article (for this last option, it would be useful to add the connectivity and connection figures in supplementary material, for example).

Response: The Introduction has been revised in response to this suggestion. We have now added a supplementary figure with the connectivity versus the porosity to the manuscript.

Lines 98-100 : This study arose from the hypothesis that foam properties, including the bubble size distribution, tortuosity, the number and size of pore throats, and the degree of interconnectivity between bubbles, play an important role in controlling the permeability of magmatic foams.

The introduction should put into perspective and emphasize the importance of the work presented. A lot of work has been done for studying this link between foam structure and permeability development, and should be reviewed here. Most of the relevant references are already cited in the introduction. However, the enhanced understanding of the link between permeability and foam structure through these studies should be precised here. The reader needs to understand what has already been done, what questions arose from it, and what still needs to be understood,that the particularities and interesting results (about pores-throats) of the study presented here, as well as the way it contributes to precedent work are emphasized.
Some references supporting the link between composition and foam structure would also welcome here.

Response: We have tried to succinctly inform the reader of previous research demonstrating the importance of parameters other than just porosity that are important in controlling the permeability (lines 98-106).

Lines 107-109 : All attempts to study a rhyolitic melt failed due to the inability of the laser furnace used in the experiments (Fife et al. 2012) to heat this composition to temperatures high enough for gas exsolution and bubble formation.
What would be a temperature high enough for rhyolite melting and bubble expansion ?
Would a rhyolite with more water have been able to vesiculate at lower temperatures ?

Response: The rhyolitic sample would simply not attain temperatures necessary for bubble growth. This has now been stated on line 215 of the revised manuscript.

Lines 110-111 : The viscous permeabilities of the foams were determined from tomographic reconstructions of sample volumes using lattice-Boltzmann techniques
Non-specialist readers may think that lattice-Boltzmann techniques were used to

reconstruct sample volumes from tomography. Adding a coma after “sample volumes” may be enough for dissipating any doubt.

Response: This sentence has been revised to make our techniques more clear to non-specialists (line 128-129 in the revised manuscript).

Lines 121-122 : We further demonstrate that characterizing the structure of the foam, and particularly the size distribution of pore-throat diameters and their cross-sectional areas, is critical
I think this result concerning pore throats should be more emphasized in the introduction. (cross sectional area, however, is no more exploited in the paper).

Response: We have modified the introduction to stress the importance of pore throats (Lines 99-106 of the revised manuscript).

Lines 137-138 : trachyandesite and dacite contained 3 wt %. water. The only successful experiment with the andesite contained 5 wt % water.
Could you precise how the water concentration is calibrated ?

Response: We have now stated that the water concentrations are based upon the weight fractions of water used in the synthesis experiments (lines 159-160 of the revised text).

Lines 177 – 178 : Data acquisition was initiated at the first visible onset of vesiculation, bubble formation, and sample expansion.
Do you mean that you look for the first onset either of vesiculation or bubble formation or sample expansion, or that bubble formation and sample expasion are visible onsets of vesiculation ? In the first case, I suggest to replace “and” by “or” In the second case, I suggest to replace the coma after vesiculation by “:”, or add “such as” before bubble formation.

Response: We have followed the reviewer's suggestion (line 201 of the revised manuscript).

What is the difference between vesiculation and bubble formation ?

Response: None in this case. Following the reviewer's advice from the previous comment we think we have made this clear in the revised manuscipt.

Line 197 : These experiments span much of the range of porosities
Are these different porosities obtained because of different ending conditions (then it should be mentioned) or because there was, for example, some gas loss ?

Response: Bubble growth stopped due to gas loss from the sample. This has been added in the revised manuscript (line 222).

Line 232-233 : Objects, bubbles and pore throats, were not counted unless their size was greater than two voxels.
Could you recall here the size of a voxel (2.89x2.89x2.89 μm^3), to facilitate fig. 3-6 reading ?

Response: We have followed the reviewer's suggestion (line 245 of revised manuscript).

Line 236 : The geometrical determination of pores and throats is …
The word “pore” is sometimes associated with bubbles, and sometimes with pore-throats, which is a little bit confusing, especially in this paragraph and in the following. Would it be possible to homogenise this in the article, so that “pore” is always associated either with “bubble” or with “pore-throat” ? If the presence of this word here is necessary for explaining the measurement method, it may be helpful to replace it by another synonym that does not appear elsewhere in the article (e.g. vesicle, hole, void, space).

Response: We have gone through the manuscript to ensure that the term “pores” is

	only used in conjunction with pore throats and not used as a synonym for bubbles. Lines 252-254 : Practically, this means that the throat-size distribution may present some large- valued outliers due to the consideration of branches that do not represent physical channels. Could you give more details on how throat sizes are estimated ? Are these large-value outliers removed before taking the maxium pore throat diameter value for permeability calculation Response: We have now provided more details on how the throat sizes are estimated (lines 255-259 in the revised text). There is one basaltic experiment with 0.55 porosity that contains one pore throat that is anomalously larger then the next largest one (see Fig. 3b). Whereas we cannot completely discard the possibility that the largest pore throat in this sample is an artefact, we think that size difference between the largest pore throat and the others in the distribution is not sufficiently large to discard the measurement (lines 504-509 in the revised manuscript). Please note that the lattice-Boltzmann permeability determinations do not involve the measurements of the pore throat diameters and are performed directly using the tomographic reconstructions. Also note that if we use the next-largest pore throat for this experiment in our modified Burgisser model, the estimated viscous permeability is still within 1 log unit of the Lattice-Boltzmann permeability. Lines 255-256 : The final assessment of pore (bubble) size is based on the diameter of the maximal inscribed sphere centered on the center of mass of the cluster of the overlapping inflated bubbles (Fig. 1H). and Lines 1109-1111 : The size of the bubble to be counted is determined by a maximal inscribed sphere that is centered on the center of mass determined from the merged bubbles. Might this method underestimate the bubble size ? If yes, what is the error made using this method ? If you sum up the bubble volumes obtained this way, and then divide it by the total sample volume, do you get back to the measured porosity ? Response: No, the method of maximal inscribed spheres is the standard method used when a skeletonization approach is used to assess the bubble size distribution (see Hildebrand and Rüegsegger 1997 for details of the method—reference in text). The sum of the bubble volumes divided by the sample volume do not yield the total vesicularity because our techniques do not measure the volume of the pore throats only their diameter. Lines 326-327 : No evidence of a significant nucleation delay (i.e., longer than a few seconds) was detected in any sample. If there was any, what would you expect to see ? What are the criteria that you use to estimate whether there is a delay or not ? Response: We have deleted this sentence and discussed possible nucleation delay after the presentation of the estimated glass transition temperatures (lines 438-442 of the revised manuscript). Lines 335-340 : We estimate a minimum onset of the glass transition in our samples with 3 wt% water (MORB, trachyandesite, and dacite) at 460 °C and in the andesite with 5 wt% water at 440 °C. However our heating rates were approximately 3 to 15 times more rapid than used in Giordano et al.'s experiments, thus the observed vesiculation temperatures were significantly above these minimum glass transition temperatures, in the range of 616 to 900 °C (Table 2). Are these differences between the observed temperatures and the theoretical one due to observation limitations (e.g. determine vesiculation onset), in which case this should be mentioned, or should it be considered as a delay in vesiculation ? In this later case, this sounds contradictory with lines 326-327. Do you expect vesiculation as soon as the glass transition is crossed ? I think some clarifications are needed here. Response: We clarified and moved our presentation of the glass transition and possible nucleation delays to lines 426-442 in the revised text.

Line 387 : the BNDs are in the thousands
BNDs are most often indicated in the literature as a number of bubbles per m^3. Here I understand that you talk about a number of bubbles per mm^3 (maybe because this is sample volume order of magnitude ?). This unit should be indicated here.

Response: The units have now been specified (line 492 in the revised manuscript)

Lines 387-388 : The two samples with the lowest porosities (0.52 and 0.50) are from the same experiment and demonstrate that with time the number
The fact that the samples with porosities of 0.52 and 0.50 are consecutive in time should be explicitely mentioned somewhere. For even more clarity, I think that the fact they are from the same experiment should be recalled in fig.3 legend, otherwise it is not straightforward to understand why these samples are not sorted by increasing porosity.

Response: This has now been stated on lines 496-498 of the revised manuscript.

Lines 403-404 : the sample volume quantified varied slightly between different time steps to avoid counting anomalously large bubbles.
What would happen if you considered such a sample (with anomalously large bubbles) and use the permeability formula with the largest pore throat size ?

Response: Although we haven't done this because we concentrated on using the most representative portions of the interiors of the samples, we think our model would work on any sample where the appropriate values for Equation 9 are known.

Line 406 : about andesite samples BSDs
For the three first andesitic samples presented in fig.4, the porosity evolves from 0.17 in the first sample to 0.28 in the third one. However, looking at the bubbles size distributions, all per mm^3, the number of bubbles observed in the first sample (porosity 0.17) is higher than that observed in the two other samples (porosities of 0.28), for every bubble size bin. Were the porosity and BSDs measured for the same volumes ? Were bubbles counted in the whole volume whereas porosity corresponds to connected porosity only ? This evolution is quite surprising, and I think some explanations would be welcome here (or in the fig.4 legend).

Response: There was a mistake in constructing this plot and it has now been fixed and the other plots checked.

Line 419 : a single bubble and Line 422 : one appears at Φ = 0.64
Would it be possible to mention the volume of the sample here (about 0.05 mm^3), so that it is more straitforward to make the link between this single bubble and the ~20 bubbles shown in fig.5 ?

Response: This has now been done on line 537 of the revised manuscript.

Lines 429-430 : up to a maximum of almost 400 μm at Φ = 0.84 (Fig. 6a).
and lines 436-437 : The PTDs of the dacitic sample demonstrate growth of larger pore throats up to a porosity of 0.87 followed by a decrease in that value as the sample reached Φ = 0.84 (Fig 6b).
It could be usefull to indicate in the fig.4-6 legends that the different panels correspond to successive times

Response: This has been done for the revised manuscript. Please see the caption for Figure 3.

Lines 445-446 : values in the hundreds to thousands
The unit should be precised here.

Response: This has been done in the revised manuscript (lines 565-566)

Lines 449-456 : The average coordination number (or number of bubbles surrounding a specified bubble) [...] and the maximum coordination numbers are often near 100 and can reach almost 600 (Table 2).

Could you be more precise in the definition of the coordination number ? Does it count bubbles that are in direct contact with the specified bubble (and maybe connected) ? Or does it count bubbles in the proximity of the bubble of interest ? In this case, up to which distance is a bubble considered to be in proximity ?

Response: This was been specified on line 449 of the previous version of the manuscript as the number of bubbles surrounding a specified bubble. In the revised manuscript we have expanded our explanation of the average coordination number on lines 569-570.

Lines 462-465 : about connectivity
I remember that there was a figure showing connectivity results in the first version of this paper. Could this figure be added to the supplementary material ? I think this would be of interest for readers.

Response: We added this figure to the manuscript as supplementary material; we note that interested readers can easily construct it from Table 2 in the manuscript.

Lines 480 – 482 : Permeability thresholds in natural and experimental magmatic foams can vary from below ~0.03 (e.g., Saar and Manga 1999; Bai et al. 2010) to values in excess of 0.63 (Lindoo et al. 2016).
The experimental data from Takeuchi et al. (2009) could also be of interest here : They studied magma permeability development from experimentally decompressed rhyolitic melts, and found that samples with a porosity below 80% were almost impermeable. These data were fitted by Rust and Cashman (2011) (see their fig.5), with a power law relationship similar to the one you give (lines 475-476), in which Φ is 78% .

Response: The crystal-free and crystal-poor permeability measurements of Takeuchi et al (2008, 2009) have now been included. See also line 606 in revised manuscript.

Lines 575-600 : Percolation theory and particularly Lines 591-592 : Thus, the size distribution of spherical bubbles is expected to have a minor effect on the percolation threshold.
Although the percolation theory is a strong tool for understanding percolation and permeability development, it does not account for magma and bubble dynamics, nor for bubble interactions. I think that the limits of this approach should be discussed later in the section. How did natural and experimental observations temper this interpretation ? Particularly, Burgisser et al. (2017), found that the bubble size distribution does have a significant effect on percolation development in experimentally decompressed rhyolitic melts, which is contradictory with the results from Consiglio et al. (2003).

Response: A complete discussion of percolation theory and bubbles is far beyond the scope of this manuscript. Our goal was only to present the very basic aspects of percolation theory and compare its percolation thresholds to the experimentally measured ones. We have now added Burgisser et al.'s (2017) observations to our discussion of the effects of size distribution on the percolation threshold (line 764-766).

Lines 623-624 : Each specific sample may have its own critical porosity based upon the size distribution and shape of the bubbles and pore throats in the sample, as discussed above. And Line 639 : such as the size distributions of bubbles and pore throats
It looks like the conclusion above was that bubble size distribution should have a minor influence on the percolation threshold, which looks contradictory to the idea you express here. Or do you refer to somewhere else in the text ? Could you indicate more precisely the section where to look for this discussion ?

Response: Lines 575-600 are discussing the conclusions from percolation theory and lines 623-624 and 639 are discussing what is seen the permeability measurements and what we think is affecting the permeabilities. We try to make clear in this section and in subsequent sections of the manuscript that percolation theory provides important ideas about the development of permeability with porosity, but that there are many details concerning bubble interactions that remain to be discovered.

Lines 683-686 : Applying this paradigm, the porous network in foams can be envisioned as resistors interconnected to one another to create a continuous circuit that when the permeability threshold is exceeded allows fluid to flow across the sample. The connections between resistors in the network can be either in parallel or in series (Stauffer and Aharony 1994).
Blower et al. (2001) should also be cited here.

Response: Blower et al. (2001) has now been cited in the revised text on lines 877, 881.

Lines 699-701 : Based upon this observation, an empirical value of χ = 10 (5 times the original value of χ = 2) was chosen, and the resulting fit of the Burgisser et al. model to the data is remarkable (Fig. 9b), with all but one of the measurements reproduced to within one log unit and a chi-squared value of 0.01.
χ refers to the permeable pathway circularity. In the case of spheres its value should be 2. Changing its value to 10 to fit the data looks confusing to me, why not introducing a fitting parameter instead ?

Response: In the revised text we have indicated that the value of 10 can be thought of as a fitting factor of 5 times the value for a circular cross-section on line 896.

Lines 708-710 : Additionally, we found that the maximum throat diameter can be related to the average bubble size, davg bubble, by
The values obtained with eq. 6 range from -8 to about 30 μm for Burgisser et al. (2017) isotropic samples, and correlate rather with the average pore-throat size than with the 84th percentile size given in Burgisser et al. (2017). See main comments.

Response: Please see our response in the main comments section of this reviewer.

Line 770 : A brief discussion of inertial permeability
Have you heard about this paper from Zhou et al. (2019) that came out very recently ? It relates inertial and viscous permeabilities for a wide range of geological materials. It is much more general and less precise than the relationships you cite here, but could be of interest for introducing the general apparent existence of a link between viscous and intertial permeabilities.

Response: We have now deleted this section from the revised manuscript and discuss Zhou et al. (2019) in the introduction of the revised manuscript (lines 135-139). We have kept the discussion of Zhou et al. succint in our efforts to shorten the length of the manuscript.

Lines 872-875 : Gas lost to the conduit walls would imply a larger volume gas loss that would still affect the permeability-porosity relations of the magmatic foam. Such gas loss through the conduit walls would have implications on transitions in eruptive style. Thus, the fundamental results of the Namiki and Manga (2008) model appear sound.
These few sentences sound a little bit contradictory to me, as I understand that you frist say that gas loss to the country rock could have a significant influence, and then deduce from this that the model from Namiki and Manga (2008), that does not account for it, is sound. Could you explain why the model from Namiki and Manga (2008) is sound despite of not considering gas loss to the rock ? Or rephrase or rearrange this parragraph so that in does not sound that contradictory ?

Response: We have now dropped the section on the Namiki and Manga model.

Lines 1097-1098 : with a smaller 160 160 pixel region used for quantitative measurements.
Is the 160x160 pixel region the one used for permeability measurements using lattice-Boltzmann techniques ? It appears to contain very large bubbles (that cover in length more than half of the sample). Are permeability measurements still reliable in this case ? Blower (2001) provide evidence that the permeability-porosity relationship is independent on bubble and sample size as long as the bubble radius is smaller than 0.1X (with X the size of the volume considered), in the case of a mono-disperse size distribution. This can be interpreted as the sample dimensions should represent at least 5-10 bubbles to be representative. How many bubbles are contained in every

dimensions of your samples ? Were any test on permeability vs size of the sample done ? This may provide another argument for representativeness. Are such big bubbles present in every analysed sample, or only in the most porous ones ? In this case, I would suggest, if available, to put images less controversial here (same sample at a lower porosity for example).

Response: The techniques used by Blower (2001) are significantly different from those used in this study and the constraints provided by Blower don't necessarily apply to the lattice Boltzmann simulations used in this study, although they are good starting guidelines. Instead, we have compared our simulations in terms of sample size, bubble fraction, and resolution to those of Bai et al. (2010) and found that we were within the range of those parameters where the results of lattice Boltzmann simulations are reliable. (see lines 334-355)

Lines 1099-1101 : only considering larger interconnections between bubbles. e) The same reconstruction also considering smaller interconnections and main text.
Could you give some more details on what is the difference between large and small interconnections ? What does the tunning parameter select ? Is it considering only connections when the pore throat is above a critical size ? What is the criteria that is changed ?

Response: Practically the algorithm considers a downscaled (averaging multiple voxels together and replacing them by one pixel equivalent in volume to the sum of the averaged voxels) or upscaled version (finest resolution) of the volume. In a downscaled version of the volume, small interconnections disappear (and the algorithm is also faster). In an upscaled version of the volume (similar to using a digital zoom of a camera), small interconnection results are represented with more voxels and therefore the medial axis (which is a digital object having exactly one voxel thickness) can "pass through" that small interconnection. The changed criterion is the up- or down-scaling of the input volume. This has been explained a little more in the caption to Figure 1 in the revised text.

Line 1103 : pore throats (yellow) measured
What do you mean by pore throats here ? What is the pore throat size measured ? Is it the length of these yellow lines ? Or is it the diameter of the pore ? In this last case, how is it measured ?

Response: The caption to Figure 1 has been modified to indicate that the yellow lines are the 1-voxel skeleton. We do not measure the length of the yellow lines, nor does it make sense to do so because many of them are inside the bubbles, as shown by comparison of figures 1d, e, f, g and h. Details concerning the measurement of bubble and pore throat diameters are provided in the text (see lines 254-264 in the revised text).

Lines 1104-1105 : To reduce the number of over-counted nodes, spheres are centered at each node and inflated by differing degrees
Does this inflation process accounts for existing bubble walls ? Or may bubbles close to each other, but not connected, merge artificially ?

Response: The inflation process accounts for bubble walls; bubbles close to each other, but not connected, cannot merge artificially.

Caption of fig.7 : The blue line (andesitic data fit) has no legend. Could you add some ?

Response: The significance of the blue line has been added to the figure caption in the revised version of the manuscript (lines Figure 7 caption).

Figure 2a : Could you add a scaling bar of 1mm on the first picture ?

Response: That has been done.

	Figure 2b : A scaling bar would also be great here (the scale is not the same as in a, is it ?). Response: That has been done. Figure 3 : Could you precise in the legend that the first two panels are successive in time, and from the same sample ? Response: This has been done (revised manuscript Figure 3 caption). Table 2 : Foot notes references on the table look to start at five (and I did not found the reference to footnote 1). Would it be possible to name them in a more instinctive way ? References on table 1 are very easy to follow. Response: This was my mistake in the previous version and has been corrected. Typos add remove Line 136 : capsules-CORRECTED Line 301 : The ratio had no effect of on the permeability-CORRECTED Line 688 : the Carmean-Kozeny-CORRECTED Line 755 : The formation of a pore-CORRECTED Line 768 : Lindoo et al. (2017) (about the influence of crystals)-CORRECTED Line 791 : vary by only by about-CORRECTED/DELETED Line 824 : Liu et al. (2005)-CORRECTED/Deleted Line 1160 : either the Carman-Kozeny equation or the Carman-Kozeny equation of Degruyter et al. (2010) and that of Burgisser et al. (2017).-This sentence has been modified. References Blower JD (2001) Factors controlling permeability-porosity relationships in magmas. Bull Volcanol 63:497-504 Burgisser A, Chevalier L, Gardner JE, Castro JM (2017) The percolation threshold and permeability evolution of ascending magmas. Earth Planet Sci Lett 470:37-47 Lindoo, A., Larsen, J.F., Cashman, K.V., Dunn, A.L., Neill, O.K., 2016. An experimental study of permeability development as a function of crystal-free melt viscosity. Earth Planet. Sci. Lett.435, 45–54. http://dx.doi.org/10.1016/j.epsl.2015.11.035. Rust, A.C., Cashman, K.V., 2011. Permeability controls on expansion and size distributions of pyroclasts. J. Geophys. Res.116. Takeuchi, S., Tomiya, A., Shinohara, H., 2009. Degassing conditions for permeable silicic magmas: implications from decompression experiments with constant rates. Earth Planet. Sci. Lett.283, 101–110. Zhou, J.-Q., Chen, Y.-F., Wang, L., & Cardenas, M. B. (2019). Universal relationship between viscous and inertial permeability of geologic porous media. Geophysical Research Letters, 46. https://doi.org/10.1029/2018GL081413
Author Comments:	Note that two copies of Table 1 and of Table 2 have been included in this submission. One copy of each table is in .pdf format so that it can be easily read and the other copy is in .xls format

McGill

Earth and Planetary Sciences
McGill University
3450 University Street
Montreal, QC, Canada H3A 2A7

Sciences de la terre et des planètes
Université McGill
3450 rue University
Montréal (Québec) Canada H3A 0E8

Tel./Tél.: (514) 398-7485
Fax/Télé : (514) 398-4680
don.baker@mcgill.ca
http:// www.mcgill.ca/eps

3 May 2019

Professor Katharine Cashman
Editor of The Bulletin of Volcanology
University of Bristol

Dear Kathy,

Enclosed you will find our revisions to manuscript BUVO-18-00171. In response to the comments of the reviewers we have made substantial modifications to the manuscript and have reduced the Discussion from 19 pages to ~ 11.

We thank you for your continued evaluation of this manuscript for publication the The Bulletin of Volcanology.

Sincerely,

Don Baker, McGill University

The importance of pore throats in controlling the permeability of magmatic foams

Don R. Baker[1], Francesco Brun[2,3], Lucia Mancini[2], Julie L. Fife[4], Alexandra LaRue[1], Cedrick O'Shaughnessy[1,5], Reghan J. Hill[6], Margherita Polacci[7]

[1]Earth and Planetary Sciences, McGill University, 3450 rue University, Montreal, QC H3A 0E8, Canada don.baker@mcgill.ca

[2]Elettra-Sincrotrone Trieste S.C.p.A., S.S. 14-km 163.5, ~~34149~~ Basovizza, 34149, Trieste, ~~(TS),~~ Italy

[3]Currently: Istituto Nazionale di Fisica Nucleare (INFN) - Sezione di Trieste, Padriciano, 99, 34149 Trieste, ~~–~~ Italy

[4]Previously with: Laboratory for Synchrotron Radiation, Swiss Light Source, Paul Scherrer Institut, 5232 Villigen, Switzerland

[5]Currently: Department of Earth Sciences, University of Toronto, 22 Russell St., Toronto, M5S 3B1

[6]Department of Chemical Engineering, McGill University, 3610 rue University, Montreal, QC~~uebec,~~ H3A 0E5, Canada.

[7]School of Earth and Environmental Sciences, University of Manchester, Manchester, U.K.

Corresponding author: don.baker@mcgill.ca
1-514-398-7485

BUVO-S-18-00171
Revised 3 May 2019
~~9 December 2017~~
~~Revised 17 July 2018~~
~~Revised 4 December 2018~~
~~Revised April 2019~~

Abstract

Foam formation during vesiculation of hydrous magmatic melts at 1 atm was studied *in situ* by synchrotron X-ray tomographic microscopy at the TOMCAT beamline of the Swiss Light Source (Villigen, Switzerland). Four different compositions were studied; basaltic, andesitic, trachyandesitic and dacitic hydrous glasses were synthesized at high pressures as starting materials and then laser heated on the beamline. The porosity, bubble number density, size distributions of bubbles and pore throats, as well as the tortuosity and connectivity of bubbles in the foams, were measured in three dimensions based on tomographic reconstructions of sample volumes. The reconstructed volumes were also used in lattice-Boltzmann simulations to determine viscous permeabilities of the samples.~~foams.~~ Connectivity of bubbles by pore throats varied from ~100 to 10^5 mm^{-3}, and for each sample correlated positively with porosity and permeability. Although permeability increased with porosity, the relationship is complex; consideration of the results of this and previous studies of the viscous permeabilities of aphyric and crystal-poor magmatic ~~foams~~samples demonstrated that at similar porosities the permeability could vary by many orders of magnitude, even in similar composition samples~~foams~~. More than 90 % of these permeabilities are bounded by two empirical power laws, neither of which identifies a percolation threshold.

Comparison of the permeability relationships from this study with previous models (Degruyter et al. 2010; Burgisser et al. 2017) relating porosity, characteristic pore-throat diameters and tortuosity demonstrated good agreement. However, modifying the Burgisser et al. (2017) model by using the maximum measured pore-throat diameter, instead of the average diameter, as the characteristic diameter ~~improved the fit of the~~produced a model that reproduced the lattice-Boltzmann permeabilities to within 1 order of magnitude~~with respect to permeability determinations~~. Measured correlations between the average bubble diameter and the maximum pore-throat diameter as well as between

porosity and tortuosity in our experiments produced relationships that allow application of the modified Burgisser et al. model to predict permeability based only upon the average bubble diameter and porosity. The experimental results are consistent with previous studies suggesting that increasing bubble growth rates result in decreasing permeability of equivalent porosity foams. The effect of growth rate on permeability is hypothesized to substantially contribute to the multiple orders-of-magnitude variations in the permeabilities of natural magmatic ~~foams~~samples at similar porosities. ~~Applying the steady-state magma ascent and eruption model of Namiki and Manga (2008), we find that only magmatic foams with the highest permeabilities will lose their expanding gases, and, therefore, the driving force for their ascent and eruption. The Namiki and Manga (2008) model also indicates that gas loss can occur at low porosities in highly permeable magmas.~~

Keywords: magmatic foam, permeability, bubble and pore throat sizes, bubble connectivity, synchrotron X-ray tomography

Introduction

The competition between magma expansion due to gas exsolution ~~of gas~~and expansion, and gas loss~~,~~ ~~and the loss of that gas through the porous network~~ created by vesiculation in volcanic conduits, exerts a significant control on the explosivity of volcanic eruptions (e.g., Sparks 2003; Spieler et al. 2004, Mueller et al. 2005, 2008). This competition is profoundly influenced by the permeability of the magmatic foam (a mixture of gas-filled bubbles and melt that may contain crystals and if quenched would produce a scoria or a pumice). Relatively impermeable magmas~~foams~~ can lead to violent eruptions, whereas permeable ones may~~do~~ not (Sparks 2003; Mueller et al. 2005, 2008). Understanding the development of porosity, Φ, and permeability, k, during magma vesiculation is one of the keys to quantitative modeling of volcanic processes that hold the promise of a better understanding of volcanic eruptions and their precursors (Fagents et al. 2013). Due to the significance of permeability, many studies characterized the porosities and permeabilities of natural samples and experimental run products and demonstrated orders-of-magnitude differences in permeability at similar porosities~~, finding useful relationships between porosity and permeability~~ (e.g., Klug and Cashman 1996; Saar and Manga 1999; Blower 2001; Rust and Cashman 2004; Mueller et al. 2005, 2008; Bouvet de Maisonneuve et al. 2008; Wright et al. 2009; Degruyter et al. 2010; Bai et al. 2010; Polacci et al. 2014; Farquharson et al. 2015; Kushnir et al. 2016; Lindoo et al. 2016; Burgisser et al. 2017).

The structural details of porous media, such as tortousity and the size of the bubbles and pore throats that connect them have long been known to significantly influence permeability (Carman 1937; Archie 1942). Polacci et al. (2008) suggested that "a few large vesicles, exhibiting mostly irregular, tortuous, channel-like textures" in scoria from Stromboli volcano (Italy) were the preferential pathways used for gas escape from the magma. Degruyter et al. (2010) and Burgisser et al. (2017) both demonstrated that the tortuosity of the sample and the characteristic diameter of the pore throats played significant roles in controlling magmatic permeability. These publications demonstrated that the size of the bubbles, the pore throats that connect them, and the ways in which bubbles are interconnected (tortuosity and either in a series or parallel configuration) are significant controls on gas transport in magmatic systems. ~~Using then-available measurements, Bai et al. (2010) proposed one general porosity-permeability relationship for basaltic foams and another for dacitic-to-rhyolitic ones. Although this compositional systemization of porosity-permeability relationships provides a useful reference, more recent studies of porosity and permeability have indicated that Bai et al.'s (2010) binary division of porosity-permeability relationships into basaltic and silicic foams breaks down (e.g., Burgisser et al. 2017). Nevertheless, the permeabilities of basaltic foams are generally greater than those of more silicic foams at similar porosities, suggesting that melt chemistry plays a role in the development of the foam~~

~~structure, and that this structure in turn controls the permeability (e.g., Blower 2001; Wright et al. 2009; Bai et al., 2010).~~

~~This study arose from the hypothesis that foam properties, including the bubble size distribution, tortuosity, the number and size of pore throats, and the degree of interconnectivity between bubbles, play an important role in controlling the permeability of magmatic foams.~~ Here we report results of a series of high-temperature, *in situ* X-ray tomographic microscopy experiments studying the development of crystal-free, vesiculating samples~~foams~~ of silicate melt at 1 atm. Although in the experiments bubbles are formed during heating at constant pressure (rather than during decompression at approximately constant temperature in volcanic systems), the development of the interconnections between bubbles provides important information on the formation of magmatic foams and development of their permeability. Four melt compositions were studied: a mid-ocean ridge basalt (MORB), a trachyandesite, an andesite, and a dacite~~. All attempts to study a rhyolitic melt failed due to the inability of the laser furnace used in the experiments (Fife et al. 2012) to heat this composition to temperatures high enough for gas exsolution and bubble formation.~~

The viscous permeabilities of the foams were determined by using~~from~~ tomographic reconstructions of sample volumes as the input for~~using~~ lattice-Boltzmann ~~technique~~simulations of fluid flow (Hill et al. 2001; Hill and Koch 2002)~~ with the goal of creating a general model that can be used for the calculation of silicate foam permeability~~. We concentrated on the viscous permeability k_1, and the applicability of the Carman-Kozeny equation to magmatic foams (Carman 1937). Although we have not investigated the inertial permeabilities, k_2, in our samples, relationships between viscous and inertial permeability have been previously determined (e.g., Rust and Cashman 2004; Yokoyama and Takeuchi 2009; Bai et al. 2010; Polacci et al. 2014; Burgisser et al. 2017). Most recently Zhou et al. (2019) proposed a universal power-law equation relating viscous and inertial permeabilities for all geologic porous media with parameters equivalent to those previously published by Polacci et al. (2014) for volcanic samples. Thus, knowledge of the viscous permeability allows calculation of the inertial permeability using the relationships in Polacci et al. (2014) and Zhou et al. (2019). Better knowledge of the foam structure holds the promise of increasing our understanding of the relationship between viscous and inertial permeability with the goal of a universally applicable relationship between the two.

We show that the viscous permeability of the studied foams is complexly controlled by their structure. We further demonstrate that characterizing the structure of the foam, and particularly the size distribution of pore-throat diameters and their cross-sectional areas, is critical to predicting viscous permeabilities to within an order of magnitude. The results are also found to support previous hypotheses concerning the role of bubble growth rate on silicate foam permeability. Combining fits to porosity-permeability data and a model of magmatic foam ascent demonstrates that only the most permeable samples appear to have the potential to lose the gases that drive their ascent, and that this loss of gas can occur at low porosities.

Methods

Hydrous glass preparation

Samples of MORB, trachyandesite, andesite, and dacite were chosen for these experiments (Table 1). The MORB is a dredge haul sample graciously donated by C. Langmuir; the trachyandesite is a scoria from the 2010 eruption of Eyjafjallajökull, Iceland, and the andesite and dacite compositions were from Atka Island, Alaska, USA. Each sample was ground to less than 50 μm in diameter and dried at 110 °C before use. Approximately 70 mg of powder plus distilled water were loaded into 3 mm diameter Pt capsules and welded closed in a water bath without volatile loss. Water concentrations are based upon the water added to the capsules and was 3 wt % in successful experiments with MORB, trachyandesite and dacite ~~contained 3 wt %. water~~. The only successful experiment with the andesite contained 5 wt % water. The rock plus water mixtures were melted above their liquidi in a piston-cylinder apparatus at a temperature of 1250 °C or 1200 °C (the trachyandesite only), and a pressure of 1.0 GPa for a duration of 2 h or of 1 h (again only the trachyandesite) in 19.1 mm NaCl-pyrex assemblies (Baker 2004) and quenched isobarically. Subsamples with volumes of approximately ~1 to 2 mm^3 of these crystal-free glasses were used for the synchrotron X-ray tomographic microscopy experiments.

In situ synchrotron X-ray tomographic microscopy

In situ synchrotron X-ray tomographic microscopy was performed at the TOMCAT beamline of the Swiss Light Source at the Paul Scherrer Institut (Villigen, Switzerland) using a laser-based heating system (Fife et al. 2012) and the ultra-fast endstation (Mokso et al. 2010, see Mokso et al. 2017 for current capabilities of the ultra-fast endstation that differ from the description below and allow more rapid acquisition of images than possible when this study was performed). The laser system comprises two, class four diode lasers of 980 nm wavelength on opposite sides of, and 40 mm away from, the sample; these each provide up to 150 W of power to heat the sample. A pyrometer was used to measure the temperature. The ultra-fast endstation incorporated a pco.DIMAX camera, which acquires and transfers data orders of magnitude faster than traditional CCD technology (Mokso et al. 2010). To reach the highest possible temperature, the lasers were pointed just below the sample holder on the zirconia rod that connected the sample holder to the rotation stage below. The temperature was increased until it reached approximately 600 °C at which point the sample was lowered into the laser beams. Samples were then heated at either 1 °C s^{-1} or 6 °C s^{-1} to the maximum temperature of the experiment, resulting in sample vesiculation and creation of a silicate foam under open-system conditions such that the sample was free to expand and exsolved gas escaped the system. Initially a programmed heating rate of ~6 °C s^{-1} was chosen as the best compromise between instantaneous heating of the sample and the need for bubbles to grow slowly enough to be successfully imaged. Due to many experimental failures, a slower programmed heating rate of ~ 1 °C s^{-1} was found to produce more successful experiments (Table 2). Measurement of the time-temperature histories of the experiments demonstrated that the heating rates were often ~ 20 percent slower than the programmed ones (Table 2).

~~Experiments were performed by isobaric heating at atmospheric pressure, with a time-temperature-pressure path distinctly different from bubble formation during near-isothermal decompression in natural systems, because a high-pressure furnace is not available on the TOMCAT beamline.~~

~~Subtracting atmospheric pressure from the hydrous melt supersaturation pressure (Table 2) yields the difference between the starting pressure of vesiculation and its final pressure (0.1 MPa) when water was exsolved from the melt. Dividing this pressure drop by the duration of the isobaric heating (Table 2) yields equivalent decompression rates of approximately 0.1 to 2 MPa s^{-1}. Although these equivalent decompression rates are considered only rough approximations for comparison of the experiments with nature, the low values are similar to decompression rates found by Ferguson et al. (2016) for eruptive products of Kilauea volcano and the high values to decompression rates found by Humphreys et al. (2008) for the May 18, 1980 plinian eruption of Mt. St. Helens.~~

Data acquisition was initiated at the first visible onset of vesiculation, such as bubble formation~~,~~ and sample expansion. During data acquisition, samples reached a maximum temperature between ~950 °C and ~1200 °C. Polychromatic X-rays were filtered to 5 % power, generating 3 ms exposure times, and 701 projections were captured over an angular range of 180 degrees during continuous rotation. The microscope used for these scans incorporated a specially designed, high numerical aperture objective lens with ~~its~~four-fold magnification~~ set to four-fold for these experiments~~. This corresponded to a 2.89 µm × 2.89 µm pixel size and a 5.83 mm × 5.83 mm field of view. The optics were coupled to a LuAG:Ce 100 µm thick scintillator screen. Reconstructions were performed using a modified GRIDREC algorithm (Dowd et al. 1999; Rivers and Wang 2006; Marone and Stampanoni 2012) coupled with Parzen filtering of the sinograms.

Many bubble-growth experiments were performed, but only a few were successful. The most significant problem was image blurring due to sample motion caused by rapid vesiculation and bubble growth that rendered the tomographic reconstructions useless for this study. Other problems were samples that failed to heat to temperatures high enough to vesiculate~~ (e.g., all rhyolitic samples and some of the other compositions)~~ (which included all rhyolitic samples investigated) and samples that cracked into small pieces during heating.

Of the 62 experiments performed, only one dynamic experiment on the andesitic composition, one on the trachyandesitic composition, and one on the dacitic composition yielded 3D reconstructions that could be used to extract quantitative data. Bubble growth in all dynamic experiments on the MORB composition was so rapid and the motion artifacts so severe that no successful reconstructions were made. However, the final steps of 4 experiments on the MORB composition were successfully imaged as bubble growth slowed or stopped due to gas loss from the sample. These experiments span much of the range of porosities measured in the successful tomographic scans on the andesite, trachyandesite, and dacite, and allow comparison between the four different melt compositions. Even the successful experiments contained some image artefacts due to sample movement during bubble growth. These aretefacts were avoided during the sample analysis discussed below.

Image analysis and quantification

The bubble distributions in the samples were not homogeneous because of thermal gradients in the laser furnace. Thus, only ~~selected~~representative central portions of the samples, far from their edges and the capsule walls, were analyzed, and the measurements reported are not representative of the entire sample, but only of the volume investigated. The tomographic reconstructions were inspected with ImageJ and subvolumes from the most vesicular portions of the samples were chosen; in most cases they were 256 × 256 × 256 voxels in volume (Fig. 1a-c). Because these volumes were too large for lattice-Boltzmann determination of their permeability (discussed below) representative subvolumes of 370 × 370 × 370 μm^3 (128 × 128 × □128 voxels, trachyandesite EFJ-8a), or 462 × 462 × 462 μm^3 (160 × 160 × 160 voxels, andesite DRB2012-2a, dacite DRB2012-6e-8, -9, -10, MORB DRB2012-7a-2, -3, -cf) or 578 × 578 × 578 μm^3 (200 × 200 × 200 voxels, dacite DRB2012-6e-07, MORB DRB2012-7f-10) were used for all quantitative analyses with the *Pore3D* software library (Brun et al. 2010; Zandomeneghi et al. 2010). An edge-preserving smoothing filter (Tomasi and Manduchi 1998) was applied followed by a 3D, manually selected, global fixed threshold to separate pore space from glass. This segmentation process was adopted for all datasets.

The vesicularity was computed as the number of voxels belonging to the pore space with respect to the total number of voxels in the object. Objects, bubbles and pore throats, were not counted unless their size was greater than two voxels, where each voxel was 2.89 × 2.89 × 2.89 μm^3 in volume. Baker et al.'s (2011) study of the reproducibility of porosity measurements using X-ray microtomography ~~Multiple measurements by different investigators ha~~demonstrated~~ve demonstrated~~ that the precision of vesicularity measurements is approximately 0.01~~; this estimate is based upon multiple 3D measurements of the same sample in ImageJ that produced an average porosity of 0.503 with a standard deviation of 0.010 (Baker et al. 2011)~~. We expect similar uncertainties for pore throats because the same techniques were used for measurements of vesicles and pore throats. The interconnected porosity was determined from the same images using the ObjectCounter3D plugin in ImageJ (https://imagej.net/3D_Objects_Counter).

A family of descriptors based on skeleton analysis (Lindquist and Lee 1996) was applied to derive bubble number and pore throat number density as well as bubble- and pore throat-size distributions. As in our previous research (Baker et al. 2012), the skeletonization algorithm of Brun and Dreossi (2010) was applied.~~,~~ Each~~and~~ bubble diameter~~s~~ and~~-~~ the minimum thickness of each pore throat~~ thicknesses~~ was~~ere~~ computed using the concept of a maximal inscribed sphere, which was moved through the pore throat along the skeleton to find its minimum diameter (Hildebrand and Rüegsegger 1997~~6~~). The skeletonization algorithm used in this study offers a tuning parameter to control the amount of branches in the output skeleton. Figures 1d & e present the differences between a case where only the most significant (and larger) interconnects are considered and a case where the smallest interconnects are considered and a skeleton branch is added to the skeleton network for each of them. This parameter is tuned to select the maximum number of branches in this study.

The geometrical determination of~~ pores~~ bubbles and throats is difficult because there is no unambiguous geometrical definition of where a~~ pore~~ bubble ends and a connecting channel begins. Conceptually, the skeleton nodes correspond to~~ pore~~ bubbles~~(bubble) bodies~~, and the branches of the pore-space skeleton correspond to the channels (or paths) connecting the ~~pores~~bubbles. However, a typical pore/node correction has to be applied because several skeleton nodes may occur in the same ~~pore~~ bubble body (Lindquist 2002), as can be seen in Figures 1d and 1e. In this work, a criterion based on the isotropic inflation of spheres centered on each node was used. If two or more spheres overlap, they are considered part of the same ~~pore~~bubble. The number of identified~~ pores~~ bubbles is actually the number of independent clusters of overlapping inflated bubbles. The amount of inflation can be controlled and acts as a parameter for the merging criterion. The steps in this process are graphically shown in the example presented in Figures 1d-1h. An insufficient inflation value overestimates the number of pores, while the maximum inflation to fill the entire bubble might underestimate this value if several spurious branches result after skeletonization. In this work a level of inflation equal to 85% of the maximum was used. Variations around this value were also considered, and it was found that this parameter only weakly affects the computed values of the bubble and pore throat numbers and sizes, as seen in Figures 1f & g that present~~s~~ two examples with different levels of inflation.

Some concerns still remain for the throat size determinations; while very short branches are usually disregarded, because some maximal spheres centered at the skeleton nodes may completely enclose the short branches, incorrect channels may still be considered. Practically, this means that the throat-size distribution may present some large-valued outliers due to the consideration of branches that ~~do~~may not represent physical channels.

The final assessment of ~~pore~~ bubble~~(bubble)~~ size is based on the diameter of the maximal inscribed sphere placed~~centered~~ at~~on~~ the center of mass of the cluster of the overlapping inflated bubbles (Fig. 1h). The bubble number density was calculated by dividing the number of inscribed spheres (bubbles) identified after skeletonization by the investigated volume. The uncertainties in the numbers of bubbles and of pore throats can be estimated as the square root of the number of each object type counted by application of Poisson statistics.

The connectivity, β, is a standard topological property that measures the number of interconnections (in this study pore throats) between objects (in this case bubbles). Connectivity analysis of tomographic reconstructions was pioneered in studies of bone structure (Odgaard and Dundersen 1993) and of porous media (Thovert et al. 1993). Following these two publications ~~To measure β~~ we ~~calculated the first Betti number following Thovert et al. (1993) and then divided that value by the sample volume to~~

~~measure~~calculate the connectivity per unit volume (mm^3 in this study), β or connective density, as done by Odgaard and Gundersen (1993) using:

$$\beta = \frac{\#\text{ pore throats} - \#\text{ bubbles} + 1}{\text{sample volume}}. \quad (1)$$

This topological measure may yield both negative and positive values per unit volume. As an illustration, consider a simplified example of 4 bubbles in a volume of 0.5 mm^3. In the case of no interconnections, or pore throats, between the bubbles, the value of β is -6 mm^{-3}. In cases where only single connections are allowed between bubbles (i.e., two pore throats cannot connect the same two bubbles), a system with two interconnections yields a β value of -2 mm^{-3}, if there are three interconnections β = 0 mm^{-3}, and if there are four β = 2 mm^{-3}. Thus, a β value of 0 mm^{-3} is the minimum threshold at which the pore throats interconnect the bubbles in this example. This threshold value can exceed 0 if we relax the constraint that bubbles can only be connected by a single pore throat or that all pore throats must interconnect bubbles within the volume of interest. Following basic statistical rules, the uncertainties in the values of β are calculated from the uncertainty in the number of bubbles, δ bubbles, and the uncertainty in the number of pore throats, δ pore throats, and the sample volume by ~~by~~

$$\delta\beta = \frac{\sqrt{(\delta\text{bubbles})^2 + (\delta\text{pore throats})^2}}{\text{sample volume}}. \quad (2)$$

~~dividing the square root of the sum of the square of the uncertainty in the number of bubbles and the square of the uncertainty in the number of pore throats by the sample volume investigated.~~

Tortuosity in this research is defined as the average distance a particle would travel between two opposite sides of the sample by the pore network divided by the Euclidean~~Euclidian~~ distance between the opposite sides. The MATLAB® code TORT3D (Al-Raoush and Madhoun 2017) was used for all tortuosity measurements. The tortuosity was determined in three orthogonal directions and then averaged; the average values are reported in Table 2.

The 3D visualization of reconstructed and analyzedanalysed volumes was obtained by the commercial software VGStudio Max 2.0 (Volume Graphics).

Lattice-Boltzmann modeling of permeabilities

Because of the dynamic nature of the experiments and the collapse of the samples with loss of vesicularity near to, or at, their termination, sample permeabilities could not be measured directly. Instead, lattice-Boltzmann modeling of permeabilities was performed using a modified version of an established lattice-Boltzmann code (Hill et al. 2001; Hill and Koch 2002). Details of the permeability modeling applied to tomographic reconstructions can be found in Bai et al. (2010), in which the accuracy of the viscous permeabilities calculated by modeling was directly compared against measured permeabilities and shown to typically be within a factor of 11 for porosities from 0.05 to 0.87. Although, for porosities less than 0.50 the difference between measured and modeled permeability is less than a factor of 7.

Bai et al. (2010) demonstrated that the ratio of the tomographic reconstruction resolution (voxel edge length) to the lattice size (edge length of subvolume) and the simulation size could influence the calculated permeability. The resolution-to-lattice-size ratios used in this study are in the range where Bai et al. (2010) demonstrated that the value of the ratio had no effect of on the calculated permeability. Bai et al. (2010) studied five samples at different lattice sizes; in three samples they found that decreasing the lattice size below 762 μm increased the calculated permeability by a factor of less than 20. Two of these three samples that display a significant effect of lattice size on calculated permeability contained a giant bubble with a volume of more than 10^9 μm^3 and more than 3 orders of magnitude larger than the 2nd largest bubbles in the sample (Bai et al. 2008). This largest bubble was not spherical, but its equivalent radius (i.e., radius of an equivalent-volume sphere) was of the same order of magnitude as the recommended lattice size of Bai et al. (2010). We attribute the sensitivity of the calculated permeability in these samples of Bai et al. (2010) to the presence of the large bubble, and note that none of the samples in the present study contain such an anomalously large bubble. The third sample of Bai et al. (2010) that displays a significant lattice size effect does not contain an anomalously large bubble, but has a porosity of only 0.286. The aAnalysis of this sample of Bai et al.'s (2010) results indicatessuggests that using the smallest lattice size in this study (370 µm) may, at most, overestimate the permeability by a factor of ~ 3 for low porosity samples. The other, larger, simulations tested for the effects of lattice size on permeability determinations in Bai et al. (2010) demonstrateused in this study are expected to have uncertainties less than 20 % (Bai et al. 2010). no significant effect of lattice size (i.e., greater than ~20 percent). Based upon Bai et al. (2010), we apply an uncertainty of 20 percent to the permeability calculations, but recognize that for lower porosity samples the calculated permeabilities may be higher by a factor of 3.

Permeabilities in the three orthogonal directions of each subvolume were calculated. Because the maximum difference between the lattice-Boltzmann permeabilities measured in three orthogonal directions of the samples was less than a factor of 2, we concluded that there was no significant variation in the permeability as a function of direction and report no significant differences with respect to orientation were detected, the average of the permeability values for each sample is reported in Table 2. This lack of orientation effects supports the modeling of our samples as random networks of bubbles interconnected by pore throats.

Bubble growth during isobaric heating versus isothermal decompression

Experiments in this study were performed by isobaric heating at atmospheric pressure because a high-pressure furnace was not available on the TOMCAT beamline. The resulting time-temperature-pressure path in these experiments is distinctly different from bubble formation during near-isothermal decompression in natural systems and in many experiments (e.g., Burgisser and Gardner 2004; Lindoo et al 2016, 2017; Mueller et al. 2005; Spieler et al. 2004; Takeuchi et al. 2009).

Although bubble nucleation and growth during isothermal decompression and isobaric heating experiments are both driven by supersaturation of the melt with a volatile, the viscosity of the melt increases during isothermal decompression (due to water loss to the bubbles) and may either increase (due to water loss) or decrease (due to increasing temperature) during isobaric heating. For example, in these experiments the andesitic melt begins vesiculation at 900 °C with a water concentration of 5 wt% and a viscosity of ~ 750 Pa s (calculated following Giordano et al. 2008). If this melt lost all its water by the end of the experiment at 1100 °C, the viscosity would be ~ 6700 Pa s. Although it is difficult to estimate the water concentration in the melt during vesiculation, we estimate that approximately 1 wt% water remains in the melt at ~ 1000 °C, which would yield a melt viscosity ~ 3100 Pa s. During these experiments the diffusivity of water in the melt also is controlled by a combination of heating and dehydration. Using the equations of Ni and Zhang (2018), the water diffusivity at the start of vesiculation is expected to be ~ 3×10^{-13} m^2 s^{-1}, decreasing to ~ 1×10^{-14} m^2 s^{-1} when water is lost. On the contrary, for isothermal decompression at 1100 °C of the same melt composition, the viscosity would increase from 32 Pa s at the start of vesiculation to ~ 6700 Pa s if all of the water is exsolved from the melt, and the water diffusivity would decrease from ~ 3×10^{-12} m^2 s^{-1} to ~ 1×10^{-14} m^2 s^{-1}.

These differences in the history of the melt viscosity and diffusivity will influence the rates of bubble growth and coalescence of neighboring bubbles. Following Navon and Lyakhovsky (1998) the radius of an individual bubble during its initial stages of growth will be significantly affected by the melt viscosity:

$$r \propto exp\left[\frac{\Delta P}{4\eta}t\right], \quad (3)$$

where r is the bubble radius, ΔP is the supersaturation pressure, η is the melt viscosity, and t is the time. As the bubble grows and supersaturation decreases, the bubble radius is described by a law containing the square root of the product of the volatile diffusivity in the melt and time (Equation 36 of Navon and Lyakhovsky 1998). Melt viscosity also exerts control on the time necessary for interacting bubble walls to fail and coalescence to begin, τ_{df}:

$$\tau_{df} = \frac{3\eta r^2}{4\Delta P h_{min}^2}, \quad (4)$$

where h_{min} is the critical thickness at which the walls fail (Navon and Lyakhovsky 1998). Equations 3 and 4 demonstrate that the rates of bubble growth and coalescence during the early stages of isobaric heating experiments should be slower than those in isothermal decompression experiments because of the higher viscosities and lower water diffusivities in the melt early in the isobaric heating experiments. However, as both types of experiments reach the end of bubble growth and water loss, the rates at which bubble growth and coalescence occur should converge.

Both isothermal decompression and isobaric heating experiments are expected to produce similar, random bubble, or foam, structures, due to the stochasticity in both the location and timing of bubble nucleation in the melts. Because of the higher viscosities and lower diffusivities of isobaric heating experiments, the vesicularity and interconnectivity of bubbles (due to coalescence) may be expected to be smaller than in isothermal decompression experiments of similar, short durations (Equations 3 and 4). Because of these differences between isothermal decompression and isobaric heating experiments we did not study bubble growth and coalescence rates, but instead concentrated on the development of porosity and permeability of the foams, while fully recognizing that the values we determined may be minimal ones.

Despite the differences between isothermal decompression and isobaric heating experiments, we can make a comparison between the rates of magma ascent and the rates of degassing during isobaric heating experiments by dividing the melt supersaturation pressure (Table 2) by the duration of the isobaric heating (Table 2) to yield equivalent decompression rates of approximately 0.1 to 2 MPa s^{-1}. Although these equivalent decompression rates are only rough approximations, the low values are similar to decompression rates found by Ferguson et al. (2016) for eruptive products of Kilauea volcano and the high values to decompression rates found by Humphreys et al. (2008) for the May 18, 1980 plinian eruption of Mt. St. Helens.

Results

Visual observations

Bubble growth in the samples occurred rapidly at temperatures above 600 °C. Typical bubble nucleation and growth can be seen in Figure 2 and Supplemental Movie 1 of andesitic sample DRB2012-2a, which was heated from 600 °C to 1100 °C over a period of 10~~4~~0 s (Table 2). ~~No evidence of a significant nucleation delay (i.e., longer than a few seconds) was detected in any sample.~~ In the absence of nucleation delay, bubble~~Bubble~~ growth is presumed to occur once the sample temperature exceeds that of the glass transition. The onset of the glass transition temperatures for the samples studied can be estimated using the results of Giordano et al. (2005). The glass transition given in Giordano et al. (2005) for basaltic, trachytic and dacitic compositions determined at their most rapid heating rate of 0.333 K s^{-1} and water concentrations up to 2.5 wt.% were fit by a power-law, which was chosen because power-laws describe the effect of water addition on melt viscosity (e.g., Shaw 1972). The power-law fit reproduces the calibrating data to within a maximum of ~ 50 K, as well as reproducing the anhydrous andesite glass transition temperature of Neuville et al. (1993) that was not used in the calibration. We estimate a minimum onset of the glass transition in our samples with 3 wt% water (MORB, trachyandesite, and dacite) at 460 °C and in the andesite with 5 wt% water at 440 °C. However our heating rates were approximately 3 to 15 times more rapid than used in Giordano et al.'s experiments, thus the observed vesiculation temperatures were significantly above these minimum glass transition temperatures, in the range of 616 to 900 °C (Table 2). Although these delays may be attributable to a short nucleation delay, we interpret them as being due to our inability to observe the onset of bubble growth in real time during the experiments because of the small size of the initial bubbles. This inability to see the earliest bubbles made it difficult to measure samples at low porosities and only a few data at these conditions were obtained (Table 2).

Bubble growth was initially observed as a dense cloud of small bubbles that grew into larger, easily discernible, bubbles that rapidly became ~~an~~ interconnected ~~foam~~ (Fig. 2). Typically, these early growth rates were so rapid that they were blurred in the tomographic images, so meaningful quantitative measurements could not be made.

Visual inspection of the tomographic reconstructions revealed that early bubbles vary from ellipsoidal to sub-spherical, but within seconds all evolve into sub-spherical to spherical shapes. Bubble growth in all experiments on the basaltic composition was too rapid to quantitatively analyze those samples before termination of the experiment. However, in four cases we extracted limited data from the different stages of foam development (Table 2). Bubbles coalesced and typically grew to a maximum size, creating a foam with~~of~~ thin-walled bubbles. If the sample was not immediately quenched, the foam contracted and underwent partial collapse, and in some cases collapse occurred before the termination of the experiment. This behavior is attributed to the loss of volatiles, either through failure of the bubble walls or diffusion through them.

Not every tomographic reconstruction set could be used for all the quantitative analyses presented in the Methods section. In some cases, permeabilities could not be determined (e.g., DRB2012-6e-07) because of the large computer memory required to resolve the surface area of the interconnected bubbles.

Bubble number density (BND), bubble size distribution (BSD), and pore throat size distribution (PTD)

Table 2 presents a summary of our quantitative measurements, and the sizes of all bubbles and pore throats measured in the studied samples are provided as supplementary material (Table S1). All measurements reported in this study were made on volumes far from the edges of the samples and that displayed no visual evidence of anisotropy. The typical distance of the analyzed volume from the sample edges was approximately 500 μm. Because of the small sample volume, in some cases the number of bubbles and pore throats, as well as their range in size, are small (Table S1). In all but one case for the dacitic composition, DRB2012-6e-10, the largest bubble in the investigated volume was less than 6 % of the sample volume. In DRB32012-6e-10 the largest bubble was 31% of the volume.

In general, in each sample the~~The~~ bubble number densities~~ in the foams~~ tend to increase with porosity up to a maximum and decrease at higher porosity (Figs. 3-6, Table 2), although between any two steps the BND can decrease (Table 2). Increasing BNDs are attributed to continuous nucleation and decreasing BNDs to bubble coalescence.~~ The continuous nucleation is notable because many of these experiments were only slightly supersaturated with water by 35 MPa, although the andesite experiment was supersaturated by 168 MPa (Table 2). The basaltic foams reached the highest BND of 1.92 x 10^4 mm^{-3}, whereas the dacite had the lowest BND of only 4.01 x 10^3 mm^{-3} in its final step.~~

The measured bubble size and pore throat size distributions of the experiments~~al foams~~ are presented in Figures 3-6. Each figure presents a volume-normalized histogram of the sizes of either the bubbles or the pore throats. None of the distributions are Gaussian, but instead often display "long tails" to large bubble and throat sizes, a characteristic indicative of power-law distributions (Newman 2005). Although the bubble-size and throat-size distributions can be fit with power-laws, this was not done in this study due to the small size range of sizes in each distribution that results in large uncertainties in the calculated power-law exponent. Despite evidence that the sizes are power-law distributed, and therefore their means and standard deviations do not have the same significance as in Gaussian distributions (Newman 2005), each panel of each figure provides the mean diameter and the standard deviation of either the bubble diameter or pore throat diameter to allow comparison of the measurements with previous studies (e.g., Burgisser et al. 2017). The relative standard deviations about the mean bubble sizes and pore throats are in most samples greater than 25% and often near 50%. These large standard deviations are consistent with the non-Gaussian distributions of bubble and pore throat sizes (Newman 2005).

Bubbles measured in the basaltic composition reach a size of approximatelylmost 46200 µm in diameter, and the BNDs are in the thousands per cubic millimeter (Fig. 3a, Table 2). The two samples with the lowest porosities (0.52 and 0.50) are from the same experiment and demonstrate that with time the number of small bubbles in the 5 to 10 µm range increases, which indicates continuing bubble nucleation and growth, as does that of larger bubbles in the 40 to 70 µm range, which provides evidence of continued growth. The disappearance of bubbles in the size range of 55 to 60 µm of the second sample ($\Phi = 0.50$) is interpreted as a consequence of bubble coalescence, and its lower porosity is probably due to bubble collapse that occurred between these two heating experiments (Table 2). Comparison of the average bubble size in each experiment does not indicate any significant trend with porosity (Fig. 3a).

The number of pore throats in the basalt varies from about 6.40 x 10^3 mm^{-3} at the lowest porosity to approximately 7.22 x 10^4 mm^{-3} at the highest porosity. The two low-porosity (0.50 and 0.52) measurements of pore throats ~~from the same~~ experiment demonstrate only moderate increases in the number and size of pore throats (Fig. 3b, Table 2). The experiment with 0.55 porosity contains one pore throat that is anomalously larger then the next largest one (Fig. 3b), and our experimental techniques for measuring the pore diameter may produce large-valued outliers in the pore throat size distributions. Whereas we cannot completely discard the possibility that the largest pore throat in this sample is an artefact, we think that size difference between the largest pore throat and the others in the distribution (Fig. 3b) is not sufficiently large to discard the measurement. ~~However, growth in the number of smaller pore throats and loss of pore throats in the 45 to 50 µm size range are evident.~~ Because the basaltic results for the two highest porosity measurements (0.55 and 0.73) are from different experiments, it is difficult to investigate the evolution of BSD and PTD with increasing porosity. Nevertheless, if these two samples are interpreted as an evolutionary trend, there appears to be ~~a trend of~~ an increasing number of pore throats with increasing porosity (Fig 3b, Table 2).

In contrast to the basaltic experiments, all of the andesite data (Fig. 4a, b, c, Table 2) were collected from the same experiment; however the location of the sample volume quantified varied slightly between different time steps in order to choose the most representative volumes near the center of the samples and to avoid volumes containing motion artefacts and/or~~counting~~ anomalously large or small bubbles. The maximum bubble size was between 215 and 220 µm (Fig. 4c). All andesite BSDs are dominated by bubbles in the 5 to 20 µm size range~~; consequently between porosities of 0.17 to 0.59 the average bubble diameter only increases from 10.1 to 13.6 µm, and only reaches a maximum of 21.5 µm in the last experiment~~ (Fig. 4a, b, c). The large number of small bubbles in all but the final porosity is interpreted to reflect a process of continuing nucleation and growth of new bubbles. The appearance of larger bubbles, greater than 40 µm, at porosities above 0.41 is caused by the expansion of gas within them during heating, and by coalescence. Evidence of coalescence is seen in the decreasing number of intermediate-sized bubbles with the appearance of larger bubbles in the highest porosity samples (cf., Gaonac'h et al. 1996).

The PTD distributions demonstrate the growth of throat sizes and number with increasing porosity (Figs. 4d, e, f). ~~Because the number of pore throats is dominated by smaller ones, the average throat diameter only increases from 8.0 to 10.6 µm in the experiment; however t~~The largest~~ pore ~~ pore throat size grows from 10-15 µm to a maximum of 50-55 µm. In comparison to the basalt, there are fewer pore throats greater than 30 µm.

The BSDs for the trachyandesite at the two highest porosities display broad peaks in the distribution without long tails to large bubble sizes seen in some of the andesite and basalt BSDs (Fig. 5a, Table 2). ~~are much more evenly distributed for sizes above 10 µm, with the exception of~~ The~~the~~ lowest porosity sample had~~with~~ only a single bubble and no pore throats in a volume of 0.0506 mm^3 (Fig. 5a, b, Table 2). ~~The average bubble size grows from 8.2 to 46.2 µm with increasing porosity, and t~~The maximum bubble measured was in the 95 to 100 µm size class. Although no bubbles less than 10 µm were observed at a porosity of 0.61, one appears at $\Phi = 0.64$, suggesting~~providing evidence of~~ continuing bubble nucleation. Bubble coalescence between the same two porosities is indicated by the decreasing number of bubbles with sizes between 10 and 75 µm and increasing numbers of larger-sized bubbles in the same sized volume (Fig. 5a).

The PTDs of the trachyandesite show a growth in the density of pore throats between 0.30 and 0.61 porosity followed by a decline in densities between 0.61 and 0.64 porosity with an increase in the number of larger pore throats (Fig. 5b.).~~ The average size of the pore throats are similar to the other compositions studied, and only vary from 8.1 to 10.3 µm.~~

The dacite BSDs demonstrate the growth of larger bubbles with increasing porosity, up to a maximum of almost 400 µm at Φ = 0.84 (Fig. 6a).~~ The change in the BSDs with porosity results in the average bubble diameter increasing from 11.4 µm to 25.9 µm at the highest porosity.~~ Bubbles in the size range of 10 – 15 µm increase in number between porosities of 0.38 and 0.79, and subsequently decrease as larger bubbles appear at higher porosities, a behavior we attribute to coalescence (cf., Gaonac'h et al. 1996).

The PTDs of the dacitic sample demonstrate growth of larger pore throats up to a porosity of 0.87 followed by a decrease in ~~that value as the sample~~ porosity at the end of the experiment to~~reached Φ =~~ 0.84 (Fig 6b). Although the largest pore throats reach 70 µm, the distributions are dominated by smaller pore throats~~ that result in average pore-throat diameters only increasing from 7.9 to 10.9 µm with growing porosity~~. The loss of the large pore throats seen in the distribution for Φ = 0.84 is associated with the growth of the large bubbles in this sample (Fig. 6a), which are presumed to have incorporated the larger pore throats into them during growth.

Connectivity, coordination number, and tortuosity

In all cases, the connected porosity is similar to the total porosity (Table 2); however the connectivity, β (Eqn. 1), varies significantly (Table 2, Supplementary Fig. 1). The β values in each type of foam increase from ~~values in the~~ hundreds to thousands per cubic millimeter with increasing porosity (Table 2) up to maximums in the tens to hundreds of thousands per cubic millimeter and then, with the exception of the basaltic composition, decrease at higher porosities (Table 2). This trend is similar to those observed for the BNDs and the PTDs (Table 2, Figs. 3-6).

The average coordination number (or number of interconnected bubbles surrounding a specified bubble) for each porosity (Table 2) of an individual melt composition is similar and varies between ~ 4 and 6, with a few outliers reaching values near 7 (DRB2012-7c-f, DRB2012-2a-18, DRB2012-6e-10) and one almost reaching 8 (DRB2012-2a-19). These average values are far below the maximum value of equal-volume, deformable bubbles surrounding a central bubble (the kissing number) of 32 (Cox and Graner 2004). However, the standard deviations about the average for each sample are often as large as, or even larger than, the mean, and the maximum coordination numbers are often near 100 and can reach almost 600 (Table 2). The bubbles with such high coordination numbers are large and surrounded by a network of small bubbles. (A two-dimensional image of such a bubble can be seen in Fig. 1.) Such high values of the kissing number are not inconsistent with simulations of polydisperse foams that display average coordination numbers between 11 and 14, but contain some foam polyhedra with coordinations approaching 100 (Kraynik et al. 2004).

The tortuosity, τ, of the foams varies from a low of 1.09 (dacites DRB2012-06e-8 and DRB2012-6e-9) to a high of 1.72 (andesite DRB2012-2a-9); however, most tortuosity values fall between 1.1 and 1.3 (Table 2). The relationship between increasing porosity and decreasing tortuosity in the studied samples can be described by (cf., Wright et al. 2009, Degruyter et al. 2010):

$$\tau = (1.0487 \pm 1.0201)(\Phi)^{-0.3192 \pm 0.0252}, \qquad (5~~2~~a)$$

and a correlation between increasing connectivity and decreasing tortuosity was also found:

$$\tau = (2.4376 \pm 1.1044)(\beta)^{-0.0687 \pm 0.0102}. \qquad (5~~2~~b)$$

Although the uncertainties in the fitting parameters are large, these equations provide useful relationships between these different measures of foam properties, as will be shown below.

Permeability

The lattice-Boltzmann (LB), viscous permeabilities, k_1, of the samples vary from 3 x 10^{-15} to greater than 5 x 10^{-11} m^2 (Table 2, Fig. 7). ~~However, our~~Note that simulations ~~failed~~ for ~~two~~one sample~~s,~~

~~(~~DRB2012-6e-7~~, EFJ-8a-06),~~ failed due to its extraordinarily fine structure, ~~and~~so ~~their~~its permeability could not be determined~~ using lattice-Boltzmann simulations~~ (discussed above). Another sample, EFJ08a-06, had only one bubble and its permeability also could not be determined.

The data sets in Figure 7 were fit with a power law because both the Carman-Kozeny relation (Carman 1937) and percolation theory (Stauffer and Aharony, 1994) predict a power-law relationship between porosity and permeability. Formally, the percolation theory relationship is expected to be $k_1 \sim (\Phi - \Phi_c)^{\mu}$, where, k_1 is the viscous permeability, Φ_c is the critical porosity threshold where the sample becomes permeable, and μ is an exponent that depends upon the system dimensionality (Stauffer and Aharony, 1994). The critical porosity threshold for monodisperse spheres in three dimensions is ~ 0.29 (Domb 1972; Lorenz and Ziff 2001); however, as discussed in detail below, the critical porosity threshold is a function of the size distribution and shape of the vesicles. Permeability thresholds in natural and experimental magmatic foams can vary from below ~0.03 (e.g., Saar and Manga 1999; Bai et al. 2010) to values in excess of 0.63 (Takeuchi et al. 2008, 2009; Lindoo et al. 2016). The critical porosity threshold for any given sample is unknown, and the porosity-permeability relationships in some magmatic foams have been empirically fit with a power law of the form k_1=AΦ^B, where A and B are fitting constants (e.g., Klug and Cashman 1996; Bai et al. 2010), although in some other studies~~cases~~ the estimated critical porosity threshold (typically 0.3) has been included in permeability-porosity relationships (e.g., Saar and Manga 1999; Blower 2001; Rust and Cashman 2004, 2011).

Our most complete data set on the andesitic composition foam displays a power-law relationship between porosity, Φ, and LB permeability of $k_1 = 1.68x10^{-11}\Phi^5$ (Fig. 8). Assuming a critical porosity of 0.010 below the minimum porosity at which a LB permeability was determined~~measured~~, or 0.15, produces a percolation theory power law fit of $k_1 = 5.79x10^{-12}(\Phi - \Phi_c)^{2.1}$. At porosities up to ~ 0.60, the measurements are similar to the Bai et al. (2010) fit to permeabilities of silicic rocks measured by Klug and Cashman (1996). The LB permeabilities of andesitic foams at porosities greater than ~ 0.60 diverge from Bai et al.'s (2010) fit to silicic foams leading to an order of magnitude difference between the two at a porosity of 0.90 (Fig. 7).

The LB permeabilities~~permeability~~ of two basaltic foams at ~0.50 porosity~~-~~ bracket the fit to the andesitic foam but the LB permeability increases to a value that is an order of magnitude greater at a porosity of ~0.55. The permeability values at ~ 0.50 porosity (DRB2012-07a-3) may be artificially low because of bubble bursting that was observed at the end of previous experiment (DRB2012-07a-2), and some of the porosity and pore throats may have been lost. These measurements at 0.50 and 0.55 porosity were made on two different chips of basaltic melt; this complicates the interpretation because the two samples have slightly different time-temperature histories, which together with the bubble popping in the sample at 0.50 porosity may might create differences in foam porosity and permeability. Thus, we doubt that the factor of ten increase in permeability between ~ 0.50 and 0.55 porosity for these basaltic samples is significant. The LB permeabilities at 0.55 and 0.73 porosity are similar to those found by Bai et al. (2010) on a high-K composition basaltic foam from Stromboli, as shown by the fit to their data in Figure 7.

The trachyandesitic foam displays a unique behavior. At low porosities, near 0.30, its LB permeability is significantly above that of the andesit~~e~~ic experiment, but at higher porosities the LB permeability falls to values similar to the andesitic composition (Fig. 7).

The LB permeability of the dacitic composition at 0.79 porosity cannot be distinguished from that of the similarly porous andesit~~e~~ic experiment, but the two higher porosity dacitic foams ~~surprisingly~~ display significantly higher LB permeabilities than expected from the trend described by the lower porosity dacitic and andesitic ~~foam~~experiments~~s~~ (Fig. 7).

~~An obvious and significant difference in the physical properties of the studied compositions is their~~

~~viscosity (Table 1). However, a simple correlation between melt viscosity and permeability at a specific porosity does not exist. The lack of such a correlation is illustrated by the permeability determinations of the trachyandesitic foam at 0.35 porosity and the two highest permeabilities of the dacitic foams (Fig. 7). Although the viscosities of the melts that form these trachyandesitic foams, either with their initial water concentration or anhydrous (Table 1), are at least an order of magnitude higher than basaltic melts, their permeabilities are similar to those of basaltic foams. Comparison of melt viscosities with the average pore-throat diameters in the foams (Figs. 3-6) does not provide clear evidence of a positive correlation between these two properties (cf., Polacci et al. 2014).~~

The experimental results demonstrate that both average bubble sizes and pore throat sizes increase with increasing vesicularity; however, the increase in pore throat sizes is less than that of the bubbles (Figs. 3-6). The maximum bubble sizes are observed in the dacitic composition, reaching nearly 400 μm in diameter, whereas the maximum bubble sizes for the basaltic, andesitic, and trachyandesitic compositions are 180, 220, and 100 μm, respectively. The maximum throat diameters are near 100 μm in the basaltic foam, but only 55 μm in the andesitic foam, 35 μm in the trachyandesitic foam, and 65 in the dacitic foam. Increasing vesicularity increases connectivity and decreases tortuosity. All of these changes in foam structure result in higher permeabilities that are not simply related to the melt compositions investigated.

Discussion

Permeability is not a simple function of porosity

Porosity is often considered the primary control of permeability; in most cases increasing porosity results in higher permeabilities (e.g., Fig. 7), but it has long been understood that other variables such as bubble sizes, composition, connectivity, pore throat diameter, tortuosity etc. significantly influence permeability (e.g., Carman 1937; Archie 1942; Rust and Cashman 2004; Mueller et al. 2005; Bai et al. 2010; Degruyter et al. 2010; Polacci et al. 2012, 2014; Lindoo et al. 2016; Burgisser et al. 2017; Colombier et al. 2017). ~~Our results demonstrate that at ~ 0.5 porosity basalts can have permeabilities similar to andesites, and at porosities approaching 0.9 the permeabilities of basalts and dacites are similar (Fig. 7).~~

An obvious and significant difference in the physical properties of the studied melt compositions is their viscosity (Table 1). However, a simple correlation between melt viscosity and permeability at a specific porosity does not exist. The experimental results using crystal-free samples demonstrate that at ~ 0.5 porosity basalts can have LB permeabilities similar to andesites, and at porosities approaching 0.9 the lattice-Boltzmann permeabilities of basalts and dacites are similar (Fig. 7) despite these melts displaying orders-of-magnitude differences in their viscosities (Table 1). Comparison of melt viscosities with the average pore-throat diameters (Figs. 3-6) does not provide clear evidence of a positive correlation between these two properties either (cf., Polacci et al. 2014).

~~Thus, o~~Our study provides no evidence that composition alone controls the permeability-porosity relationship. Connectivity also does not provide a simple predictor of permeability, as evidenced by an order of magnitude difference in the lattice-Boltzmann permeability of samples with similar connectivity and porosity (Table 2, Fig. 7, Supplementary Figure 1). Tortuosity also does not appear to directly correlate with the porosity-permeability relations of the ~~foams~~samples studied (Table 2). However, the bubble- and pore throat-size distributions (Figs. 3 – 6) suggest that larger ~~pores~~ bubbles and larger pore throats play a significant role in influencing the permeabilities of magmatic foams. Before quantitatively investigating the role of bubble- and pore throat sizes in controlling the permeability of magmatic foams, we ~~first~~ compare our results with those from previous studies.

Porosity-permeabilityPorosity- permeabilty trends compared to previous determinations

Our lattice-Boltzmann permeability determinations are compared with many previous measurements of porosity and permeability from aphyric to low-crystallinity natural and experimental samples in Figure 8. These data plotted in Figure 8 were taken from published studies to illustrate the distribution of measured permeabilities and porosities. The lattice-Boltzmann permeability determinations of the experiments in this study are consistent with previous measurements of similar composition samples (Fig. 8), even though in some cases our experimental samples are orders of magnitude smaller than natural samples. At any given porosity the combined data set demonstrates that permeability can vary by orders of magnitude; nevertheless, the data define significant trends as porosity increases from negligible values up to near 1.0 (Fig. 8).

At low porosities, the few permeability determinations in the region of 0.02 to 0.18 porosity show no evidence of significant compositional dependence at equivalent porosity (Fig. 8). Most viscous permeabilities increase from ~10^{-17} m^2 at porosities near 0.01 to ~10^{-13} m^2 at 0.20 to 0.30 porosity, although some rhyolites at these porosities have permeabilities of only 10^{-15} m^2 (Fig. 8). At porosities above ~0.3, the sphere percolation threshold (Lorenz and Ziff 2001), the permeabilities continue to increase but at a slower rate than observed at lower porosities (Fig. 8). For porosities between 0.5 and 0.9, the permeabilities in Figure 8 range from values as low as ~ 10^{-14} m^2 (Lindoo et al. 2016) to as high as 10^{-10} m^2 (Bai et al. 2010). The slow increase in permeability at porosities above 0.3 suggests that once a permeable pathway is created, the addition of other pathways for gas transport at higher porosities (as shown by higher values of β and lower values of tortuosity) increases the permeability much less significantly than the first pathway. Most lattice-Boltzmann permeabilities measured in this study are near the center of the trend in Figure 8, with the exceptions of the highest permeability basaltic and dacitic melts., and some basaltic samples with only a few percent porosity have permeabilities between 10^{-14} and 10^{-12} m^2 (Fig. 8).

At porosities from 0.18 to 0.30 the permeability-porosity curves begin to flatten (Fig. 8). The extensive data sets of Farquharson et al. (2015) and Kushnir et al. (2016) on andesitic compositions create a sub-horizontal swath in Figure 8, but are consistent with a trend of increasing permeability for porosities from 0.18 to 0.30. Interestingly, these two studies of andesite each demonstrate almost a two order-of-magnitude variation in permeability at similar porosities (Fig. 8). Our permeability determinations on the andesitic melt show an order-of-magnitude increase in permeability from 0.17 to 0.33 porosity.

The trachyandesitic sample with 0.35 porosity has a permeability close to the value predicted by the Bai et al. (2010) basalt line (Fig. 7). The observation that this foam containing 58 wt.% SiO_2 has a permeability more similar to basaltic compositions than other foams with similar compositions (Table 1) is inconsistent with a model that simply uses melt composition or melt viscosity to explain the porosity-permeability relationship (e.g., Bai et al. 2010). The trachyandesitic foam with 0.35 porosity is notable for its high bubble number density and pore throat density, which appears to account for its high permeability (Fig. 5a, b).

In general, silicic foams have lower permeabilities and mafic foams higher permeabilities, but the dacitic foams with greater than 0.80 porosity measured in this study have lattice-Boltzmann permeabilities similar to basaltic foams with similar porosities (Saar and Manga 1999; Bai et al. 2010). Rust and Cashman's (2004) permeabilities of rhyolite, pumice and obsidian as well as Farquharson et al.'s (2015) permeabilities of pumiceous andesite demonstrate almost a two order-of-magnitude variation at similar porosities (Fig. 8). Thus the influence of composition on any porosity permeability relationship appears to be weak.

The porosity-permeability data set contains many determinations at porosities below the nominal critical value for mono-disperse spheres. Each specific sample may have its own critical porosity based upon the size distribution and shape of the bubbles and pore throats. Because of our lack of knowledge of the critical porosity for each sample, the data were fit by empirical power laws without including a critical porosity. Although the data in Figure 8 can be empirically fit with a single power law, $k_1 = 6.0x10^{-12}\Phi^{4.0}$, the dispersion of the permeabilities around this average fit is orders of magnitude at porosities from 0.15 to 0.90 (Fig. 8). The range of permeabilities displayed in Figure 8 also can be bound by two power-law fits. The lower bound is constrained by permeability measurements below 10^{-14} m^2: $k_1 = 1.5x10^{-14}\Phi^{1.8}$. The upper bound is dominated by the high permeability basaltic foams of Saar and Manga (1999) and of Bai et al. (2010), and can be described by a power law of $k_1 = 1.5x10^{-10}\Phi^{4.0}$. More than 90 % of the viscous permeability determinations in Figure 8, including those of this study, fall within the boundaries defined by these two power-laws.

Percolation theory can explain Tthe great increase in permeability between 0 and 0.30 porosity. seen for most permeability determinations can be explained by percolation theory. This theory predicts that at about 0.29 porosity an ensemble of inter-penetrating, equivalent diameter spheres that are randomly distributed in three-dimensional space will create a spanning, permeable network of connected porosity (Domb 1972; Lorenz and Ziff 2001). The permeability at porosities below 0.3 and the lack of permeability in some foams at porosities as high as ~ 0.86 (e.g., Takeuchi et al. 2008, 2009; Lindoo et al. 2016; Burgisser et al. 2017) maycan reflect the observations that statistical nature of the percolation threshold in finite systems, which does not necessarily occur at a specified porosity for a non-infinite system (Stauffer and Aharony 1994; Colombier et al. 2017). Possibly the permeabilities at low porosities are controlled by the percolation threshold for hard spheres, which has been determined at a porosity of 0.1938 (Ogata et al. 2005) or 0.1990 (Ziff and Torquato 2017). Another possibility is that a non-constant size distribution of bubbles will affect the percolation threshold. However, Consiglio et al. (2003)Ogata et al. (2005) and Ogata et al. (2005) demonstrated that the effect of the non-uniform size distributions they investigated on the percolation threshold was not significant for interpenetrating spheres and hard spheres, respectively.~~demonstrate that for either a uniform size distribution or a log-normal distribution the effect of size is minor and only decreases the percolation threshold of hard spheres by far less than one percent of the porosity for the size distributions they studied. Consiglio et al. (2003) investigated the percolation of inter-penetrating spheres of two different sizes and found that by varying the ratio of the two different-sized spheres the porosity at which percolation occurred could increase by less than 0.01 when compared to the results for spheres of a single size. Thus, the size distribution of spherical bubbles is expected to have a minor effect on the percolation threshold~~ However, Burgisser et al. (2017) demonstrated with their experimental samples that the separation distance between bubbles weighted by the polydispersity of the bubble sizes affected the percolation threshold.

On the other hand, bubble shape plays a significant role in controlling the percolation threshold. Garboczi et al. (1995) demonstrated that the continuum percolation threshold for randomly oriented, inter-penetrating, prolate ellipsoids decreased from the porosity value for spheres of 0.29 (e.g., Lorenz and Ziff 2001) to 0.26 for an aspect ratio of 2, to 0.18 for an aspect ratio of 4, to 0.09 for an aspect ratio of 10, to 0.007 for an aspect ratio of 100, and to 0.0001 for an aspect ratio of 500. Thus, the presence of a small fraction of ellipsoidal bubbles (e.g., tube pumices) or cracks in a sample ~~(e.g., tube pumices)~~ could provide an explanation of the permeabilities of volcanic foams whose porosities are below the percolation threshold for mono-disperse spheres.

~~Almost all permeability determinations for porosities between 0.30 and 0.50 cluster between 10^{-14} and 10^{-12} m^2 (Fig. 8). Each individual study of permeability-porosity relationships plotted in Figure 8 shows only modest increases (one to two orders-of-magnitude) in permeability between 0.30 and 0.50 porosity, and then only about an order-of-magnitude increase between 0.50 and the maximum porosity~~

studied (typically between 0.80 and 0.90 porosity). The permeabilities of the studied andesitic and trachyandesitic foams in this porosity region display only modest increases; however, the basaltic foams have an apparent factor of ten increase in the permeability between ~0.50 and 0.55 porosity (Table 2, Fig. 7). Note that these measurements were made on two different chips of basaltic melt; which complicates the interpretation because the two samples have slightly different time-temperature histories, and bubble popping was observed in the experiment with 0.50 porosity, both of which might create small differences in foam porosity and permeability. Thus, we doubt that the factor of ten increase in permeability between ~ 0.50 and 0.55 porosity for these basaltic samples is significant.

The slow increase in permeability at porosities above the percolation threshold at ~ 0.3 indicates that once a permeable pathway is created, the addition of other pathways for gas transport at higher porosities (as shown by higher values of β and lower values of tortuosity) increases the permeability much less significantly than the first pathway.

For porosities between 0.5 and 0.9, the permeabilities in Figure 8 range from values as low as ~ 10^{-14} m^2 (Lindoo et al. 2016) to as high at 10^{-10} m^2 (Bai et al. 2010). In general, silicic foams have lower permeabilities and mafic melts higher permeabilities, but the dacitic foams with greater than 0.80 porosity measured in this study have permeabilities similar to basaltic foams with similar porosities (Saar and Manga 1999; Bai et al. 2010).

The porosity-permeability data set contains many determinations at porosities below the nominal critical value for mono-disperse spheres. Each specific sample may have its own critical porosity based upon the size distribution and shape of the bubbles and pore throats in the sample, as discussed above. Because of our lack of knowledge of the critical porosity for each sample, the data were fit by empirical power laws without including a critical porosity. Although the data in Figure 8 can be empirically fit with a single power law, , the dispersion of the permeabilities around this average fit is orders of magnitude at porosities from 0.15 to 0.90 (Fig. 8). The range of permeabilities displayed in Figure 8 also can be bound by two power-law fits. The lower bound is constrained by the low porosity, low permeability measurements of Saar and Manga (1999) on basaltic foams, and rhyolitic porosities and permeabilities determined by Lindoo et al. (2016) and Burgisser et al. (2017): . The upper bound is dominated by the high permeability basaltic foams of Saar and Manga (1999) and of Bai et al. (2010), and can be described by a power law of . More than 92% of the viscous permeability determinations in Figure 8, including those of this study, fall within the envelope of these two power-law equations.

Although these simple power-law relationships between porosity and permeability supportAlthough percolation theory and the simple power-law relationships between porosity and permeability support the expected relationship between these two foam properties, permeability variations of up to 4 orders-of-magnitude at similar porosities clearly indicate that, in addition to porosity, there are other properties of the foams, such as the size distributions of bubbles and pore throats, influencing their permeability, as discussed above.

A further control on permeability-porosity relations is the presence of crystals. Both crystallinity and bubble anisotropy have been shown to influence the permeability of natural and experimental magmatic foams, however these influences were not investigated in this study. Degruyter et al. (2010), Schneider et al. (2012), and Burgisser et al. (2017) provide multiple examples of the effects of preferred bubble orientation on magma permeability. The effect of crystals was not investigated in this study, but interested readers can find research on permeability development in crystal-bearing magmatic foams was investigated experimentally in Bai et al. (2011) and Lindoo et al. (2017). Nevertheless, the permeabilities of crystal-rich magmatic samples determined by Saar and Manga (1999), Mueller et al (2008), Bai et al. (2011), Farquharson et al. (2015), Kushnir et al. (2016), and

Lindoo et al. (2017) also plot in the same region as the aphyric-to-low-crystallinity samples, but are not shown in Figure 8.

Comparison of measurements with the models of Degruyter et al. (2010) and Burgisser et al. (2017)

The complexity of the relationship between porosity and permeability displayed in Figure 8 has been noted before by many authors, and many models for the calculation of permeability have been constructed and demonstrated to reproduce the results of the individual studies (e.g., Saar and Manga 1999; Mueller et al., 2005; Polacci et al., 2008; Bai et al., 2010; Degruyter et al., 2010; Lindoo et al., 2016; Burgisser et al. 2017; LaSpina et al. 2017). Most recently, Burgisser et al. (2017) developed a model for permeability calculations based on modifications and extensions of concepts and equations developed in Degruyter et al. (2010) and successfully applied their new model to multiple data sets.

Burgisser et al. (2017) used a modification of the channel-based Carman-Kozeny relationship to model viscous permeability:

$$k_1 = \frac{\Phi_c^n d_t^2}{16\chi\tau^2}, \qquad (6~~3~~)$$

where ϕ_c^n is the connected porosity raised to the nth power, d_t is the characteristic diameter of pore throats, χ is the channel circularity:

$$\chi = \left(\frac{r^2}{l^2} + \frac{l^2}{r^2}\right), \qquad (7~~4~~)$$

where r is the equivalent circle radius of the throat and l is its major axis (χ = 2 for circular pore throats, Degruyter et al. 2010), and τ is the tortuosity. Degruyter et al. (2010) set n = 1 in this equation for their study, but Burgisser et al. (2017) fit their data with this equation and determined a value of n =

2.49. Burgisser et al. (2017) found that this fit reproduced 26 of their 28 viscous permeability measurements to within one log unit.

Equation 6~~3~~ was applied to the ~~foam~~samples produced in this study for which the appropriate variables were measured (Table 2) to predict permeabilities using both the value of n = 1 from Degruyter et al. (2010) and of n = 2.49 from Burgisser et al. (2017); in both applications the value of χ was set to 2 (Degruyter et al. 2010). The quality of the model fit to the data was assessed by calculating chi-squared as defined by:

$$\text{chi} - \text{squared} = \sum \frac{(\log[\text{calculated permeability}] - \log[\text{measured permeability}])^2}{((\log[\text{measured permeability}]))}. \quad (8\sout{5})$$

Application of the Degruyter et al. (2010) formulation of Equation 6~~2~~ with d_t equaling~~equalling~~ the average pore-throat diameter, χ = 2 and n = 1 predicted the permeabilities of 17 out of 23 permeability determinations to within 1 log unit (all were within 1.6 log units) and produced a chi-squared value of 1.13 (Fig. 9a). With Burgisser et al.'s (2017) value of n = 2.49, 19 permeability predictions were within 1 log unit of our determinations (all were within 1.4 log units), and the chi-squared value was 1.14 (Fig. 9a). The fit of these models to the measurements of this study is impressive when considering the almost 5 orders of magnitude spread in the lattice-Boltzmann ~~measured~~ permeabilities; however the trend between predicted and measured permeabilities is at high angles to the slope of the perfect 1:1 correlation line between model and measurement (Fig. 9a), indicating the need for further model ~~improve~~refinement.

Toward a better model of the viscous permeability of magmatic foams by considering the largest pore throat area

We wish to improve upon the models of Degruyter et al. (2010) and Burgisser et al. (2017) using the lattice-Boltzmann permeabilities found in this study. However, there are three caveats that must be considered for the model discussed below. The first is that the model is only calibrated for permeabilities between ~ 10^{-15} and 10^{-10} m^2. The second is that we have no technique to determine when an individual sample becomes permeable, although we can approximate the permeability threshold at Φ ~ 0.3 (the percolation threshold for interpenetrating spheres) or use the methods presented in Burgisser et al. (2017) to estimate the permeability threshold if no other information is available. The third caveat is that the model is probably only applicable to isotropic, or nearly isotropic, samples.

Fluid conductivity in porous media can be related to a random resistor network by application of percolation theory (Stauffer and Aharony 1994; Blower et al. 2001). Applying this paradigm, the porous network~~ in foams~~ can be envisioned as resistors interconnected to one another that ~~o ~~create a continuous circuit~~ that~~ when the permeability threshold is exceeded and ~~allows ~~fluid can~~to~~ flow across the sample. The connections between resistors in the network can be either in parallel or in series (Stauffer and Aharony 1994; Blower et al. 2001). The conductivity of the network is related to the specifics of the pore throat cross-sectional area, as expressed in the numerator of the Carma~~e~~n-Kozeny relationship as the square of the characteristic throat diameter, d_c^2 (Equation 6~~3~~). Given a complete description of the lengths and diameters of the pore throats, together with detailed information about their connections in either series or parallel sub-circuits, a complete model of sample permeability should be calculable, but these data are not available. ~~Such a calculation would be tedious and we do not have all of the information required to solve the necessary equations. ~~However, by making the simplifying assumption that the largest pore throat dominates the permeability (as the minimum-valued resistor in a parallel circuit dominates the current flow), the width of that throat, d_{max}, can be used as the characteristic pore throat diameter in Equation ~~3~~6. Support for the idea of parallel connections between bubbles is provided by the high values of the connective density, ranging from 10^3 to 10^4 mm^{-3} (Table 2). Replacing the average throat diameter with the maximum throat diameter, and leaving $\chi = 2$, in Equation 6~~3~~ did not significantly improve the fit of either the Degruyter et al. (2010) or Burgisser et al. (2017) models; however the Burgisser et al. (2017) model yielded calculated permeabilities consistently above the measured ones by a factor of 5. Based upon this observation, an empirical value of $\chi = 10$ (or a fitting factor of 5 times the original value of $\chi = 2$) was chosen, and the resulting fit of the Burgisser et al. model to the data is remarkable (Fig. 9b), with all but one of the measurements reproduced to within one log unit and a chi-squared value of 0.01. The Degruyter et al. (2010) model also reproduces all but one of the measurements to within 1 log unit, but yields a chi-squared value twice that of the Burgisser et al. model, 0.02.

The challenge in applying this model to predict permeability from porosity measurements is that the tortuosity and the maximum throat diameter needed for the calculation typically are not known (cf. Burgisser et al. 2017). In most cases, published studies only provide the average bubble diameter and the porosity. However, the relationship found in this study between tortuosity and porosity (Eqn. 5~~2~~a) can be used to estimate the tortuosity. Additionally, we found that the maximum throat diameter can be related to the average bubble size, d_{avg}^{bubble} (m), by

$$d_{\max} = 2.22251x10^{-5}\ln\left(d_{\text{avg}}^{\text{bubble}}\right) + 2.69501x10^{-4}. \qquad (9\sout{6})$$

To test this model, the permeabilities of samples within the range of our calibration, 10^{-15} to 10^{-10} m^2, from Bai et al. (2010) and the isotropic pumices of Burgisser et al. (2017) were estimated using the correlations between tortuosity and porosity and between the average bubble size and the maximum throat diameter (Fig. 9c). We did not apply the model to the non-isotropic samples of Burgisser et al. (2017) because we are unsure whether our correlations would apply to these samples and lack the necessary data to test our model on non-isotropic samples.

Although there is clearly a degradation in the accuracy of the model when the correlations are used to estimate the tortuosity and maximum throat diameter rather than their measured values (cf. Fig. 9c with Fig. 9b), the permeability of ~~permeability of~~ 11 of the 14 samples from Bai et al. (2010) are reproduced within 1 log unit, and the maximum difference between ~~the~~all estimated and measured permeabilities is 1.9 log units. The chi-squared value (Eqn. 8) for all of the Bai et al. (2010) and the model is 0.77. ~~The~~ The estimated permeabilities of all 13 isotropic samples from Burgisser et al. (2017) are within 0.9 of a log unit of the measured values, and the chi-squared value is 0.35. The accuracy of this model is similar to that reported by Burgisser et al. (2017) who found that their fit to Equation 6 could reproduce 26 out of the 28 (isotropic and anisotropic) samples they investigated to within 1 log unit.

This test of the model indicates its utility for estimating the permeability of samples with knowledge of only the porosity and the average bubble diameter. However, as shown in Figure 9c, the model has a tendency to overestimate the permeabilities by a factor of ~5. An ad hoc correction could be made for this overestimation, but even without such correction the test indicates that permeabilities can be calculated to within an order of magnitude with the model.

~~However, there are three caveats that must be considered. The first is that the model is only calibrated for permeabilities between ~ 10^{-15} and 10^{-10} m^2. The second is that we have no technique to determine when an individual sample becomes permeable, although we can approximate the permeability threshold at Φ ~ 0.3 or use the methods presented in Burgisser et al. (2017) to estimate the permeability threshold if no other information is available. The third is that the model is probably only applicable to isotropic, or nearly isotropic, samples.~~

Role of bubble growth rate on permeability

Although we were unable to successfully determine permeabilities at the same porosity from experiments with the same composition at different heating rates, our results agree ~~we concur~~ with previous studies indicating that bubble growth rates significantly influence permeabilities (Rust and Cashman 2004; Burgisser and Gardner 2004; Mueller al. 2005, 2008; Takeuchi et al. 2009; Castro et al. 2012; Lindoo et al. 2016). In particular, Lindoo et al. (2016) noted that increasing decompression rates in their experiments, leading to increasing bubble growth rates, resulted in an increasing percolation threshold. This hypothesis is consistent with two observations on the basaltic composition where the slowly heated experiment DRB2012-7f-10 (1 °C s^{-1}) with a porosity of 0.55 has a permeability (1.5 x 10^{-11} m^2) similar to the rapidly heated (6 °C s^{-1}), 0.73 porosity experiment DRB2012-7c-f (2.9 x 10^{-11} m^2), whereas the fit from Bai et al. (2010) predicts a permeability of at least 5 x 10^{-11} m^2 at a porosity of 0.73.

We also note that there may be a correlation between the bubble growth rate and the size distribution of pore throats that significantly influences permeability. We propose this tentative hypothesis because of the often-lower permeabilities of the rapidly heated (5 °C min^{-1}) andesitic foam in comparison to the more slowly heated (~1 °C min^{-1}) trachyandesitic and dacitic foams with similar porosities (Table 2, Figure 7).

Despite the need for further experiments to quantitatively constrain the effects of decompression and growth rates on the permeability of silicate foams, we suggest that the orders-of-magnitude variability seen in permeability at similar porosities in Figure 8 is significantly controlled by the bubble growth rate. The formation of a pore throat between two bubbles requires them to partially coalesce; for coalescence to occur the interbubble melt film (IBF) must thin to the point where it fails, estimated to be a thickness of 0.5 µm in a rhyolitic melt by Castro et al. (2012). The rate at which the IBF thins is a function of the surface tension and bubble size (Equation 4), and the timescales of thinning vary from less than a second (basaltic melts) to thousands of seconds (dacitic melts), based upon the analyses of Castro et al. (2012) and Nguyen et al. (2013). In the case where bubbles are growing on a timescale shorter than that of IBF thinning, coalescence is not as effective in creating large pore throats as at slower growth rates, and permeabilities at equal porosities are lower than in the case where bubble growth is slower than IBF thinning. Consideration of the lubrication and drag forces during bubble growth suggests the possibility of a bubble-size-dependence of connectivity (and therefore permeability). These considerations will be explored in future studies.

Although we think that the rate of gas exsolution plays a significant role in creating the wide spread of permeability at equivalent porosities, we recognize that other factors may affect the observed variations in permeability, such as the effects of bubble orientation (e.g., Degruyter et al. 2010; Burgisser et al. 2017) and the presence of crystals in the magma (e.g.~~cf.~~, Bai et al. 2011; Lindoo et al. 201~~6~~7).

~~*A brief discussion of inertial permeability*~~

~~Although the inertial permeability, k_2, was not investigated in this study, earlier studies have correlated the variation of k_2 with the viscous permeability, k_1. Note that such relationships exist because k_1 and k_2 are defined so that they are independent of the fluid (viscosity and density) and its flow regime (Reynolds number), i.e., k_1 and k_2 depend only on pore size and shape. Rust and Cashman (2004) found that for silicic foams~~

~~, (7)~~

~~whereas the measurements on pumice by Yokoyama and Takeuchi (2009) yielded~~

~~. (8)~~

Bai et al. (2010) provided the following relationship for basaltic foams:

, (9)

and Polacci et al. (2014) combined the available data and found

. (10)

Most recently, Burgisser et al. (2017) found a relationship almost identical to that of Rust and Cashman (2004):

. (11)

Burgisser et al. (2017) also demonstrated the similarity of their relation to previous measurements of viscous and inertial permeabilities.

Near $k_1 = 10^{-12}$ m^2, these relations (Equations 7-11) converge with a k_2 range of 1.5 orders of magnitude between the maximum of 7 x 10^{-8} m (Bai et al. 2010) and minimum of 2 x 10^{-9} m (Yokoyama and Takeuchi 2009). The calculated values of k_2 diverge at higher viscous permeabilities until a value of $k_1 = 10^{-10}$ m^2 at which the inertial viscosities vary by only by about ~2.5 orders of magnitude, from 4 x 10^{-7} m (Yokoyama and Takeuchi 2009) to 1 x 10^{-4} m (Rust and Cashman 2004). Application of Equation 11 allows the viscous permeabilities, such as those determined in this study, to be used to estimate the inertial permeabilities that are often needed for modeling gas flow in volcanic systems (e.g., Rust and Cashman 2004; Burgisser et al. 2017). However, a single relationship between k_1 and k_2 is unlikely to be applicable for all samples and without direct measurements of inertial permeabilities in samples under investigation the estimates may be inaccurate.

The competition between magmatic ascent and outgassing in magmatic systems

The experimental results demonstrate significant differences in the size distributions of bubbles and pore throats in the studied compositions. These morphological variations result in permeabilities that can vary by at least an order of magnitude as seen in the results of this study and by even greater values when previous studies are included (Fig. 8). The various permeability-porosity relationships shown in Figure 8 are expected to influence the ascent and eruption of magmas because of the role of gas in volcanic processes. To evaluate the significance of the differing permeability-porosity relationships on magma ascent we applied the model of Namiki and Manga (2008).

Although subvolcanic magma ascent and volcanic eruptions are driven by rapid volatile exsolution and formation of magmatic foams, expansion of volcanic foams increases their permeabilities, enhancing gas transport out of the magma and may slow, or possibly even stop, eruptions. This competition between the rapid expansion of magmatic foams and their loss of gas affects the intensity of volcanic eruptions. Combining the porosity-permeability relationships in Figure 8 with the steady-state model for volcanic eruptions of Namiki and Manga (2008), we investigated the conditions at which porous flow removes gas from basaltic and rhyolitic magmatic systems at rates greater than the transport of the magma caused by volatile exsolution and bubble formation.

Namiki and Manga (2008) constructed their model using a constant diameter magmatic conduit in which a water-bearing magma ascends at velocity v_o until the magma begins to vesiculate, causing the velocity to become a function of depth, v(z). The ratio $v(z)/v_o$ is calculated from mass conservation:

. (12)

The porosity as a function of depth, , is calculated by subtracting the water-saturation concentration at each pressure from the initial water concentration of the melt (2 % for basalt, 4 % for rhyolite in this study) to yield the exsolved water concentration, C_e. Water solubility in basalt was calculated from the results of Dixon et al. (2005) up to 70 MPa with the addition of a solubility value of 0.1 wt% H_2O for water saturation at 1 bar; water solubility for the rhyolitic system was calculated from the data of Silver et al. (1990) and Liu et al. (2008) for pressures to 180 MPa. These values were combined with the density of the melt, ρ_m (2800 kg m^{-3} for basalt and 2400 kg m^{-3} for rhyolite), and the density of water, ρ_w, to calculate :

, (13)

where ρ_w was calculated assuming ideal gas behavior for water at 1200 and 850 °C for the basaltic and rhyolitic systems, respectively. Pressure was converted to depth using:

, (14)

with $g = 9.8$ m s^{-2}. Namiki and Manga (2008) expand the depressurization rate of a parcel of magma as

, (15)

and they calculate permeable gas flow by (from Ingebritsen and Sanford 1998):

, (16)

where β is the gas compressibility (= 1/P for an ideal gas), k is the permeability, and η_g is the gas viscosity (10^{-5} Pa s). Combining Equations 15 and 14 produces the criterion that Namiki and Manga (2008) propose as a measure of efficient outgassing:

. (17)

To solve this equation, the second derivative of pressure with respect to depth can be replaced by

. (18)

To create an illustrative model, we considered an initial magma ascent velocity of 0.001 m s^{-1}, or about 0.1 km day^{-1}. This ascent rate is equivalent to the ascent rate of the andesitic experiment's estimated equivalent decompression rate (discussed in the Methods section) calculated for a constant density of 2400 kg m^{-3} and to the effusive ascent rates of natural magmas tabulated by Browne and Szramek

(2015). The porosity-permeability relationships of both the basaltic magma and rhyolitic magma were modeled with the three fits (upper bound, average, and lower bound) to the porosity-permeability data in Figure 8.

The results of the different cases considered are plotted in Figure 10, which displays the ratio of the gas velocity to the melt velocity as a function of depth for the basaltic and rhyolitic magma systems. The results of the low-permeability cases are unsurprising. The gas velocities in neither the basaltic magma nor the rhyolitic magma approach those of the melt, and therefore gas is not expected to be lost during ascent (Fig. 10). Although the average permeability fit displays a maximum v_{gas}/v_{melt} that is orders of magnitude higher than the low permeability fit, the calculations do not reach $v_{gas}/v_{melt} = 1$ (Fig. 10). The observation that the Namiki and Manga model predicts that foams whose permeability is defined by the average fit should not lose the gas driving their transport is consistent with the eruption of the many natural, vesicular samples for which porosity-permeability measurements constrain the average fit in Figure 8. With no loss of the vesiculating gas, the modeled magmas with either low or average porosity-permeability relations reach velocities similar to the explosive ascent rates of natural magmas tabulated by Browne and Szramek (2015) of 0.05 to 3 m s^{-1}.

The high permeability cases for both the basaltic and rhyolitic magmas display regions where the gas velocity exceeds that of the melt and has the potential to escape (Fig. 10), lessening or removing the driving force for volcanic eruptions. What is most surprising is that both melt compositions cross the critical v_{gas}/v_{melt} ratio of 1 and into the region of potential gas loss at low vesicularities, 0.07 and 0.12 for the basaltic and rhyolitic magmas, respectively, and maintain velocity ratios above 1 until vesicularities reach ~ 0.87 (Fig. 10). This modeling suggests that even low porosity magmas have the capacity to lose their driving gases if they are sufficiently permeable. The paucity of natural samples with porosity-permeability relationships similar to those of the high-permeability case is consistent

~~with this application of the Namiki and Manga (2008) model, which indicates that highly permeable foams probably lose the gas driving their ascent, stalling on the way to the surface.~~

~~The model of Namiki and Manga (2008) does not contain details of the geometry and mechanisms leading to ascent and eruption of magmas, nor does it consider possible loss of gas into the country rock surrounding the conduit (e.g., Chevalier et al. 2017). Gas lost to the conduit walls would imply a larger volume gas loss that would still affect the permeability-porosity relations of the magmatic foam. Such gas loss through the conduit walls would have implications on transitions in eruptive style. Thus, the fundamental results of the Namiki and Manga (2008) model appear sound. Only magmatic foams with the highest permeabilities at a given porosity (Fig. 8) are expected to enter the region where potential gas loss can occur (Fig. 10) and the driving force for further ascent and eruption will dissipate. Because of the correlation between bubble growth rate and permeability (discussed above), mechanisms that slow bubble growth rate are expected to increase permeability and potentially lead to the loss of gas through porous flow even at relatively low porosities (Fig. 10).~~

Conclusions

A complete characterization of magmatic foams is required to model permeability because permeability-porosity relationships alone do not provide sufficient data for accurate modeling and prediction. Furthermore, average properties of the foam, in particular average pore-throat diameters, appear to be insufficient to fully characterize permeability. Complete measurements of porosity, bubble and pore throat size distributions, as well as tortuosity, are required to model accurately the permeability of magmatic foams. In particular, we stress the apparent importance of the largest pore throat on the permeability of magmatic foams. We propose one such model, which we consider a step in the right direction, that can be used to benchmark future studies. ~~Combining t~~The results of this study are consistent with previous work indicatinges the importance of the bubble growth rate on the permeability of magmatic foams. Higher growth rates appear to produce lower permeabilities, and the effect of growth rate on permeability may explain a significant portion of the orders-of-magnitude spread in permeabilities at similar porosity. The model of Namiki and Manga (2008) is consistent with measurements of natural samples and predicts that only magmatic foams with the highest permeability values may lose the gases driving their ascent. Remarkably, this model demonstrates that gas loss can occur at small porosities as well.

Acknowledgements

D.R. Baker thanks NSERC for their continued support for his research through the Discovery Grant Program. All of the members of the TOMCAT team and of the Swiss Light Source at the Paul Scherrer Institut are thanked for their creation of the facility that allowed this study to be done and their continuing dedication to providing support to external users of the beamline.

We also thank the editor, KC. Cashman and the reviewers H. Wright, L. Chevalier and A. Burgisser for their detailed and thoughtful comments that significantly improved the presentation of our research in this contribution.

References

Al-Raoush RI, Madhoun IT (2017) TORT3D: A MATLAB code to compute geometric tortuosity from 3D images of unconsolidated porous media, Powder Tech 320: 99-107

Archie GE (1942) The electrical resistivity log as an aid in determining some reservoir characteristics. Trans Am Inst Mineral Meteorol 146:54-62.

~~Bai L, Baker DR, Rivers M (2008) Experimental study of bubble growth in Stromboli basalt melts at 1 atm. Earth Planet Sci Lett 267:533-547~~

Bai L, Baker DR, Hill RJ (2010) Permeability of vesicular Stromboli basaltic glass: Lattice Boltzmann simulations and laboratory measurements. J Geophys Res 115:B07201. doi:10.1029/2009JB007047

Bai L, Baker DR, Polacci M, Hill RJ (2011) In-situ degassing study on crystal-bearing Stromboli basaltic magmas: Implications for Stromboli Eruptions. Geophys Res Lett 38: L17309

Baker DR (2004) Piston-cylinder calibration at 400 to 500 MPa: a comparison of using water solubility in albite melt and NaCl melting. Am Mineral 89:1553–1556

Baker DR Eggler DH (1987) Compositions of anhydrous and hydrous melts coexisting with plagioclase, augite, and olivine or low-Ca pyroxene from 1 atm. to 8 kbar: application to the Aleutian volcanic center of Atka. Am Mineral 72:12-28

Baker DR, Polacci MR, LaRue A (2011) A study on the reproducibility of counting vesicles in volcanic rocks. Geosphere, doi: 10.1130/GES00553.1

Baker DR, Brun F, O'Shaughnessy C, Mancini L, Fife JL, Rivers M (2012) A four-dimensional X-ray tomographic microscopy study of bubble growth in basaltic foam. Nat Comm 3: 1135. doi:10.1038/ncomms2134

Blower JD (2001) Factors controlling permeability-porosity relationships in magmas. Bull Volcanol 63:497-504

Bouvet de Maisonneuve C, Bachmann O, Burgisser A (2008) Characterization of juvenile pyroclasts from the Kos Plateau Tuff (Aegean Arc): insights into the eruptive dynamics of a large rhyolitic eruption.

Bull Volcanol doi: 10.1007/s00445-008-0250-x

Browne B, Szramek L (2015) Chapter 9: Rates of magma ascent and storage. The Encyclopedia of Volcanoes. Elsevier Inc. http://dx.doi.org/10.1016/B978-0-12-385938-9.00009-2

Brun F, Dreossi D (2010) Efficient curve-skeleton computation for the analysis of biomedical 3D images. Biomed Sci Instrum 46:475-480

Brun F, Mancini L, Kasae P, Favretto S, Dreossi D, Tromba G (2010) Pore3D: A software library for quantitative analysis of porous media. Nucl Instr Methods Phys Res A 615:326-332

Burgisser A, Gardner JE (2004) Experimental constraints on degassing and permeability in volcanic conduit flow. Bull Volcanol 67:42–56. http://dx.doi.org/10.1007/s00445-004-0359-5

Burgisser A, Chevalier L, Gardner JE, Castro JM (2017) The percolation threshold and permeability evolution of ascending magmas. Earth Planet Sci Lett 470:37-47

Carman PC (1937) Fluid flow through a granular bed. Trans Inst Chem Eng London, 15:150-156

Castro JM, Burgisser A, Schipper CI, Mancini S (2012) Mechanisms of bubble coalescence in silicic magmas. Bull Volcanol 74:2339–2352

~~Chevalier L, Collombet M, Pinel V (2017) Temporal evolution of magma flow and degassing conditions during dome growth, insights from 2d numerical modeling. J Volcan Geotherm Res 333-334:116 – 133~~

Colombier M, Wadsworth FB, Gurioli L, Scheu B, Kueppers U, Di Muro A, Dingwell DB (2017) The evolution of pore connectivity in volcanic rocks. Earth Planet Sci Lett 462:99-109

Consiglio R, Baker DR, Paul G, Stanley HE (2003) Continuum percolation thresholds for mixtures of spheres of different sizes. Physica A 319:49-55

Cox SJ, Graner F (2004) Three-dimensional~~Three-dimenstional~~ bubble clusters: Shape, packing, and growth rate. Phys Rev E 69: 031409

~~Dixon JE, Stolper EM, Holloway JR (2005) An experimental study of water and carbon dioxide solubilities in mid-ocean ridge basaltic liquids. Part I: Calibration and solubility models. J Petrol 36:1607-1631~~

Degruyter W, Bachmann O, Burgisser A (2010) Controls on magma permeability in the volcanic conduit during the climatic phase of the Kos Plateau~~Pleateau~~ Tuff eruption (Aegean Arc). Bull Vulcanol 72:63-74

Domb C (1972) A note on the series expansion method for clustering problems. Biometrika 59:209-211

Dowd B, Campbell GH, Marr RB, Nagarkar V, Tipnis S, Axe L, Siddons DP (1999) Developments in synchrotron x-ray computed tomography at the National Synchrotron Light Source. Developments in X-Ray Tomography II, Proc SPIE 3772:224-236

Fagents SA, Gregg TKP, Lopes RMC (2013) Modeling Volcanic Processes: The Physics and Mathematics of Volcanism. Cambridge University Press, Cambridge, 421 p

Farquharson J, Heap MJ, Varley NR, Baud P, Reushclé T (2015) Permeability and porosity relationships of edifice-forming andesites: A combined field and laboratory study. Jour Volcan Geotherm Res 297:52-68

Ferguson DJ, Gonnermann HM, Ruprech P, Plank T, Hauri EH, Houghton BF, Swanson DA (2016) Magma decompression rates during explosive eruptions of Kilauea volcano, Hawaii, recorded by melt embayments. Bull Volcanol 78:71

Fife JL, Rappaz M, Pistone M, Celcer T, Mikuljan G, Stampanoni M (2012) Development of a laser-based heating system for in-situ synchrotron-based x-ray tomographic microscopy, J. Synchrotron Radiation 19:352-358

Fortin M-A, Riddle J, Desjardins-Langlais Y, Baker DR (2015) The effect of water on the sulfur concentration at sulfide saturation (SCSS) in natural melts. Geochim Cosmochim Acta 160:100-116

Gaonac'h H, Lovejoy S, Stix J, Scherzter D (1996) A scaling growth model for bubbles in basaltic lava flows. Earth Planet Sci Lett 139:395-409.

Garboczi EJ, Snyder KA, Douglas JF, Thorpe MF (1995) Geometrical percolation threshold of overlapping ellipsoids. Physical review E 52:819-828

Giordano D, Nichols ARL, Dingwell DB (2005) Glass transition temperatures of natural hydrous melts: a relationship with shear viscosity and implications for the welding process. J Volcan Geotherm Res 142: 105-118

Giordano D, Russell JK, Dingwell DB (2008) Viscosity of magmatic liquids: A model. Earth Planet Sci Lett 278:123-134

Hildebrand T, Rüegsegger P (1997) A new method for the model-independent assessment of thickness in three-dimensional images. J Microscopy 185:67-75

Hill RJ, Koch DL,Ladd AJC (2001) The first effects of fluid inertia on flows in ordered and random arrays of spheres. J Fluid Mech 448:213–241. doi:Ziff10.1017/S0022112001005948

Hill RJ, Koch DL (2002) The transition from steady to weakly turbulent flow in a close-packed ordered array of spheres. J Fluid Mech 465:59–97. doi:10.1017/S0022112002008947

Humphreys MCS, Menand T, Blundy JD, Klimm K (2008) Magma ascent rates in explosive eruptions: Constraints from H_2O diffusion in melt inclusions. Earth Planet Sci Lett 270:25-40

~~Ingebritsen SE, Sanford WE (1998) Groundwater in Geologic Processes. Cambridge University Press, Cambridge~~

Klug C, Cashman KV (1996) Permeability development in vesiculating magmas: implications for fragmentation. Bull Volcan 58:87-100

Kraynik AM, Reinelt DA, van Swol F (2004) Structure of random foam. Phys Rev Lett 93: 208301, 10.1103/PhysRevLett.93.208301

Kushnir ARL, Martel C, Bourdier J-L, Heap MJ, Reushclé T, Erdmann S, Komorowski J-C, Cholik N (2016) Probing permeability and microstructure: Unravelling the role of a low-permeability dome on the explosivity of Merapi (Indonesia). Jour Volcan Geotherm Res 316:56-71

LaRue A (2012) Bubble size distributions and magma-water interaction at Eyjafjallajökull volcano, Iceland. M.Sc. Thesis, McGill University

La Spina G, Polacci M, Burton M, de’ Michieli Vitturi M (2017) Numerical investigation of permeability models for low viscosity magmas: Application to the 2007 Stromboli effusive eruption. Earth Planet Sci Lett 473:279-290. https://doi.org/10.1016/j.epsl.2017.06.013

Lindoo A, Larsen JF, Cashman KV, Dunn AL, Neill OK (2016) An experimental study of permeability development as a function of crystal-free melt viscosity. Earth Planet Sci Lett 435:45-54

Lindoo A, Larsen JF, Cashman KV, Oppenheimer J (2017) Crystal controls on permeability development and degassing in basaltic andesite magma. Geology 45: 831-834

Lindquist WB (2002) Quantitative analysis of three dimensional X-ray tomographic images. Proc. SPIE 4503:103-115

Lindquist WB, Lee SM (1996) Medial axis analysis of void structure in three-dimensional tomographic images of porous media. J. Geophys Res 101:8297-8310

Liu Y, Samaha N-T, Baker DR (2007) Sulfur concentration at sulfide saturation (SCSS) in magmatic silicate melts. Geochim Cosmochim Acta 71:1783-1799

Liu Y, Zhang Y, Behrens H (2005) Solubility of H_2O in rhyolitic melts at low pressures and a new empirical model for mixed H_2O-CO_2 solubility in rhyolitic melts. J Volcan Geotherm Res 143:219-235

Lorenz CD, Ziff RM (2001) Precise determination of the critical percolation threshold for the three-dimensional 'Swiss cheese' model using a growth algorithm. J Chem Phys 114:3659-3661

Marone F, Stampanoni M (2012) Regridding reconstruction algorithm for real time tomographic imaging. J Synchrotron Rad 19:1029-1037

Mokso R, Marone F, Stampanoni M (2010) Real time tomography at the Swiss Light Source. AIP Conf Proc 1234:87-90

Mokso R, Schlepuetz CM, Theidel G, Billich H, Schmid E, Celcer T, Mikuljan G, Sala L, Marone F, Schlumpf N, Stampanoni M (2017) GigaFRoST: The Gigabit Fast Readout System for Tomography. Jour Synchrotron Rad doi.org/10.1107/S1600577517013522

Mueller S, Melnik O, Spieler O, Scheu B, Dingwell DB (2005) Permeability and degassing of dome lavas undergoing rapid decompression: An experimental determination. Bull Volcan 67:526-538

Mueller S, Scheu B, Spieler O, Dingwell DB (2008) Permeability control on magma fragmentation. Geology 36:499-402

Navon O, Lyakhovsky, V, (1998) Vesiculation processes in silicic magmas. In: Gilbert, J.S., Sparks, R.S.J. (Eds.), The Physics of Explosive Volcanic Eruptions. Geol Soc Spec Pub Lond 145: 27–50.

~~Namiki A, Manga, M (2008) Transition between fragmentation and permeable outgassing of low viscosity magmas. J Volcan Geotherm Res 169:48-60~~

Neuville DR, Courtial P, Dingwell DB, Richet P (1993) Thermodynamic and rheological properties of rhyolite and andesite melts. Contrib Mineral Petrol 113:572-581

Newman MEJ (2005) Power laws, Pareto distributions and Zipt's law. Contemporary Physics 46:323-351

Nguyen CT, Gonnermann HM, Chen Y, Huber C, Maiorano AA, Gouldstone A, Dufek J (2013) Film drainage and the lifetime of bubbles. Geochem Geophys Geosys 14: 10.1002/ggge.20198

Ni H, Zhang L (2018) A general model of water diffusivity in calcalkaline silicate melts and glasses. Chem Geol 478:60-68.

Odgaard A, Gundersen HJG (1993) Quantification of connectivity in cancellous bone, with special emphasis on 3-D reconstructions. Bone 14:173-182

Ogata R, Odagaki T, Okazaki K (2005) Effects of poly-dispersity on continuum percolation. J Phs Condens Matter 17:4531-4538

Papale P, Moretti R, Barbato D (2006) The compositional dependence of the saturation surface of H_2O + CO_2 fluids in silicate melts. Chem Geol 229:78-95

Polacci M, Baker DR, Bai L, Mancini L (2008) Large vesicles record pathways of degassing at basaltic volcanoes. Bull Volcanol 70:1023-1029. https://doi.org/10.1007/s00445-007-0184-8

Polacci M, Baker DR, La Rue A, Mancini L, Allard P (2012) Degassing behaviour of vesiculated basaltic magmas: an example from Ambrym volcano, Vanuatu Arc. Jour Volcan Geotherm Res 233-234:55-64.

Polacci M, Bouvet de Maisonneuve C, Giordano D, Piochi M, Mancini L, Degruyter W, Bachmann O (2014) Permeability measurements of Campi Flegrei pyroclastic products: An example from the

Campanian Ignimbrite and Monte Nuovo eruptions. Jour Volcan Geotherm Res 2272:16-22.

Rivers ML, Wang Y (2006) Recent developments in microtomography at GeoSoilEnviroCARS. Developments in X-Ray Tomography V, Proc SPIE 6318:J3180. doi: 10.1117/12.681144

Rust AC, Cashman KV (2004) Permeability of vesicular silicic magma: Inertial and hysteresis effects. Earth Planet Sci Lett 228:93-107

Rust AC, Cashman KV (2011) Permeability controls on expansion and size distributions of pyroclasts. J Geophys Res 116:B11202

Saar MO, Manga M (1999) Permeability-porosity relationship in vesicular basalts. Geophys Res Lett 26:111-114

Schneider A, Rempel AW, Cashman KV. (2012) Conduit degassing and thermal controls on eruption styles at Mount St. Helens. Earth Planet Sci Lett 357-358: 347-354

Shaw HR (1972) Viscosities of magmatic silicate liquids: an empirical method of prediction. Am J Sci 272:870-893

~~Silver LA, Ihinger PD, Stolper E (1990) The influence of bulk composition on the speciation of water in silicate glasses. Con Min Petrol 104:142-162~~

Sparks RSJ (2003) Dynamics of magma degassing. In: Oppenheimer, C., Pyle, D.M., and Barclay, J. (eds) Volcanic Degassing. Geological Society, London, Special Publications 213:5-22

Spieler O, Kennedy B, Kueppers U, Dingwell DB, Scheu B, Taddeucci J (2004) The fragmentation threshold of pyroclastic rocks. Earth Planet Sci Lett 226:139-148

Stauffer D, Aharony A. (1994) Introduction to Percolation Theory, 2nd Edition. Taylor & Francis, London, 181 p

Takeuchi S, Nakashima S, Tomiya A (2008) Permeability measurements of natural and experimental volcanic materials with a simple permeameter: Toward and understanding of magmatic degassing processes. J Volcan Geotherm Res 177:329-339.

Takeuchi S, Tomiya A, Shinohara H (2009) Degassing conditions for permeable silicic magmas: implications from decompression experiments with constant rates. Earth Planet Sci Lett 283:101–110. http://dx.doi.org/10.1016/j.epsl.2009

Thovert J.F., Salles J., Adler P.M. (1993) Computerized characterization of the geometry of real porous media: their discretization, analysis and interpretation. J. Microscopy 170:65-79

Tomasi C, Manduchi R (1998) Bilateral filtering for gray and color images. Sixth Internat Conf Comp Vision: 839-846

Wright HMN, Cashman KV, Gottesfeld EH, Roberts JJ (2009) Pore structure of volcanic clasts: Measurements of permeability and electrical conductivity. Earth Planet Sci Lett 280:93-104

Yokoyama T, Takeuchi S (2009) Porosimetry of vesicular volcanic products by a water-expulsion method and the relationship of pore characteristics to permeability. J Geophys Res 114:B0221. doi:10.1029/2008JB005758

Zandomeneghi D, Voltolini M, Mancini L, Brun F, Dreossi D, Polacci M (2010) Quantitative analysis of X-ray microtomography images of geomaterials: Application to volcanic rocks. Geosphere 6:793-804

Zhou J-Q, Chen Y-F, Wang L, Rayani Cardenas M. (2019) Universal relationship between viscous and inertial permeability of geologica porous media. Geophys Res Lett 46:1441-1448.

Ziff RM, Torquato S (2017) Percolation of disorderd jammed sphere packings. J Phys A Math Theor 50: 085001, doi:10.1088/1751-8121/aa5664

Figure Captions

Figure 1 a) Slice of complete sample DRB2012_6e_10. The 256 × 256 pixel region in this slice sampled for analysis is shown by the dashed lines. b) Detailed image of the portion of the 256 × 256 slice sampled from the larger image. c) Thresholded image of (b) with a smaller 160 × 160 pixel region used for quantitative measurements shown enclosed by the solid lines. d) Reconstruction for DRB2012-2a-19, with the one-voxel-wide-skeleton in yellow and the nodes (intersections of the skeleton branches) in red and orange, demonstrating the effect of only considering larger interconnections between bubbles by merging voxels together and taking their average. e) The same reconstruction also considering smaller interconnections based upon the finest voxel resolution. In this work the choice was made to count both large and small interconnections of the skeleton and maximize the number of possible skeleton nodes (or bubble centers~~, in red and orange~~) and pore throats (~~yellow~~the skeleton connecting the nodes) measured. However this procedure can over-count the number of nodes;~~.~~ to~~To~~ reduce the number of over-counted nodes, spheres are centered at each node and isotropically inflated by differing degrees. f) This image demonstrates the effect of less inflation, producing a higher bubble count, and g) demonstrates the effect of more inflation resulting in the merger of more spheres and a smaller number of counted bubbles. The merger is best seen in the small sphere on the left-hand side of the big bubble that is not merged in (f) and would be counted as a separate bubble, but is merged in (g) and becomes part of the large bubble. h) The size of the bubble to be counted is determined by a maximal inscribed sphere that is centered on the center of mass determined from the merged bubbles. Please see text for further discussion. (Color on line~~online~~)

Figure 2 a, b, c) Selected 3D renderings of andesitic experiment DRB2012-2a during vesiculation. In the earliest image the sample is approximately 1 x 1 x 2 mm in size. Due to the perspective projections of these renderings the scale bars are only approximate. Representative interior sections of these samples were chosen for quantitative analysis. d, e, f~~b~~) Corresponding thresholded~~Thresholded~~ tomographic slices (axial slice number 128 near the center of the ~~tomographic~~ reconstruction) from each of the renderings shown in ~~part~~ panels a, b and c, in which black is the melt and white is either the bubbles in the samples or the air around samples (seen in panels e and f~~the early images only~~). The 500 μm scale bar in panel d also applies to panels e and f. Melt viscosities are calculated using Giordano et al. (2008) with 5 wt.% H_2O in the melt at 900 °C and an estimated 1 wt.% H_2O at 994 °C; at 1089 °C, near the end of bubble growth, the melt is assumed to be anhydrous for the viscosity calculation. ~~The numbers in each panel refer to the time in seconds after the start of data acquisition whose q~~Quantitative measurements of the experiment are provided in Table 2 and Supplemental Data Table 1. Please see Supplemental data for a movie of this sample during bubble growth.

Figure 3 a) Bubble size distributions in basaltic sample DRB2012-7. The figure contains subpanels with bubble size distributions from different experiments with porosities from 0.50 to 0.73. All panels in this and subsequent plots of bubble and pore-throat size distributions are plotted in order of increasing experimental duration and temperature. Note that in this figure the sample with a porosity 0.50 was made by reheating the sample with 0.52 porosity (please see Table 2 and the text for further discussion). In each subpanel a volume-normalized histogram of the sizes of the bubbles (the bar graphs) is presented together with the cumulative distribution of the bubble sizes (solid black line). The porosity is given in the upper right corner of each subpanel. The mean bubble diameter, d, and one-standard deviation about the mean is given in~~on the left side of~~ each subpanel. Bin sizes are 5 μm. b) Corresponding pore throat size distributions in basaltic sample DRB2012-7. The information on the pore-throat distributions is presented in the same manner as the bubble size distributions in Part a. Bin sizes are 5 µm.

Figure 4 Bubble and pore-throat distributions for andesitic experiment DRB2012-2a. a) Bubble size distributions for porosities between 0.17 and 0.33. Bin sizes are 5 µm. b) Bubble size distributions for porosities between 0.41 and 0.59. Bin sizes are 5 µm. c) Bubble size distributions for porosities between 0.71 and 0.80. Bin sizes are 5 µm. d) Pore throat size distributions for porosities between 0.17 and 0.33. Bin sizes are 5 µm. e) Pore throat size distributions for porosities between 0.41 and 0.59. Bin sizes are 5 µm. f) Pore throat size distributions for porosities between 0.71 and 0.80. Bin sizes are 5 µm. Please see caption to Figure 3 for a complete description of figure.

Figure 5 Bubble and pore throat distributions for trachyandesitic experiment EFJ-8a. a) Bubble size distributions for porosities between 0.09 and 0.64. Bin sizes are 5 µm. b) Corresponding pore throat distributions. Bin sizes are 5 µm. Please see caption to Figure 3 for a complete description of figure.

Figure 6 Bubble and pore throat distributions for dacitic experiment DRB2012-6e. a) Bubble size distributions for porosities between 0.38 and 0.84. Bin sizes are 5 µm. b) Corresponding pore throat distributions. Bin sizes are 5 µm. Please see caption to Figure 3 for a complete description of figure.

Figure 7 Experimental foam permeabilities determined by lattice-Boltzmann simulations plotted as a function of porosity. Uncertainties in the measured porosity and in the permeability are estimated at 20 relative percent and typically the same size as, or smaller than, the symbols. The solid blue line is the power-law fit to the lattice-Boltzmann permeabilities of the andesitic composition. The proposed relationships between porosity and permeability for basaltic and for silicic compositions from Bai et al. (2010) are also plotted. (Color on line~~online~~) Please see text for further discussion.

Figure 8 Permeability measurements as a function of porosity for aphyric-to-low-crystallinity vesiculated samples foams of basaltic to rhyolitic composition from the literature and this study. Three fits to the data are presented. Fitting all the data with a power law yields the power-law relationship $k_1 = 6.0x10^{-12}\Phi^{4.0}$. A lower bound is constrained by fitting the low porosity, low permeability measurements below 10^{-14} m^2 of Saar and Manga (1999), Lindoo et al. (2016) and Burgisser et al. (2017), which yields- $k_1 = 1.5x10^{-14}\Phi^{1.8}$. An upper bound is defined by the high permeability measurements of Saar and Manga (1999) and of Bai et al. (2010), and is described by a power law of $k_1 = 1.5x10^{-10}\Phi^{4.0}$. Sources of the data are provided in the figure and can be found in the references. (Color on lineonline)

Figure 9 a) Application of the models for the prediction of permeability using the Carman-Kozeny equations of Degruyter et al. (2010) and of Burgisser et al. (2017). The line labeelled 1:1 represents a perfect fit of athe model to the data; the line labeled "*5x*" represents the modeled values multiplied by 5 and the line labeled "*0.2x*" represents the modeled values multiplied by 0.2. In these models the average pore throat value (Table 2) was used as the characteristic diameter of pore throats. b) Modification of the models of Degruyter et al. and of Burgisser et al. by using the maximum pore throat as the characteristic diameter and an empirical value of $\chi = 10$. Note the excellent fit of the Burgisser et al. model to the measurements. c) Comparison of the modified Burgisser et al. model and measured permeabilities of samples from Bai et al. (2010) and of the isotropic samples from Burgisser et al. (2017) using relationships between the average bubble diameter and the largest throat diameter and between the porosity and the tortuosity, as determined in this study. The data from Bai et al. (2010) and from Burgisser et al. (2017) were not used to calibrate the model. Please see text for further discussion. (Color on lineonline)

~~**Figure 10** Gas velocity relative to melt ascent velocity as a function of depth calculated using Equation 17 (following Namiki and Manga 2008) with an initial unvesiculated magmatic velocity of 0.001 m s^{-1}. Calculations were performed for both basaltic magmas (solid black lines) initially with 2 wt. % water and for rhyolitic magmas (dashed red lines) initially with 4 wt% water. Each of the porosity-permeability relationships whose equations are shown in Figure 8 were used in the calculations. Only the high permeability curves cross the v_{gas}/v_{melt} ratio of 1 (indicated by the horizontal dotted line) giving them the potential to lose the gas driving magma ascent at depths between ~ 7500 and 5000 m below the surface for the basaltic system and 13 500 and 9000 m for the rhyolitic system. The porosities at which the high permeability curves cross the critical value of 1 are noted next to the crossing point. Please see text for more discussion. (Color online)~~

Table 1 Starting glass compositions

Table 2 Experimental results

Supplementary Movie Bubble growth in DRB2012-2a

Supplementary Data Table Measured diameters of bubbles and pore throats in the experiments.

Supplementary Figure 1 Connectivity versus porosity in the experimental samples (in color online).

The importance of pore throats in controlling the permeability of magmatic foams

Don R. Baker[1], Francesco Brun[2,3], Lucia Mancini[2], Julie L. Fife[4], Alexandra LaRue[1], Cedrick O'Shaughnessy[1,5], Reghan J. Hill[6], Margherita Polacci[7]

[1]Earth and Planetary Sciences, McGill University, 3450 rue University, Montreal, QC H3A 0E8, Canada don.baker@mcgill.ca

[2]Elettra-Sincrotrone Trieste S.C.p.A., S.S. 14-km 163.5, Basovizza, 34149, Trieste, Italy

[3]Currently: Istituto Nazionale di Fisica Nucleare (INFN) - Sezione di Trieste, Padriciano, 99, 34149 Trieste, Italy

[4]Previously with: Laboratory for Synchrotron Radiation, Swiss Light Source, Paul Scherrer Institut, 5232 Villigen, Switzerland

[5]Currently: Department of Earth Sciences, University of Toronto, 22 Russell St., Toronto, M5S 3B1

[6]Department of Chemical Engineering, McGill University, 3610 rue University, Montreal, QC H3A 0E5, Canada.

[7]School of Earth and Environmental Sciences, University of Manchester, Manchester, U.K.

Corresponding author: don.baker@mcgill.ca
1-514-398-7485

BUVO-S-18-00171
Revised 3 May 2019

Abstract

Foam formation during vesiculation of hydrous magmatic melts at 1 atm was studied *in situ* by synchrotron X-ray tomographic microscopy at the TOMCAT beamline of the Swiss Light Source (Villigen, Switzerland). Four different compositions were studied; basaltic, andesitic, trachyandesitic and dacitic hydrous glasses were synthesized at high pressures as starting materials and then laser heated on the beamline. The porosity, bubble number density, size distributions of bubbles and pore throats, as well as the tortuosity and connectivity of bubbles in the foams, were measured in three dimensions based on tomographic reconstructions of sample volumes. The reconstructed volumes were also used in lattice-Boltzmann simulations to determine viscous permeabilities of the samples. Connectivity of bubbles by pore throats varied from ~100 to 10^5 mm^{-3}, and for each sample correlated positively with porosity and permeability. Although permeability increased with porosity, the relationship is complex; consideration of the results of this and previous studies of the viscous permeabilities of aphyric and crystal-poor magmatic samples demonstrated that at similar porosities the permeability could vary by many orders of magnitude, even in similar composition samples. More than 90 % of these permeabilities are bounded by two empirical power laws, neither of which identifies a percolation threshold.

Comparison of the permeability relationships from this study with previous models (Degruyter et al. 2010; Burgisser et al. 2017) relating porosity, characteristic pore-throat diameters and tortuosity demonstrated good agreement. However, modifying the Burgisser et al. (2017) model by using the maximum measured pore-throat diameter, instead of the average diameter, as the characteristic diameter produced a model that reproduced the lattice-Boltzmann permeabilities to within 1 order of magnitude. Measured correlations between the average bubble diameter and the maximum pore-throat diameter as well as between porosity and tortuosity in our experiments produced relationships that

allow application of the modified Burgisser et al. model to predict permeability based only upon the average bubble diameter and porosity. The experimental results are consistent with previous studies suggesting that increasing bubble growth rates result in decreasing permeability of equivalent porosity foams. The effect of growth rate on permeability is hypothesized to substantially contribute to the multiple orders-of-magnitude variations in the permeabilities of natural magmatic samples at similar porosities.

Keywords: magmatic foam, permeability, bubble and pore throat sizes, bubble connectivity, synchrotron X-ray tomography

Introduction

The competition between magma expansion due to gas exsolution and expansion, and gas loss created by vesiculation in volcanic conduits, exerts a significant control on the explosivity of volcanic eruptions (e.g., Sparks 2003; Spieler et al. 2004, Mueller et al. 2005, 2008). This competition is profoundly influenced by the permeability of the magmatic foam (a mixture of gas-filled bubbles and melt that may contain crystals and if quenched would produce a scoria or a pumice). Relatively impermeable magmas can lead to violent eruptions, whereas permeable ones may not (Sparks 2003; Mueller et al. 2005, 2008). Understanding the development of porosity, Φ, and permeability, k, during magma vesiculation is one of the keys to quantitative modeling of volcanic processes that hold the promise of a better understanding of volcanic eruptions and their precursors (Fagents et al. 2013). Due to the significance of permeability, many studies characterized the porosities and permeabilities of natural samples and experimental run products and demonstrated orders-of-magnitude differences in permeability at similar porosities (e.g., Klug and Cashman 1996; Saar and Manga 1999; Blower 2001; Rust and Cashman 2004; Mueller et al. 2005, 2008; Bouvet de Maisonneuve et al. 2008; Wright et al.

2009; Degruyter et al. 2010; Bai et al. 2010; Polacci et al. 2014; Farquharson et al. 2015; Kushnir et al. 2016; Lindoo et al. 2016; Burgisser et al. 2017).

The structural details of porous media, such as tortousity and the size of the bubbles and pore throats that connect them have long been known to significantly influence permeability (Carman 1937; Archie 1942). Polacci et al. (2008) suggested that “a few large vesicles, exhibiting mostly irregular, tortuous, channel-like textures” in scoria from Stromboli volcano (Italy) were the preferential pathways used for gas escape from the magma. Degruyter et al. (2010) and Burgisser et al. (2017) both demonstrated that the tortuosity of the sample and the characteristic diameter of the pore throats played significant roles in controlling magmatic permeability. These publications demonstrated that the size of the bubbles, the pore throats that connect them, and the ways in which bubbles are interconnected (tortuosity and either in a series or parallel configuration) are significant controls on gas transport in magmatic systems.

Here we report results of a series of high-temperature, *in situ* X-ray tomographic microscopy experiments studying the development of crystal-free, vesiculating samples of silicate melt at 1 atm. Although in the experiments bubbles are formed during heating at constant pressure (rather than during decompression at approximately constant temperature in volcanic systems), the development of the interconnections between bubbles provides important information on the formation of magmatic foams and development of their permeability. Four melt compositions were studied: a mid-ocean ridge basalt (MORB), a trachyandesite, an andesite, and a dacite The viscous permeabilities of the foams were determined by using tomographic reconstructions of sample volumes as the input for lattice-Boltzmann simulations of fluid flow (Hill et al. 2001; Hill and Koch 2002). We concentrated on the viscous permeability k_1, and the applicability of the Carman-Kozeny equation to magmatic foams (Carman 1937). Although we have not investigated the inertial permeabilities, k_2, in our samples, relationships between viscous and inertial permeability have been previously determined (e.g., Rust and Cashman

2004; Yokoyama and Takeuchi 2009; Bai et al. 2010; Polacci et al. 2014; Burgisser et al. 2017). Most recently Zhou et al. (2019) proposed a universal power-law equation relating viscous and inertial permeabilities for all geologic porous media with parameters equivalent to those previously published by Polacci et al. (2014) for volcanic samples. Thus, knowledge of the viscous permeability allows calculation of the inertial permeability using the relationships in Polacci et al. (2014) and Zhou et al. (2019).

Methods

Hydrous glass preparation

Samples of MORB, trachyandesite, andesite, and dacite were chosen for these experiments (Table 1). The MORB is a dredge haul sample graciously donated by C. Langmuir; the trachyandesite is a scoria from the 2010 eruption of Eyjafjallajökull, Iceland, and the andesite and dacite compositions were from Atka Island, Alaska, USA. Each sample was ground to less than 50 μm in diameter and dried at 110 °C before use. Approximately 70 mg of powder plus distilled water were loaded into 3 mm diameter Pt capsules and welded closed in a water bath without volatile loss. Water concentrations are based upon the water added to the capsules and was 3 wt % in successful experiments with MORB, trachyandesite and dacite. The only successful experiment with the andesite contained 5 wt % water. The rock plus water mixtures were melted above their liquidi in a piston-cylinder apparatus at a temperature of 1250 °C or 1200 °C (the trachyandesite only), and a pressure of 1.0 GPa for a duration of 2 h or of 1 h (again only the trachyandesite) in 19.1 mm NaCl-pyrex assemblies (Baker 2004) and quenched isobarically. Subsamples with volumes of approximately ~1 to 2 mm^3 of these crystal-free glasses were used for the synchrotron X-ray tomographic microscopy experiments.

In situ synchrotron X-ray tomographic microscopy

In situ synchrotron X-ray tomographic microscopy was performed at the TOMCAT beamline of the Swiss Light Source at the Paul Scherrer Institut (Villigen, Switzerland) using a laser-based heating system (Fife et al. 2012) and the ultra-fast endstation (Mokso et al. 2010, see Mokso et al. 2017 for current capabilities of the ultra-fast endstation that differ from the description below and allow more rapid acquisition of images than possible when this study was performed). The laser system comprises two, class four diode lasers of 980 nm wavelength on opposite sides of, and 40 mm away from, the sample; these each provide up to 150 W of power to heat the sample. A pyrometer was used to measure the temperature. The ultra-fast endstation incorporated a pco.DIMAX camera, which acquires and transfers data orders of magnitude faster than traditional CCD technology (Mokso et al. 2010). To reach the highest possible temperature, the lasers were pointed just below the sample holder on the zirconia rod that connected the sample holder to the rotation stage below. The temperature was increased until it reached approximately 600 °C at which point the sample was lowered into the laser beams. Samples were then heated at either 1 °C s^{-1} or 6 °C s^{-1} to the maximum temperature of the experiment, resulting in sample vesiculation and creation of a silicate foam under open-system conditions such that the sample was free to expand and exsolved gas escaped the system. Initially a programmed heating rate of ~6 °C s^{-1} was chosen as the best compromise between instantaneous heating of the sample and the need for bubbles to grow slowly enough to be successfully imaged. Due to many experimental failures, a slower programmed heating rate of ~ 1 °C s^{-1} was found to produce more successful experiments (Table 2). Measurement of the time-temperature histories of the experiments demonstrated that the heating rates were often ~ 20 percent slower than the programmed ones (Table 2).

Data acquisition was initiated at the first visible onset of vesiculation, such as bubble formation and sample expansion. During data acquisition, samples reached a maximum temperature between ~950 °C and ~1200 °C. Polychromatic X-rays were filtered to 5 % power, generating 3 ms exposure times, and 701 projections were captured over an angular range of 180 degrees during continuous rotation. The microscope used for these scans incorporated a specially designed, high numerical aperture objective lens with four-fold magnification. This corresponded to a 2.89 μm × 2.89 μm pixel size and a 5.83 mm × 5.83 mm field of view. The optics were coupled to a LuAG:Ce 100 μm thick scintillator screen. Reconstructions were performed using a modified GRIDREC algorithm (Dowd et al. 1999; Rivers and Wang 2006; Marone and Stampanoni 2012) coupled with Parzen filtering of the sinograms.

Many bubble-growth experiments were performed, but only a few were successful. The most significant problem was image blurring due to sample motion caused by rapid vesiculation and bubble growth that rendered the tomographic reconstructions useless for this study. Other problems were samples that failed to heat to temperatures high enough to vesiculate (which included all rhyolitic samples investigated) and samples that cracked into small pieces during heating.

Of the 62 experiments performed, only one dynamic experiment on the andesitic composition, one on the trachyandesitic composition, and one on the dacitic composition yielded 3D reconstructions that could be used to extract quantitative data. Bubble growth in all dynamic experiments on the MORB composition was so rapid and the motion artifacts so severe that no successful reconstructions were made. However, the final steps of 4 experiments on the MORB composition were successfully imaged as bubble growth slowed or stopped due to gas loss from the sample. These experiments span much of the range of porosities measured in the successful tomographic scans on the andesite, trachyandesite, and dacite, and allow comparison between the four different melt compositions. Even the successful experiments contained some image artefacts due to sample movement during bubble growth. These aretefacts were avoided during the sample analysis discussed below.

Image analysis and quantification

The bubble distributions in the samples were not homogeneous because of thermal gradients in the laser furnace. Thus, only representative central portions of the samples, far from their edges and the capsule walls, were analyzed, and the measurements reported are not representative of the entire sample, but only of the volume investigated. The tomographic reconstructions were inspected with ImageJ and subvolumes from the most vesicular portions of the samples were chosen; in most cases they were 256 × 256 × 256 voxels in volume (Fig. 1a-c). Because these volumes were too large for lattice-Boltzmann determination of their permeability (discussed below) representative subvolumes of 370 × 370 × 370 μm^3 (128 × 128 × 128 voxels, trachyandesite EFJ-8a), or 462 × 462 × 462 μm^3 (160 × 160 × 160 voxels, andesite DRB2012-2a, dacite DRB2012-6e-8, -9, -10, MORB DRB2012-7a-2, -3, -cf) or 578 × 578 × 578 μm^3 (200 × 200 × 200 voxels, dacite DRB2012-6e-07, MORB DRB2012-7f-10) were used for all quantitative analyses with the *Pore3D* software library (Brun et al. 2010; Zandomeneghi et al. 2010). An edge-preserving smoothing filter (Tomasi and Manduchi 1998) was applied followed by a 3D, manually selected, global fixed threshold to separate pore space from glass. This segmentation process was adopted for all datasets.

The vesicularity was computed as the number of voxels belonging to the pore space with respect to the total number of voxels in the object. Objects, bubbles and pore throats, were not counted unless their size was greater than two voxels, where each voxel was 2.89 × 2.89 × 2.89 μm^3 in volume. Baker et al.'s (2011) study of the reproducibility of porosity measurements using X-ray microtomography demonstrated that the precision of vesicularity measurements is approximately 0.01. We expect similar uncertainties for pore throats because the same techniques were used for measurements of vesicles and pore throats. The interconnected porosity was determined from the same images using the

ObjectCounter3D plugin in ImageJ (https://imagej.net/3D_Objects_Counter).

A family of descriptors based on skeleton analysis (Lindquist and Lee 1996) was applied to derive bubble number and pore throat number density as well as bubble- and pore throat-size distributions. As in our previous research (Baker et al. 2012), the skeletonization algorithm of Brun and Dreossi (2010) was applied. Each bubble diameter and the minimum thickness of each pore throat was computed using the concept of a maximal inscribed sphere, which was moved through the pore throat along the skeleton to find its minimum diameter (Hildebrand and Rüegsegger 1997). The skeletonization algorithm used in this study offers a tuning parameter to control the amount of branches in the output skeleton. Figures 1d & e present the differences between a case where only the most significant (and larger) interconnects are considered and a case where the smallest interconnects are considered and a skeleton branch is added to the skeleton network for each of them. This parameter is tuned to select the maximum number of branches in this study.

The geometrical determination of bubbles and throats is difficult because there is no unambiguous geometrical definition of where a bubble ends and a connecting channel begins. Conceptually, the skeleton nodes correspond to bubbles, and the branches of the pore-space skeleton correspond to the channels (or paths) connecting the bubbles. However, a typical pore/node correction has to be applied because several skeleton nodes may occur in the same bubble body (Lindquist 2002), as can be seen in Figures 1d and 1e. In this work, a criterion based on the isotropic inflation of spheres centered on each node was used. If two or more spheres overlap, they are considered part of the same bubble. The number of identified bubbles is actually the number of independent clusters of overlapping inflated bubbles. The amount of inflation can be controlled and acts as a parameter for the merging criterion. The steps in this process are graphically shown in the example presented in Figures 1d-1h. An insufficient inflation value overestimates the number of pores, while the maximum inflation to fill the entire bubble might underestimate this value if several spurious branches result after skeletonization. In this work a level of inflation equal to 85% of the maximum was used. Variations around this value were also considered, and it was found that this parameter only weakly affects the computed values of the bubble and pore throat numbers and sizes, as seen in Figures 1f & g that present two examples with different levels of inflation.

Some concerns still remain for the throat size determinations; while very short branches are usually disregarded, because some maximal spheres centered at the skeleton nodes may completely enclose the short branches, incorrect channels may still be considered. Practically, this means that the throat-size distribution may present some large-valued outliers due to the consideration of branches that may not represent physical channels.

The final assessment of bubble size is based on the diameter of the maximal inscribed sphere placed at the center of mass of the cluster of the overlapping inflated bubbles (Fig. 1h). The bubble number density was calculated by dividing the number of inscribed spheres (bubbles) identified after skeletonization by the investigated volume. The uncertainties in the numbers of bubbles and of pore throats can be estimated as the square root of the number of each object type counted by application of Poisson statistics.

The connectivity, β, is a standard topological property that measures the number of interconnections (in this study pore throats) between objects (in this case bubbles). Connectivity analysis of tomographic reconstructions was pioneered in studies of bone structure (Odgaard and Dundersen 1993) and of porous media (Thovert et al. 1993). Following these two publications we calculate the connectivity per unit volume (mm^3 in this study), β or connective density, as done by Odgaard and Gundersen (1993) using:

$$\beta = \frac{\text{\# pore throats} - \text{\# bubbles} + 1}{\text{sample volume}}. \quad (1)$$

This topological measure may yield both negative and positive values per unit volume. As an illustration, consider a simplified example of 4 bubbles in a volume of 0.5 mm^3. In the case of no interconnections, or pore throats, between the bubbles, the value of β is -6 mm^{-3}. In cases where only single connections are allowed between bubbles (i.e., two pore throats cannot connect the same two bubbles), a system with two interconnections yields a β value of -2 mm^{-3}, if there are three interconnections β = 0 mm^{-3}, and if there are four β = 2 mm^{-3}. Thus, a β value of 0 mm^{-3} is the minimum threshold at which the pore throats interconnect the bubbles in this example. This threshold value can exceed 0 if we relax the constraint that bubbles can only be connected by a single pore throat or that all pore throats must interconnect bubbles within the volume of interest. Following basic statistical rules, the uncertainties in the values of β are calculated from the uncertainty in the number of bubbles, δ bubbles, and the uncertainty in the number of pore throats, δ pore throats, and the sample volume by

$$\delta\beta = \frac{\sqrt{(\delta \text{bubbles})^2 + (\delta \text{pore throats})^2}}{\text{sample volume}}. \quad (2)$$

Tortuosity in this research is defined as the average distance a particle would travel between two opposite sides of the sample by the pore network divided by the Euclidean distance between the opposite sides. The MATLAB® code TORT3D (Al-Raoush and Madhoun 2017) was used for all tortuosity measurements. The tortuosity was determined in three orthogonal directions and then averaged; the average values are reported in Table 2.

The 3D visualization of reconstructed and analyzed volumes was obtained by the commercial software VGStudio Max 2.0 (Volume Graphics).

Lattice-Boltzmann modeling of permeabilities

Because of the dynamic nature of the experiments and the collapse of the samples with loss of vesicularity near to, or at, their termination, sample permeabilities could not be measured directly. Instead, lattice-Boltzmann modeling of permeabilities was performed using a modified version of an established lattice-Boltzmann code (Hill et al. 2001; Hill and Koch 2002). Details of the permeability modeling applied to tomographic reconstructions can be found in Bai et al. (2010), in which the accuracy of the viscous permeabilities calculated by modeling was directly compared against measured permeabilities and shown to typically be within a factor of 11 for porosities from 0.05 to 0.87.

Bai et al. (2010) demonstrated that the ratio of the tomographic reconstruction resolution (voxel edge length) to the lattice size (edge length of subvolume) and the simulation size could influence the calculated permeability. The resolution-to-lattice-size ratios used in this study are in the range where Bai et al. (2010) demonstrated that the value of the ratio had no effect on the calculated permeability. Bai et al. (2010) found that decreasing the lattice size below 762 μm increased the calculated permeability by a factor of less than 20. Analysis of Bai et al.'s (2010) results indicates that using the smallest lattice size in this study (370 μm) may, at most, overestimate the permeability by a factor of ~ 3 for low porosity samples. The other, larger, simulations used in this study are expected to have uncertainties less than 20 % (Bai et al. 2010).

Permeabilities in the three orthogonal directions of each subvolume were calculated. Because the maximum difference between the lattice-Boltzmann permeabilities measured in three orthogonal directions of the samples was less than a factor of 2, we concluded that there was no significant variation in the permeability as a function of direction and report the average permeability values for each sample in Table 2. This lack of orientation effects supports the modeling of our samples as random networks of bubbles interconnected by pore throats.

Bubble growth during isobaric heating versus isothermal decompression

Experiments in this study were performed by isobaric heating at atmospheric pressure because a high-pressure furnace was not available on the TOMCAT beamline. The resulting time-temperature-pressure path in these experiments is distinctly different from bubble formation during near-isothermal decompression in natural systems and in many experiments (e.g., Burgisser and Gardner 2004; Lindoo et al 2016, 2017; Mueller et al. 2005; Spieler et al. 2004; Takeuchi et al. 2009).

Although bubble nucleation and growth during isothermal decompression and isobaric heating experiments are both driven by supersaturation of the melt with a volatile, the viscosity of the melt increases during isothermal decompression (due to water loss to the bubbles) and may either increase (due to water loss) or decrease (due to increasing temperature) during isobaric heating. For example, in these experiments the andesitic melt begins vesiculation at 900 °C with a water concentration of 5 wt% and a viscosity of ~ 750 Pa s (calculated following Giordano et al. 2008). If this melt lost all its water by the end of the experiment at 1100 °C, the viscosity would be ~ 6700 Pa s. Although it is difficult to estimate the water concentration in the melt during vesiculation, we estimate that approximately 1 wt% water remains in the melt at ~ 1000 °C, which would yield a melt viscosity ~ 3100 Pa s. During these experiments the diffusivity of water in the melt also is controlled by a combination of heating and dehydration. Using the equations of Ni and Zhang (2018), the water diffusivity at the start of vesiculation is expected to be ~ 3×10^{-13} m^2 s^{-1}, decreasing to ~ 1×10^{-14} m^2 s^{-1} when water is lost. On the contrary, for isothermal decompression at 1100 °C of the same melt composition, the viscosity would increase from 32 Pa s at the start of vesiculation to ~ 6700 Pa s if all of the water is exsolved from the melt, and the water diffusivity would decrease from ~ 3×10^{-12} m^2 s^{-1} to ~ 1×10^{-14} m^2 s^{-1}.

These differences in the history of the melt viscosity and diffusivity will influence the rates of bubble growth and coalescence of neighboring bubbles. Following Navon and Lyakhovsky (1998) the radius of an individual bubble during its initial stages of growth will be significantly affected by the melt viscosity:

$$r \propto exp\left[\frac{\Delta P}{4\eta} t\right], \quad (3)$$

where r is the bubble radius, ΔP is the supersaturation pressure, η is the melt viscosity, and t is the time. As the bubble grows and supersaturation decreases, the bubble radius is described by a law containing the square root of the product of the volatile diffusivity in the melt and time (Equation 36 of Navon and Lyakhovsky 1998). Melt viscosity also exerts control on the time necessary for interacting bubble walls to fail and coalescence to begin, τ_{df}:

$$\tau_{df} = \frac{3\eta r^2}{4\Delta P h_{min}^2}, \quad (4)$$

where h_{min} is the critical thickness at which the walls fail (Navon and Lyakhovsky 1998). Equations 3 and 4 demonstrate that the rates of bubble growth and coalescence during the early stages of isobaric heating experiments should be slower than those in isothermal decompression experiments because of the higher viscosities and lower water diffusivities in the melt early in the isobaric heating experiments. However, as both types of experiments reach the end of bubble growth and water loss, the rates at which bubble growth and coalescence occur should converge.

Both isothermal decompression and isobaric heating experiments are expected to produce similar, random bubble, or foam, structures, due to the stochasticity in both the location and timing of bubble nucleation in the melts. Because of the higher viscosities and lower diffusivities of isobaric heating experiments, the vesicularity and interconnectivity of bubbles (due to coalescence) may be expected to be smaller than in isothermal decompression experiments of similar, short durations (Equations 3 and 4). Because of these differences between isothermal decompression and isobaric heating experiments we did not study bubble growth and coalescence rates, but instead concentrated on the development of porosity and permeability of the foams, while fully recognizing that the values we determined may be minimal ones.

Despite the differences between isothermal decompression and isobaric heating experiments, we can make a comparison between the rates of magma ascent and the rates of degassing during isobaric heating experiments by dividing the melt supersaturation pressure (Table 2) by the duration of the isobaric heating (Table 2) to yield equivalent decompression rates of approximately 0.1 to 2 MPa s^{-1}. Although these equivalent decompression rates are only rough approximations, the low values are similar to decompression rates found by Ferguson et al. (2016) for eruptive products of Kilauea volcano and the high values to decompression rates found by Humphreys et al. (2008) for the May 18, 1980 plinian eruption of Mt. St. Helens.

Results

Visual observations

Bubble growth in the samples occurred rapidly at temperatures above 600 °C. Typical bubble nucleation and growth can be seen in Figure 2 and Supplemental Movie 1 of andesitic sample DRB2012-2a, which was heated from 600 °C to 1100 °C over a period of 100 s (Table 2).

In the absence of nucleation delay, bubble growth is presumed to occur once the sample temperature exceeds that of the glass transition. The onset of the glass transition temperatures for the samples studied can be estimated using the results of Giordano et al. (2005). The glass transition given in Giordano et al. (2005) for basaltic, trachytic and dacitic compositions determined at their most rapid heating rate of 0.333 K s^{-1} and water concentrations up to 2.5 wt.% were fit by a power-law, which was chosen because power-laws describe the effect of water addition on melt viscosity (e.g., Shaw 1972). The power-law fit reproduces the calibrating data to within a maximum of ~ 50 K, as well as reproducing the anhydrous andesite glass transition temperature of Neuville et al. (1993) that was not used in the calibration. We estimate a minimum onset of the glass transition in our samples with 3 wt% water (MORB, trachyandesite, and dacite) at 460 °C and in the andesite with 5 wt% water at 440 °C. However our heating rates were approximately 3 to 15 times more rapid than used in Giordano et al.'s experiments, thus the observed vesiculation temperatures were significantly above these minimum glass transition temperatures, in the range of 616 to 900 °C (Table 2). Although these delays may be attributable to a short nucleation delay, we interpret them as being due to our inability to observe the onset of bubble growth in real time during the experiments because of the small size of the initial bubbles. This inability to see the earliest bubbles made it difficult to measure samples at low porosities and only a few data at these conditions were obtained (Table 2).

Bubble growth was initially observed as a dense cloud of small bubbles that grew into larger, easily discernible, bubbles that rapidly became interconnected (Fig. 2). Typically, these early growth rates were so rapid that they were blurred in the tomographic images, so meaningful quantitative measurements could not be made.

Visual inspection of the tomographic reconstructions revealed that early bubbles vary from ellipsoidal to sub-spherical, but within seconds all evolve into sub-spherical to spherical shapes. Bubble growth in all experiments on the basaltic composition was too rapid to quantitatively analyze those samples before termination of the experiment. However, in four cases we extracted limited data from the different stages of foam development (Table 2). Bubbles coalesced and typically grew to a maximum size, creating a foam with thin-walled bubbles. If the sample was not immediately quenched, the foam contracted and underwent partial collapse, and in some cases collapse occurred before the termination of the experiment. This behavior is attributed to the loss of volatiles, either through failure of the bubble walls or diffusion through them.

Not every tomographic reconstruction set could be used for all the quantitative analyses presented in the Methods section. In some cases, permeabilities could not be determined (e.g., DRB2012-6e-07) because of the large computer memory required to resolve the surface area of the interconnected bubbles.

Bubble number density (BND), bubble size distribution (BSD), and pore throat size distribution (PTD)

Table 2 presents a summary of our quantitative measurements, and the sizes of all bubbles and pore throats measured in the studied samples are provided as supplementary material (Table S1). All measurements reported in this study were made on volumes far from the edges of the samples and that displayed no visual evidence of anisotropy. The typical distance of the analyzed volume from the sample edges was approximately 500 μm. Because of the small sample volume, in some cases the number of bubbles and pore throats, as well as their range in size, are small (Table S1). In all but one case for the dacitic composition, DRB2012-6e-10, the largest bubble in the investigated volume was less than 6 % of the sample volume. In DRB32012-6e-10 the largest bubble was 31% of the volume.

In general, in each sample the bubble number densities tend to increase with porosity up to a maximum and decrease at higher porosity (Figs. 3-6, Table 2), although between any two steps the BND can decrease (Table 2). Increasing BNDs are attributed to continuous nucleation and decreasing BNDs to bubble coalescence.

The measured bubble size and pore throat size distributions of the experiments are presented in Figures 3-6. Each figure presents a volume-normalized histogram of the sizes of either the bubbles or the pore throats. None of the distributions are Gaussian, but instead often display "long tails" to large bubble and throat sizes, a characteristic indicative of power-law distributions (Newman 2005). Although the bubble-size and throat-size distributions can be fit with power-laws, this was not done in this study due to the small size range in each distribution that results in large uncertainties in the calculated power-law exponent. Despite evidence that the sizes are power-law distributed, and therefore their means and standard deviations do not have the same significance as in Gaussian distributions (Newman 2005), each panel of each figure provides the mean diameter and the standard deviation of either the bubble diameter or pore throat diameter to allow comparison of the measurements with previous studies (e.g., Burgisser et al. 2017). The relative standard deviations about the mean bubble sizes and pore throats are in most samples greater than 25% and often near 50%. These large standard deviations are consistent with the non-Gaussian distributions of bubble and pore throat sizes (Newman 2005).

Bubbles measured in the basaltic composition reach a size of approximately 460 µm in diameter, and the BNDs are in the thousands per cubic millimeter (Fig. 3a, Table 2). The two samples with the lowest porosities (0.52 and 0.50) are from the same experiment and demonstrate that with time the number of small bubbles in the 5 to 10 µm range increases, which indicates continuing bubble nucleation and growth, as does that of larger bubbles in the 40 to 70 µm range, which provides evidence of continued growth. The disappearance of bubbles in the size range of 55 to 60 µm of the second sample ($\Phi = 0.50$) is interpreted as a consequence of bubble coalescence, and its lower porosity is probably due to bubble collapse that occurred between these two heating experiments (Table 2). Comparison of the average bubble size in each experiment does not indicate any significant trend with porosity (Fig. 3a).

The number of pore throats in the basalt varies from about 6.40×10^3 mm^{-3} at the lowest porosity to approximately 7.22×10^4 mm^{-3} at the highest porosity. The two low-porosity (0.50 and 0.52) measurements of pore throats experiment demonstrate only moderate increases in the number and size of pore throats (Fig. 3b, Table 2). The experiment with 0.55 porosity contains one pore throat that is anomalously larger then the next largest one (Fig. 3b), and our experimental techniques for measuring the pore diameter may produce large-valued outliers in the pore throat size distributions. Whereas we cannot completely discard the possibility that the largest pore throat in this sample is an artefact, we think that size difference between the largest pore throat and the others in the distribution (Fig. 3b) is not sufficiently large to discard the measurement. Because the basaltic results for the two highest porosity measurements (0.55 and 0.73) are from different experiments, it is difficult to investigate the evolution of BSD and PTD with increasing porosity. Nevertheless, if these two samples are interpreted as an evolutionary trend, there appears to be an increasing number of pore throats with increasing porosity (Fig 3b, Table 2).

In contrast to the basaltic experiments, all of the andesite data (Fig. 4a, b, c, Table 2) were collected from the same experiment; however the location of the sample volume quantified varied slightly between different time steps in order to choose the most representative volumes near the center of the samples and to avoid volumes containing motion artefacts and/or anomalously large or small bubbles. The maximum bubble size was between 215 and 220 μm (Fig. 4c). All andesite BSDs are dominated by bubbles in the 5 to 20 μm size range (Fig. 4a, b, c). The large number of small bubbles in all but the final porosity is interpreted to reflect a process of continuing nucleation and growth of new bubbles. The appearance of larger bubbles, greater than 40 μm, at porosities above 0.41 is caused by the expansion of gas within them during heating, and by coalescence. Evidence of coalescence is seen in the decreasing number of intermediate-sized bubbles with the appearance of larger bubbles in the highest porosity samples (cf., Gaonac'h et al. 1996). The PTD distributions demonstrate the growth of throat sizes and number with increasing porosity (Figs. 4d, e, f). The largest pore throat size grows from 10-15 μm to a maximum of 50-55 μm. In comparison to the basalt, there are fewer pore throats greater than 30 μm.

The BSDs for the trachyandesite at the two highest porosities display broad peaks in the distribution without long tails to large bubble sizes seen in some of the andesite and basalt BSDs (Fig. 5a, Table 2). The lowest porosity sample had only a single bubble and no pore throats in a volume of 0.0506 mm^3 (Fig. 5a, b, Table 2). The maximum bubble measured was in the 95 to 100 μm size class. Although no bubbles less than 10 μm were observed at a porosity of 0.61, one appears at $\Phi = 0.64$, suggesting continuing bubble nucleation. Bubble coalescence between the same two porosities is indicated by the decreasing number of bubbles with sizes between 10 and 75 μm and increasing numbers of larger-sized bubbles in the same sized volume (Fig. 5a). The PTDs of the trachyandesite show a growth in the density of pore throats between 0.30 and 0.61 porosity followed by a decline in densities between 0.61 and 0.64 porosity with an increase in the number of larger pore throats (Fig. 5b.).

The dacite BSDs demonstrate the growth of larger bubbles with increasing porosity, up to a maximum of almost 400 μm at $\Phi = 0.84$ (Fig. 6a). Bubbles in the size range of 10 – 15 μm increase in number between porosities of 0.38 and 0.79, and subsequently decrease as larger bubbles appear at higher porosities, a behavior we attribute to coalescence (cf., Gaonac'h et al. 1996). The PTDs of the dacitic sample demonstrate growth of larger pore throats up to a porosity of 0.87 followed by a decrease in porosity at the end of the experiment to 0.84 (Fig 6b). Although the largest pore throats reach 70 μm, the distributions are dominated by smaller pore throats. The loss of the large pore throats seen in the distribution for $\Phi = 0.84$ is associated with the growth of the large bubbles in this sample (Fig. 6a), which are presumed to have incorporated the larger pore throats into them during growth.

Connectivity, coordination number, and tortuosity

In all cases, the connected porosity is similar to the total porosity (Table 2); however the connectivity, β (Eqn. 1), varies significantly (Table 2, Supplementary Fig. 1). The β values in each type of foam increase from hundreds to thousands per cubic millimeter with increasing porosity (Table 2) up to maximums in the tens to hundreds of thousands per cubic millimeter and then, with the exception of the basaltic composition, decrease at higher porosities (Table 2). This trend is similar to those observed for the BNDs and the PTDs (Table 2, Figs. 3-6).

The average coordination number (or number of interconnected bubbles surrounding a specified bubble) for each porosity (Table 2) of an individual melt composition is similar and varies between ~ 4 and 6, with a few outliers reaching values near 7 (DRB2012-7c-f, DRB2012-2a-18, DRB2012-6e-10) and one almost reaching 8 (DRB2012-2a-19). These average values are far below the maximum value of equal-volume, deformable bubbles surrounding a central bubble (the kissing number) of 32 (Cox and Graner 2004). However, the standard deviations about the average for each sample are often as large as, or even larger than, the mean, and the maximum coordination numbers are often near 100 and can reach almost 600 (Table 2). The bubbles with such high coordination numbers are large and surrounded by a network of small bubbles. (A two-dimensional image of such a bubble can be seen in Fig. 1.) Such high values of the kissing number are not inconsistent with simulations of polydisperse foams that display average coordination numbers between 11 and 14, but contain some foam polyhedra with coordinations approaching 100 (Kraynik et al. 2004).

The tortuosity, τ, of the foams varies from a low of 1.09 (dacites DRB2012-06e-8 and DRB2012-6e-9) to a high of 1.72 (andesite DRB2012-2a-9); however, most tortuosity values fall between 1.1 and 1.3 (Table 2). The relationship between increasing porosity and decreasing tortuosity in the studied samples can be described by (cf., Wright et al. 2009, Degruyter et al. 2010):

$$\tau = (1.0487 \pm 1.0201)(\Phi)^{-0.3192 \pm 0.0252}, \tag{5a}$$

and a correlation between increasing connectivity and decreasing tortuosity was also found:

$$\tau=(2.4376 \pm 1.1044)(\beta)^{-0.0687\pm0.0102}. \quad (5b)$$

Although the uncertainties in the fitting parameters are large, these equations provide useful relationships between these different measures of foam properties, as will be shown below.

Permeability

The lattice-Boltzmann (LB), viscous permeabilities, k_1, of the samples vary from 3 x 10^{-15} to greater than 5 x 10^{-11} m^2 (Table 2, Fig. 7). Note that simulations for one sample, DRB2012-6e-7 failed due to its extraordinarily fine structure, so its permeability could not be determined (discussed above). Another sample, EFJ08a-06, had only one bubble and its permeability also could not be determined.

The data sets in Figure 7 were fit with a power law because both the Carman-Kozeny relation (Carman 1937) and percolation theory (Stauffer and Aharony, 1994) predict a power-law relationship between porosity and permeability. Formally, the percolation theory relationship is expected to be $k_1 \sim (\Phi - \Phi_c)^{\mu}$, where, k_1 is the viscous permeability, Φ_c is the critical porosity threshold where the sample becomes permeable, and μ is an exponent that depends upon the system dimensionality (Stauffer and Aharony, 1994). The critical porosity threshold for monodisperse spheres in three dimensions is ~ 0.29 (Domb 1972; Lorenz and Ziff 2001); however, as discussed in detail below, the critical porosity threshold is a function of the size distribution and shape of the vesicles. Permeability thresholds in natural and experimental magmatic foams can vary from below ~0.03 (e.g., Saar and Manga 1999; Bai et al. 2010) to values in excess of 0.63 (Takeuchi et al. 2008, 2009; Lindoo et al. 2016). The critical porosity threshold for any given sample is unknown, and the porosity-permeability relationships in some magmatic foams have been empirically fit with a power law of the form $k_1=A\Phi^B$, where A and

B are fitting constants (e.g., Klug and Cashman 1996; Bai et al. 2010), although in some other studies the estimated critical porosity threshold (typically 0.3) has been included in permeability-porosity relationships (e.g., Saar and Manga 1999; Blower 2001; Rust and Cashman 2004, 2011).

Our most complete data set on the andesitic composition foam displays a power-law relationship between porosity, Φ, and LB permeability of $k_1 = 1.68x10^{-11}\Phi^5$ (Fig. 8). Assuming a critical porosity of 0.010 below the minimum porosity at which a LB permeability was determined, or 0.15, produces a percolation theory power law fit of $k_1 = 5.79x10^{-12}(\Phi - \Phi_c)^{2.1}$. At porosities up to ~ 0.60, the measurements are similar to the Bai et al. (2010) fit to permeabilities of silicic rocks measured by Klug and Cashman (1996). The LB permeabilities of andesitic foams at porosities greater than ~ 0.60 diverge from Bai et al.'s (2010) fit to silicic foams leading to an order of magnitude difference between the two at a porosity of 0.90 (Fig. 7).

The LB permeabilities of two basaltic foams at ~0.50 porosity bracket the fit to the andesitic foam but the LB permeability increases to a value that is an order of magnitude greater at a porosity of ~0.55. The permeability values at ~ 0.50 porosity (DRB2012-07a-3) may be artificially low because of bubble bursting that was observed at the end of previous experiment (DRB2012-07a-2), and some of the porosity and pore throats may have been lost. These measurements at 0.50 and 0.55 porosity were made on two different chips of basaltic melt; this complicates the interpretation because the two samples have slightly different time-temperature histories, which together with the bubble popping in the sample at 0.50 porosity may might create differences in foam porosity and permeability. Thus, we doubt that the factor of ten increase in permeability between ~ 0.50 and 0.55 porosity for these basaltic samples is significant. The LB permeabilities at 0.55 and 0.73 porosity are similar to those found by Bai et al. (2010) on a high-K composition basaltic foam from Stromboli, as shown by the fit to their data in Figure 7.

The trachyandesitic foam displays a unique behavior. At low porosities, near 0.30, its LB permeability is significantly above that of the andesitic experiment, but at higher porosities the LB permeability falls to values similar to the andesitic composition (Fig. 7).

The LB permeability of the dacitic composition at 0.79 porosity cannot be distinguished from that of the similarly porous andesitic experiment, but the two higher porosity dacitic foams display significantly higher LB permeabilities than expected from the trend described by the lower porosity dacitic and andesitic experiments (Fig. 7).

The experimental results demonstrate that both average bubble sizes and pore throat sizes increase with increasing vesicularity; however, the increase in pore throat sizes is less than that of the bubbles (Figs. 3-6). The maximum bubble sizes are observed in the dacitic composition, reaching nearly 400 μm in diameter, whereas the maximum bubble sizes for the basaltic, andesitic, and trachyandesitic compositions are 180, 220, and 100 μm, respectively. The maximum throat diameters are near 100 μm in the basaltic foam, but only 55 μm in the andesitic foam, 35 μm in the trachyandesitic foam, and 65 in the dacitic foam. Increasing vesicularity increases connectivity and decreases tortuosity. All of these changes in foam structure result in higher permeabilities that are not simply related to the melt compositions investigated.

Discussion

Permeability is not a simple function of porosity

Porosity is often considered the primary control of permeability; in most cases increasing porosity results in higher permeabilities (e.g., Fig. 7), but it has long been understood that other variables such as bubble sizes, composition, connectivity, pore throat diameter, tortuosity etc. significantly influence permeability (e.g., Carman 1937; Archie 1942; Rust and Cashman 2004; Mueller et al. 2005; Bai et al. 2010; Degruyter et al. 2010; Polacci et al. 2012, 2014; Lindoo et al. 2016; Burgisser et al. 2017; Colombier et al. 2017).

An obvious and significant difference in the physical properties of the studied melt compositions is their viscosity (Table 1). However, a simple correlation between melt viscosity and permeability at a specific porosity does not exist. The experimental results using crystal-free samples demonstrate that at ~ 0.5 porosity basalts can have LB permeabilities similar to andesites, and at porosities approaching 0.9 the lattice-Boltzmann permeabilities of basalts and dacites are similar (Fig. 7) despite these melts displaying orders-of-magnitude differences in their viscosities (Table 1). Comparison of melt viscosities with the average pore-throat diameters (Figs. 3-6) does not provide clear evidence of a positive correlation between these two properties either (cf., Polacci et al. 2014).

Our study provides no evidence that composition alone controls the permeability-porosity relationship. Connectivity also does not provide a simple predictor of permeability, as evidenced by an order of magnitude difference in the lattice-Boltzmann permeability of samples with similar connectivity and porosity (Table 2, Fig. 7, Supplementary Figure 1). Tortuosity also does not appear to directly correlate with the porosity-permeability relations of the samples studied (Table 2). However, the bubble- and pore throat-size distributions (Figs. 3 – 6) suggest that larger bubbles and larger pore throats play a significant role in influencing the permeabilities of magmatic foams. Before quantitatively investigating the role of bubble- and pore throat sizes in controlling the permeability of magmatic foams, we compare our results with those from previous studies.

Porosity-permeability trends compared to previous determinations

Our lattice-Boltzmann permeability determinations are compared with previous measurements of porosity and permeability from aphyric to low-crystallinity natural and experimental samples in Figure 8. These data were taken from published studies to illustrate the distribution of measured permeabilities and porosities. The lattice-Boltzmann permeability determinations of the experiments in this study are consistent with previous measurements of similar composition samples (Fig. 8), even though in some cases our experimental samples are orders of magnitude smaller than natural samples. At any given porosity the combined data set demonstrates that permeability can vary by orders of magnitude; nevertheless, the data define significant trends as porosity increases from negligible values to near 1.0 (Fig. 8).

Most viscous permeabilities increase from ~10^{-17} m^2 at porosities near 0.01 to ~10^{-13} m^2 at 0.20 to 0.30 porosity, although some rhyolites at these porosities have permeabilities of only 10^{-15} m^2 (Fig. 8). At porosities above ~0.3, the sphere percolation threshold (Lorenz and Ziff 2001), the permeabilities continue to increase but at a slower rate than observed at lower porosities (Fig. 8). For porosities between 0.5 and 0.9, the permeabilities in Figure 8 range from values as low as ~ 10^{-14} m^2 (Lindoo et al. 2016) to as high as 10^{-10} m^2 (Bai et al. 2010). The slow increase in permeability at porosities above 0.3 suggests that once a permeable pathway is created, the addition of other pathways for gas transport at higher porosities (as shown by higher values of β and lower values of tortuosity) increases the permeability much less significantly than the first pathway. Most lattice-Boltzmann permeabilities measured in this study are near the center of the trend in Figure 8, with the exceptions of the highest permeability basaltic and dacitic melts.

In general, silicic foams have lower permeabilities and mafic foams higher permeabilities, but the dacitic foams with greater than 0.80 porosity measured in this study have lattice-Boltzmann permeabilities similar to basaltic foams with similar porosities (Saar and Manga 1999; Bai et al. 2010).

Rust and Cashman's (2004) permeabilities of rhyolite, pumice and obsidian as well as Farquharson et al.'s (2015) permeabilities of pumiceous andesite demonstrate almost a two order-of-magnitude variation at similar porosities (Fig. 8). Thus the influence of composition on any porosity permeability relationship appears to be weak.

The porosity-permeability data set contains many determinations at porosities below the nominal critical value for mono-disperse spheres. Each specific sample may have its own critical porosity based upon the size distribution and shape of the bubbles and pore throats. Because of our lack of knowledge of the critical porosity for each sample, the data were fit by empirical power laws without including a critical porosity. Although the data in Figure 8 can be empirically fit with a single power law, $k_1 = 6.0x10^{-12}\Phi^{4.0}$, the dispersion of the permeabilities around this average fit is orders of magnitude at porosities from 0.15 to 0.90 (Fig. 8). The range of permeabilities displayed in Figure 8 also can be bound by two power-law fits. The lower bound is constrained by permeability measurements below 10^{-14} m^2: $k_1 = 1.5x10^{-14}\Phi^{1.8}$. The upper bound is dominated by the high permeability basaltic foams of Saar and Manga (1999) and of Bai et al. (2010), and can be described by a power law of $k_1 = 1.5x10^{-10}\Phi^{4.0}$. More than 90 % of the viscous permeability determinations in Figure 8, including those of this study, fall within the boundaries defined by these two power-laws.

Percolation theory can explain the great increase in permeability between 0 and 0.30 porosity. This theory predicts that at about 0.29 porosity an ensemble of inter-penetrating, equivalent diameter spheres that are randomly distributed in three-dimensional space will create a spanning, permeable network of connected porosity (Domb 1972; Lorenz and Ziff 2001). The permeability at porosities below 0.3 and the lack of permeability in some foams at porosities as high as ~ 0.8 (e.g., Takeuchi et al. 2008, 2009; Lindoo et al. 2016; Burgisser et al. 2017) may reflect the observations that the percolation threshold in finite systems does not necessarily occur at a specified porosity for a non-infinite system

(Stauffer and Aharony 1994; Colombier et al. 2017). Possibly the permeabilities at low porosities are controlled by the percolation threshold for hard spheres, which has been determined at a porosity of 0.1938 (Ogata et al. 2005) or 0.1990 (Ziff and Torquato 2017). Another possibility is that a non-constant size distribution of bubbles will affect the percolation threshold. However, Consiglio et al. (2003) and Ogata et al. (2005) demonstrated that the effect of the non-uniform size distributions they investigated on the percolation threshold was not significant for interpenetrating spheres and hard spheres, respectively. However, Burgisser et al. (2017) demonstrated with their experimental samples that the separation distance between bubbles weighted by the polydispersity of the bubble sizes affected the percolation threshold.

On the other hand, bubble shape plays a significant role in controlling the percolation threshold. Garboczi et al. (1995) demonstrated that the continuum percolation threshold for randomly oriented, inter-penetrating, prolate ellipsoids decreased from the porosity value for spheres of 0.29 (e.g., Lorenz and Ziff 2001) to 0.26 for an aspect ratio of 2, to 0.18 for an aspect ratio of 4, to 0.09 for an aspect ratio of 10, to 0.007 for an aspect ratio of 100, and to 0.0001 for an aspect ratio of 500. Thus, the presence of a small fraction of ellipsoidal bubbles (e.g., tube pumices) or cracks in a sample could provide an explanation of the permeabilities of volcanic foams whose porosities are below the percolation threshold for mono-disperse spheres.

Although percolation theory and the simple power-law relationships between porosity and permeability support the expected relationship between these two foam properties, permeability variations of up to 4 orders-of-magnitude at similar porosities clearly indicate that, in addition to porosity, there are other properties of the foams, such as the size distributions of bubbles and pore throats, influencing their permeability, as discussed above.

Both crystallinity and bubble anisotropy have been shown to influence the permeability of natural and experimental magmatic foams, however these influences were not investigated in this study. Degruyter et al. (2010), Schneider et al. (2012), and Burgisser et al. (2017) provide multiple examples of the effects of preferred bubble orientation on magma permeability. The effect of crystals on permeability development in magmatic foams was investigated experimentally in Bai et al. (2011) and Lindoo et al. (2017). Nevertheless, the permeabilities of crystal-rich magmatic samples determined by Saar and Manga (1999), Mueller et al (2008), Bai et al. (2011), Farquharson et al. (2015), Kushnir et al. (2016), and Lindoo et al. (2017) also plot in the same region as the aphyric-to-low-crystallinity samples, but are not shown in Figure 8.

Comparison of measurements with the models of Degruyter et al. (2010) and Burgisser et al. (2017)

The complexity of the relationship between porosity and permeability displayed in Figure 8 has been noted before by many authors, and many models for the calculation of permeability have been constructed and demonstrated to reproduce the results of the individual studies (e.g., Saar and Manga 1999; Mueller et al., 2005; Polacci et al., 2008; Bai et al., 2010; Degruyter et al., 2010; Lindoo et al., 2016; Burgisser et al. 2017; LaSpina et al. 2017). Most recently, Burgisser et al. (2017) developed a model for permeability calculations based on modifications and extensions of concepts and equations developed in Degruyter et al. (2010) and successfully applied their new model to multiple data sets.

Burgisser et al. (2017) used a modification of the channel-based Carman-Kozeny relationship to model viscous permeability:

$$k_1 = \frac{\Phi_c^n d_t^2}{16\chi\tau^2}, \quad (6)$$

where ϕ_c^n is the connected porosity raised to the nth power, d_t is the characteristic diameter of pore throats, χ is the channel circularity:

$$\chi = \left(\frac{r^2}{l^2} + \frac{l^2}{r^2}\right), \tag{7}$$

where r is the equivalent circle radius of the throat and l is its major axis (χ = 2 for circular pore throats, Degruyter et al. 2010), and τ is the tortuosity. Degruyter et al. (2010) set n = 1 in this equation for their study, but Burgisser et al. (2017) fit their data with this equation and determined a value of n = 2.49. Burgisser et al. (2017) found that this fit reproduced 26 of their 28 viscous permeability measurements to within one log unit.

Equation 6 was applied to the samples produced in this study for which the appropriate variables were measured (Table 2) to predict permeabilities using both the value of n = 1 from Degruyter et al. (2010) and of n = 2.49 from Burgisser et al. (2017); in both applications the value of χ was set to 2 (Degruyter et al. 2010). The quality of the model fit to the data was assessed by calculating chi-squared as defined by:

$$\text{chi} - \text{squared} = \sum \frac{(\log[\text{calculated permeability}] - \log[\text{measured permeability}])^2}{((\log[\text{measured permeability}]))}. \tag{8}$$

Application of the Degruyter et al. (2010) formulation of Equation 6 with d_t equaling the average pore-throat diameter, χ = 2 and n = 1 predicted the permeabilities of 17 out of 23 permeability determinations to within 1 log unit (all were within 1.6 log units) and produced a chi-squared value of 1.13 (Fig. 9a). With Burgisser et al.'s (2017) value of n = 2.49, 19 permeability predictions were within 1 log unit of our determinations (all were within 1.4 log units), and the chi-squared value was 1.14 (Fig. 9a). The fit of these models to the measurements of this study is impressive when considering the almost 5 orders of magnitude spread in the lattice-Boltzmann permeabilities; however the trend between predicted and measured permeabilities is at high angles to the slope of the perfect 1:1 correlation line between model and measurement (Fig. 9a), indicating the need for further model refinement.

Toward a better model of the viscous permeability of magmatic foams by considering the largest pore throat area

We wish to improve upon the models of Degruyter et al. (2010) and Burgisser et al. (2017) using the lattice-Boltzmann permeabilities found in this study. However, there are three caveats that must be considered for the model discussed below. The first is that the model is only calibrated for permeabilities between ~ 10^{-15} and 10^{-10} m^2. The second is that we have no technique to determine when an individual sample becomes permeable, although we can approximate the permeability threshold at $\Phi \sim 0.3$ (the percolation threshold for interpenetrating spheres) or use the methods presented in Burgisser et al. (2017) to estimate the permeability threshold if no other information is available. The third caveat is that the model is probably only applicable to isotropic, or nearly isotropic, samples.

Fluid conductivity in porous media can be related to a random resistor network by application of percolation theory (Stauffer and Aharony 1994; Blower et al. 2001). Applying this paradigm, the porous network can be envisioned as resistors interconnected to one another that create a continuous circuit when the permeability threshold is exceeded and fluid can flow across the sample. The connections between resistors in the network can be either in parallel or in series (Stauffer and Aharony 1994; Blower et al. 2001). The conductivity of the network is related to the specifics of the pore throat cross-sectional area, as expressed in the numerator of the Carman-Kozeny relationship as the square of the characteristic throat diameter, d_c^2 (Equation 6). Given a complete description of the lengths and diameters of the pore throats, together with detailed information about their connections in either series or parallel sub-circuits, a complete model of sample permeability should be calculable, but these data are not available. However, by making the simplifying assumption that the largest pore throat dominates the permeability (as the minimum-valued resistor in a parallel circuit dominates the current flow), the width of that throat, d_{max}, can be used as the characteristic pore throat diameter in Equation 6. Support for the idea of parallel connections between bubbles is provided by the high values of the connective density, ranging from 10^3 to 10^4 mm^{-3} (Table 2). Replacing the average throat diameter with the maximum throat diameter, and leaving $\chi = 2$, in Equation 6 did not significantly improve the fit of either the Degruyter et al. (2010) or Burgisser et al. (2017) models; however the Burgisser et al. (2017) model yielded calculated permeabilities consistently above the measured ones by a factor of 5. Based upon this observation, an empirical value of $\chi = 10$ (or a fitting factor of 5 times the original value of $\chi = 2$) was chosen, and the resulting fit of the Burgisser et al. model to the data is remarkable (Fig. 9b), with all but one of the measurements reproduced to within one log unit and a chi-squared value of 0.01. The Degruyter et al. (2010) model also reproduces all but one of the measurements to within 1 log unit, but yields a chi-squared value twice that of the Burgisser et al. model, 0.02.

The challenge in applying this model to predict permeability from porosity measurements is that the tortuosity and the maximum throat diameter needed for the calculation typically are not known (cf. Burgisser et al. 2017). In most cases, published studies only provide the average bubble diameter and the porosity. However, the relationship found in this study between tortuosity and porosity (Eqn. 5a) can be used to estimate the tortuosity. Additionally, we found that the maximum throat diameter can be related to the average bubble size, d_{avg}^{bubble} (m), by

$$d_{\max} = 2.22251x10^{-5}\ln\left(d_{\text{avg}}^{\text{bubble}}\right) + 2.69501x10^{-4}. \quad (9)$$

To test this model, the permeabilities of samples within the range of our calibration, 10^{-15} to 10^{-10} m^2, from Bai et al. (2010) and the isotropic pumices of Burgisser et al. (2017) were estimated using the correlations between tortuosity and porosity and between the average bubble size and the maximum throat diameter (Fig. 9c). We did not apply the model to the non-isotropic samples of Burgisser et al. (2017) because we are unsure whether our correlations would apply to these samples and lack the necessary data to test our model on non-isotropic samples.

Although there is clearly a degradation in the accuracy of the model when the correlations are used to estimate the tortuosity and maximum throat diameter rather than their measured values (cf. Fig. 9c with Fig. 9b), the permeability of 11 of the 14 samples from Bai et al. (2010) are reproduced within 1 log unit, and the maximum difference between all estimated and measured permeabilities is 1.9 log units. The chi-squared value (Eqn. 8) for all of the Bai et al. (2010) and the model is 0.77. The estimated permeabilities of all 13 isotropic samples from Burgisser et al. (2017) are within 0.9 of a log unit of the measured values, and the chi-squared value is 0.35. The accuracy of this model is similar to that reported by Burgisser et al. (2017) who found that their fit to Equation 6 could reproduce 26 out of the 28 (isotropic and anisotropic) samples they investigated to within 1 log unit.

This test of the model indicates its utility for estimating the permeability of samples with knowledge of only the porosity and the average bubble diameter. However, as shown in Figure 9c, the model has a tendency to overestimate the permeabilities by a factor of ~5. An ad hoc correction could be made for this overestimation, but even without such correction the test indicates that permeabilities can be calculated to within an order of magnitude with the model.

Role of bubble growth rate on permeability

Although we were unable to successfully determine permeabilities at the same porosity from experiments with the same composition at different heating rates, our results agree with previous studies indicating that bubble growth rates significantly influence permeabilities (Rust and Cashman 2004; Burgisser and Gardner 2004; Mueller al. 2005, 2008; Takeuchi et al. 2009; Castro et al. 2012;

Lindoo et al. 2016). In particular, Lindoo et al. (2016) noted that increasing decompression rates in their experiments, leading to increasing bubble growth rates, resulted in an increasing percolation threshold. This hypothesis is consistent with two observations on the basaltic composition where the slowly heated experiment DRB2012-7f-10 (1 °C s^{-1}) with a porosity of 0.55 has a permeability (1.5 x 10^{-11} m^2) similar to the rapidly heated (6 °C s^{-1}), 0.73 porosity experiment DRB2012-7c-f (2.9 x 10^{-11} m^2), whereas the fit from Bai et al. (2010) predicts a permeability of at least 5 x 10^{-11} m^2 at a porosity of 0.73.

We also note that there may be a correlation between the bubble growth rate and the size distribution of pore throats that significantly influences permeability. We propose this tentative hypothesis because of the often-lower permeabilities of the rapidly heated (5 °C min^{-1}) andesitic foam in comparison to the more slowly heated (~1 °C min^{-1}) trachyandesitic and dacitic foams with similar porosities (Table 2, Figure 7).

Despite the need for further experiments to quantitatively constrain the effects of decompression and growth rates on the permeability of silicate foams, we suggest that the orders-of-magnitude variability seen in permeability at similar porosities in Figure 8 is significantly controlled by the bubble growth rate. The formation of a pore throat between two bubbles requires them to partially coalesce; for coalescence to occur the interbubble melt film (IBF) must thin to the point where it fails, estimated to be a thickness of 0.5 μm in a rhyolitic melt by Castro et al. (2012). The rate at which the IBF thins is a function of the surface tension and bubble size (Equation 4), and the timescales of thinning vary from less than a second (basaltic melts) to thousands of seconds (dacitic melts), based upon the analyses of Castro et al. (2012) and Nguyen et al. (2013). In the case where bubbles are growing on a timescale shorter than that of IBF thinning, coalescence is not as effective in creating large pore throats as at slower growth rates, and permeabilities at equal porosities are lower than in the case where bubble growth is slower than IBF thinning. Consideration of the lubrication and drag forces during bubble growth suggests the possibility of a bubble-size-dependence of connectivity (and therefore permeability). These considerations will be explored in future studies.

Although we think that the rate of gas exsolution plays a significant role in creating the wide spread of permeability at equivalent porosities, we recognize that other factors may affect the observed variations in permeability, such as the effects of bubble orientation (e.g., Degruyter et al. 2010; Burgisser et al. 2017) and the presence of crystals in the magma (e.g., Bai et al. 2011; Lindoo et al. 2017).

Conclusions

A complete characterization of magmatic foams is required to model permeability because permeability-porosity relationships alone do not provide sufficient data for accurate modeling and prediction. Furthermore, average properties of the foam, in particular average pore-throat diameters, appear to be insufficient to fully characterize permeability. Complete measurements of porosity, bubble and pore throat size distributions, as well as tortuosity, are required to model accurately the permeability of magmatic foams. In particular, we stress the apparent importance of the largest pore throat on the permeability of magmatic foams. We propose one such model, which we consider a step in the right direction, that can be used to benchmark future studies. The results of this study are consistent with previous work indicating the importance of the bubble growth rate on the permeability of magmatic foams. Higher growth rates appear to produce lower permeabilities, and the effect of growth rate on permeability may explain a significant portion of the orders-of-magnitude spread in permeabilities at similar porosity.

Acknowledgements

D.R. Baker thanks NSERC for their continued support for his research through the Discovery Grant Program. All of the members of the TOMCAT team and of the Swiss Light Source at the Paul Scherrer Institut are thanked for their creation of the facility that allowed this study to be done and their continuing dedication to providing support to external users of the beamline.

We also thank the editor, K. Cashman and the reviewers H. Wright, L. Chevalier and A. Burgisser for their detailed and thoughtful comments that significantly improved the presentation of our research in this contribution.

References

Al-Raoush RI, Madhoun IT (2017) TORT3D: A MATLAB code to compute geometric tortuosity from 3D images of unconsolidated porous media, Powder Tech 320: 99-107

Archie GE (1942) The electrical resistivity log as an aid in determining some reservoir characteristics. Trans Am Inst Mineral Meteorol 146:54-62.

Bai L, Baker DR, Hill RJ (2010) Permeability of vesicular Stromboli basaltic glass: Lattice Boltzmann simulations and laboratory measurements. J Geophys Res 115:B07201. doi:10.1029/2009JB007047

Bai L, Baker DR, Polacci M, Hill RJ (2011) In-situ degassing study on crystal-bearing Stromboli basaltic magmas: Implications for Stromboli Eruptions. Geophys Res Lett 38: L17309

Baker DR (2004) Piston-cylinder calibration at 400 to 500 MPa: a comparison of using water solubility in albite melt and NaCl melting. Am Mineral 89:1553–1556

Baker DR Eggler DH (1987) Compositions of anhydrous and hydrous melts coexisting with plagioclase, augite, and olivine or low-Ca pyroxene from 1 atm. to 8 kbar: application to the Aleutian volcanic center of Atka. Am Mineral 72:12-28

Baker DR, Polacci MR, LaRue A (2011) A study on the reproducibility of counting vesicles in volcanic rocks. Geosphere, doi: 10.1130/GES00553.1

Baker DR, Brun F, O'Shaughnessy C, Mancini L, Fife JL, Rivers M (2012) A four-dimensional X-ray tomographic microscopy study of bubble growth in basaltic foam. Nat Comm 3: 1135. doi:10.1038/ncomms2134

Blower JD (2001) Factors controlling permeability-porosity relationships in magmas. Bull Volcanol 63:497-504

Bouvet de Maisonneuve C, Bachmann O, Burgisser A (2008) Characterization of juvenile pyroclasts from the Kos Plateau Tuff (Aegean Arc): insights into the eruptive dynamics of a large rhyolitic eruption. Bull Volcanol doi: 10.1007/s00445-008-0250-x

Browne B, Szramek L (2015) Chapter 9: Rates of magma ascent and storage. The Encyclopedia of Volcanoes. Elsevier Inc. http://dx.doi.org/10.1016/B978-0-12-385938-9.00009-2

Brun F, Dreossi D (2010) Efficient curve-skeleton computation for the analysis of biomedical 3D images. Biomed Sci Instrum 46:475-480

Brun F, Mancini L, Kasae P, Favretto S, Dreossi D, Tromba G (2010) Pore3D: A software library for quantitative analysis of porous media. Nucl Instr Methods Phys Res A 615:326-332

Burgisser A, Gardner JE (2004) Experimental constraints on degassing and permeability in volcanic conduit flow. Bull Volcanol 67:42–56. http://dx.doi.org/10.1007/s00445-004-0359-5

Burgisser A, Chevalier L, Gardner JE, Castro JM (2017) The percolation threshold and permeability evolution of ascending magmas. Earth Planet Sci Lett 470:37-47

Carman PC (1937) Fluid flow through a granular bed. Trans Inst Chem Eng London, 15:150-156

Castro JM, Burgisser A, Schipper CI, Mancini S (2012) Mechanisms of bubble coalescence in silicic magmas. Bull Volcanol 74:2339–2352

Colombier M, Wadsworth FB, Gurioli L, Scheu B, Kueppers U, Di Muro A, Dingwell DB (2017) The evolution of pore connectivity in volcanic rocks. Earth Planet Sci Lett 462:99-109

Consiglio R, Baker DR, Paul G, Stanley HE (2003) Continuum percolation thresholds for mixtures of spheres of different sizes. Physica A 319:49-55

Cox SJ, Graner F (2004) Three-dimensional bubble clusters: Shape, packing, and growth rate. Phys Rev E 69: 031409

Degruyter W, Bachmann O, Burgisser A (2010) Controls on magma permeability in the volcanic conduit during the climatic phase of the Kos Plateau Tuff eruption (Aegean Arc). Bull Vulcanol 72:63-74

Domb C (1972) A note on the series expansion method for clustering problems. Biometrika 59:209-211

Dowd B, Campbell GH, Marr RB, Nagarkar V, Tipnis S, Axe L, Siddons DP (1999) Developments in synchrotron x-ray computed tomography at the National Synchrotron Light Source. Developments in X-Ray Tomography II, Proc SPIE 3772:224-236

Fagents SA, Gregg TKP, Lopes RMC (2013) Modeling Volcanic Processes: The Physics and Mathematics of Volcanism. Cambridge University Press, Cambridge, 421 p

Farquharson J, Heap MJ, Varley NR, Baud P, Reushclé T (2015) Permeability and porosity relationships of edifice-forming andesites: A combined field and laboratory study. Jour Volcan Geotherm Res 297:52-68

Ferguson DJ, Gonnermann HM, Ruprech P, Plank T, Hauri EH, Houghton BF, Swanson DA (2016) Magma decompression rates during explosive eruptions of Kilauea volcano, Hawaii, recorded by melt embayments. Bull Volcanol 78:71

Fife JL, Rappaz M, Pistone M, Celcer T, Mikuljan G, Stampanoni M (2012) Development of a laser-based heating system for in-situ synchrotron-based x-ray tomographic microscopy, J. Synchrotron Radiation 19:352-358

Fortin M-A, Riddle J, Desjardins-Langlais Y, Baker DR (2015) The effect of water on the sulfur concentration at sulfide saturation (SCSS) in natural melts. Geochim Cosmochim Acta 160:100-116

Gaonac'h H, Lovejoy S, Stix J, Scherzter D (1996) A scaling growth model for bubbles in basaltic lava flows. Earth Planet Sci Lett 139:395-409.

Garboczi EJ, Snyder KA, Douglas JF, Thorpe MF (1995) Geometrical percolation threshold of overlapping ellipsoids. Physical review E 52:819-828

Giordano D, Nichols ARL, Dingwell DB (2005) Glass transition temperatures of natural hydrous melts: a relationship with shear viscosity and implications for the welding process. J Volcan Geotherm Res 142: 105-118

Giordano D, Russell JK, Dingwell DB (2008) Viscosity of magmatic liquids: A model. Earth Planet Sci Lett 278:123-134

Hildebrand T, Rüegsegger P (1997) A new method for the model-independent assessment of thickness in three-dimensional images. J Microscopy 185:67-75

Hill RJ, Koch DL,Ladd AJC (2001) The first effects of fluid inertia on flows in ordered and random arrays of spheres. J Fluid Mech 448:213–241. doi:Ziff10.1017/S0022112001005948

Hill RJ, Koch DL (2002) The transition from steady to weakly turbulent flow in a close-packed ordered array of spheres. J Fluid Mech 465:59–97. doi:10.1017/S0022112002008947

Humphreys MCS, Menand T, Blundy JD, Klimm K (2008) Magma ascent rates in explosive eruptions: Constraints from H_2O diffusion in melt inclusions. Earth Planet Sci Lett 270:25-40

Klug C, Cashman KV (1996) Permeability development in vesiculating magmas: implications for fragmentation. Bull Volcan 58:87-100

Kraynik AM, Reinelt DA, van Swol F (2004) Structure of random foam. Phys Rev Lett 93: 208301, 10.1103/PhysRevLett.93.208301

Kushnir ARL, Martel C, Bourdier J-L, Heap MJ, Reushclé T, Erdmann S, Komorowski J-C, Cholik N (2016) Probing permeability and microstructure: Unravelling the role of a low-permeability dome on the explosivity of Merapi (Indonesia). Jour Volcan Geotherm Res 316:56-71

LaRue A (2012) Bubble size distributions and magma-water interaction at Eyjafjallajökull volcano, Iceland. M.Sc. Thesis, McGill University

La Spina G, Polacci M, Burton M, de' Michieli Vitturi M (2017) Numerical investigation of permeability models for low viscosity magmas: Application to the 2007 Stromboli effusive eruption. Earth Planet Sci Lett 473:279-290. https://doi.org/10.1016/j.epsl.2017.06.013

Lindoo A, Larsen JF, Cashman KV, Dunn AL, Neill OK (2016) An experimental study of permeability development as a function of crystal-free melt viscosity. Earth Planet Sci Lett 435:45-54

Lindoo A, Larsen JF, Cashman KV, Oppenheimer J (2017) Crystal controls on permeability development and degassing in basaltic andesite magma. Geology 45: 831-834

Lindquist WB (2002) Quantitative analysis of three dimensional X-ray tomographic images. Proc. SPIE 4503:103-115

Lindquist WB, Lee SM (1996) Medial axis analysis of void structure in three-dimensional tomographic images of porous media. J. Geophys Res 101:8297-8310

Liu Y, Samaha N-T, Baker DR (2007) Sulfur concentration at sulfide saturation (SCSS) in magmatic silicate melts. Geochim Cosmochim Acta 71:1783-1799

Liu Y, Zhang Y, Behrens H (2005) Solubility of H_2O in rhyolitic melts at low pressures and a new empirical model for mixed H_2O-CO_2 solubility in rhyolitic melts. J Volcan Geotherm Res 143:219-235

Lorenz CD, Ziff RM (2001) Precise determination of the critical percolation threshold for the three-dimensional 'Swiss cheese' model using a growth algorithm. J Chem Phys 114:3659-3661

Marone F, Stampanoni M (2012) Regridding reconstruction algorithm for real time tomographic imaging. J Synchrotron Rad 19:1029-1037

Mokso R, Marone F, Stampanoni M (2010) Real time tomography at the Swiss Light Source. AIP Conf Proc 1234:87-90

Mokso R, Schlepuetz CM, Theidel G, Billich H, Schmid E, Celcer T, Mikuljan G, Sala L, Marone F, Schlumpf N, Stampanoni M (2017) GigaFRoST: The Gigabit Fast Readout System for Tomography. Jour Synchrotron Rad doi.org/10.1107/S1600577517013522

Mueller S, Melnik O, Spieler O, Scheu B, Dingwell DB (2005) Permeability and degassing of dome lavas undergoing rapid decompression: An experimental determination. Bull Volcan 67:526-538

Mueller S, Scheu B, Spieler O, Dingwell DB (2008) Permeability control on magma fragmentation. Geology 36:499-402

Navon O, Lyakhovsky, V, (1998) Vesiculation processes in silicic magmas. In: Gilbert, J.S., Sparks, R.S.J. (Eds.), The Physics of Explosive Volcanic Eruptions. Geol Soc Spec Pub Lond 145: 27–50.

Neuville DR, Courtial P, Dingwell DB, Richet P (1993) Thermodynamic and rheological properties of rhyolite and andesite melts. Contrib Mineral Petrol 113:572-581

Newman MEJ (2005) Power laws, Pareto distributions and Zipt's law. Contemporary Physics 46:323-351

Nguyen CT, Gonnermann HM, Chen Y, Huber C, Maiorano AA, Gouldstone A, Dufek J (2013) Film drainage and the lifetime of bubbles. Geochem Geophys Geosys 14: 10.1002/ggge.20198

Ni H, Zhang L (2018) A general model of water diffusivity in calcalkaline silicate melts and glasses. Chem Geol 478:60-68.

Odgaard A, Gundersen HJG (1993) Quantification of connectivity in cancellous bone, with special emphasis on 3-D reconstructions. Bone 14:173-182

Ogata R, Odagaki T, Okazaki K (2005) Effects of poly-dispersity on continuum percolation. J Phs Condens Matter 17:4531-4538

Papale P, Moretti R, Barbato D (2006) The compositional dependence of the saturation surface of H_2O + CO_2 fluids in silicate melts. Chem Geol 229:78-95

Polacci M, Baker DR, Bai L, Mancini L (2008) Large vesicles record pathways of degassing at basaltic volcanoes. Bull Volcanol 70:1023-1029. https://doi.org/10.1007/s00445-007-0184-8

Polacci M, Baker DR, La Rue A, Mancini L, Allard P (2012) Degassing behaviour of vesiculated basaltic magmas: an example from Ambrym volcano, Vanuatu Arc. Jour Volcan Geotherm Res 233-234:55-64.

Polacci M, Bouvet de Maisonneuve C, Giordano D, Piochi M, Mancini L, Degruyter W, Bachmann O (2014) Permeability measurements of Campi Flegrei pyroclastic products: An example from the Campanian Ignimbrite and Monte Nuovo eruptions. Jour Volcan Geotherm Res 2272:16-22.

Rivers ML, Wang Y (2006) Recent developments in microtomography at GeoSoilEnviroCARS.

Developments in X-Ray Tomography V, Proc SPIE 6318:J3180. doi: 10.1117/12.681144

Rust AC, Cashman KV (2004) Permeability of vesicular silicic magma: Inertial and hysteresis effects. Earth Planet Sci Lett 228:93-107

Rust AC, Cashman KV (2011) Permeability controls on expansion and size distributions of pyroclasts. J Geophys Res 116:B11202

Saar MO, Manga M (1999) Permeability-porosity relationship in vesicular basalts. Geophys Res Lett 26:111-114

Schneider A, Rempel AW, Cashman KV. (2012) Conduit degassing and thermal controls on eruption styles at Mount St. Helens. Earth Planet Sci Lett 357-358: 347-354

Shaw HR (1972) Viscosities of magmatic silicate liquids: an empirical method of prediction. Am J Sci 272:870-893

Sparks RSJ (2003) Dynamics of magma degassing. In: Oppenheimer, C., Pyle, D.M., and Barclay, J. (eds) Volcanic Degassing. Geological Society, London, Special Publications 213:5-22

Spieler O, Kennedy B, Kueppers U, Dingwell DB, Scheu B, Taddeucci J (2004) The fragmentation threshold of pyroclastic rocks. Earth Planet Sci Lett 226:139-148

Stauffer D, Aharony A. (1994) Introduction to Percolation Theory, 2nd Edition. Taylor & Francis, London, 181 p

Takeuchi S, Nakashima S, Tomiya A (2008) Permeability measurements of natural and experimental volcanic materials with a simple permeameter: Toward and understanding of magmatic degassing processes. J Volcan Geotherm Res 177:329-339.

Takeuchi S, Tomiya A, Shinohara H (2009) Degassing conditions for permeable silicic magmas: implications from decompression experiments with constant rates. Earth Planet Sci Lett 283:101–

110. http://dx.doi.org/10.1016/j.epsl.2009

Thovert J.F., Salles J., Adler P.M. (1993) Computerized characterization of the geometry of real porous media: their discretization, analysis and interpretation. J. Microscopy 170:65-79

Tomasi C, Manduchi R (1998) Bilateral filtering for gray and color images. Sixth Internat Conf Comp Vision: 839-846

Wright HMN, Cashman KV, Gottesfeld EH, Roberts JJ (2009) Pore structure of volcanic clasts: Measurements of permeability and electrical conductivity. Earth Planet Sci Lett 280:93-104

Yokoyama T, Takeuchi S (2009) Porosimetry of vesicular volcanic products by a water-expulsion method and the relationship of pore characteristics to permeability. J Geophys Res 114:B0221. doi:10.1029/2008JB005758

Zandomeneghi D, Voltolini M, Mancini L, Brun F, Dreossi D, Polacci M (2010) Quantitative analysis of X-ray microtomography images of geomaterials: Application to volcanic rocks. Geosphere 6:793-804

Zhou J-Q, Chen Y-F, Wang L, Rayani Cardenas M. (2019) Universal relationship between viscous and inertial permeability of geologica porous media. Geophys Res Lett 46:1441-1448.

Ziff RM, Torquato S (2017) Percolation of disorderd jammed sphere packings. J Phys A Math Theor 50: 085001, doi:10.1088/1751-8121/aa5664

Figure Captions

Figure 1 a) Slice of complete sample DRB2012_6e_10. The 256 × 256 pixel region in this slice sampled for analysis is shown by the dashed lines. b) Detailed image of the portion of the 256 × 256 slice sampled from the larger image. c) Thresholded image of (b) with a smaller 160 × 160 pixel region used for quantitative measurements shown enclosed by the solid lines. d) Reconstruction for DRB2012-2a-19, with the one-voxel-wide-skeleton in yellow and the nodes (intersections of the skeleton branches) in red and orange, demonstrating the effect of only considering larger interconnections between bubbles by merging voxels together and taking their average. e) The same reconstruction also considering smaller interconnections based upon the finest voxel resolution. In this work the choice was made to count both large and small interconnections of the skeleton and maximize the number of possible skeleton nodes (or bubble centers) and pore throats (the skeleton connecting the nodes) measured. However this procedure can over-count the number of nodes; to reduce the number of over-counted nodes, spheres are centered at each node and isotropically inflated by differing degrees. f) This image demonstrates the effect of less inflation, producing a higher bubble count, and g) demonstrates the effect of more inflation resulting in the merger of more spheres and a smaller number of counted bubbles. The merger is best seen in the small sphere on the left-hand side of the big bubble that is not merged in (f) and would be counted as a separate bubble, but is merged in (g) and becomes part of the large bubble. h) The size of the bubble to be counted is determined by a maximal inscribed sphere that is centered on the center of mass determined from the merged bubbles. Please see text for further discussion. (Color on line)

Figure 2 a, b, c) Selected 3D renderings of andesitic experiment DRB2012-2a during vesiculation. In the earliest image the sample is approximately 1 x 1 x 2 mm in size. Due to the perspective projections of these renderings the scale bars are only approximate. Representative interior sections of these samples were chosen for quantitative analysis. d, e, f) Corresponding thresholded tomographic slices (axial slice number 128 near the center of the reconstruction) from each of the renderings shown in panels a, b and c, in which black is the melt and white is either the bubbles in the samples or the air around samples (seen in panels e and f). The 500 μm scale bar in panel d also applies to panels e and f. Melt viscosities are calculated using Giordano et al. (2008) with 5 wt.% H_2O in the melt at 900 °C and an estimated 1 wt.% H_2O at 994 °C; at 1089 °C, near the end of bubble growth, the melt is assumed to be anhydrous for the viscosity calculation. Quantitative measurements of the experiment are provided in Table 2 and Supplemental Data Table 1. Please see Supplemental data for a movie of this sample during bubble growth.

Figure 3 a) Bubble size distributions in basaltic sample DRB2012-7. The figure contains subpanels with bubble size distributions from different experiments with porosities from 0.50 to 0.73. All panels in this and subsequent plots of bubble and pore-throat size distributions are plotted in order of increasing experimental duration and temperature. Note that in this figure the sample with a porosity 0.50 was made by reheating the sample with 0.52 porosity (please see Table 2 and the text for further discussion). In each subpanel a volume-normalized histogram of the sizes of the bubbles (the bar graphs) is presented together with the cumulative distribution of the bubble sizes (solid black line). The porosity is given in the upper right corner of each subpanel. The mean bubble diameter, d, and one-standard deviation about the mean is given in each subpanel. Bin sizes are 5 μm. b) Corresponding pore throat size distributions in basaltic sample DRB2012-7. The information on the pore-throat distributions is presented in the same manner as the bubble size distributions in Part a. Bin sizes are 5 μm.

Figure 4 Bubble and pore-throat distributions for andesitic experiment DRB2012-2a. a) Bubble size distributions for porosities between 0.17 and 0.33. Bin sizes are 5 μm. b) Bubble size distributions for porosities between 0.41 and 0.59. Bin sizes are 5 μm. c) Bubble size distributions for porosities between 0.71 and 0.80. Bin sizes are 5 μm. d) Pore throat size distributions for porosities between 0.17 and 0.33. Bin sizes are 5 µm. e) Pore throat size distributions for porosities between 0.41 and 0.59. Bin sizes are 5 µm. f) Pore throat size distributions for porosities between 0.71 and 0.80. Bin sizes are 5 µm. Please see caption to Figure 3 for a complete description of figure.

Figure 5 Bubble and pore throat distributions for trachyandesitic experiment EFJ-8a. a) Bubble size distributions for porosities between 0.09 and 0.64. Bin sizes are 5 µm. b) Corresponding pore throat distributions. Bin sizes are 5 µm. Please see caption to Figure 3 for a complete description of figure.

Figure 6 Bubble and pore throat distributions for dacitic experiment DRB2012-6e. a) Bubble size distributions for porosities between 0.38 and 0.84. Bin sizes are 5 µm. b) Corresponding pore throat distributions. Bin sizes are 5 µm. Please see caption to Figure 3 for a complete description of figure.

Figure 7 Experimental foam permeabilities determined by lattice-Boltzmann simulations plotted as a function of porosity. Uncertainties in the measured porosity and in the permeability are estimated at 20 relative percent and typically the same size as, or smaller than, the symbols. The solid blue line is the power-law fit to the lattice-Boltzmann permeabilities of the andesitic composition. The proposed relationships between porosity and permeability for basaltic and for silicic compositions from Bai et al. (2010) are also plotted. (Color on line) Please see text for further discussion.

Figure 8 Permeability measurements as a function of porosity for aphyric-to-low-crystallinity vesiculated samples of basaltic to rhyolitic composition from the literature and this study. Three fits to the data are presented. Fitting all the data with a power law yields the relationship $k_1 = 6.0x10^{-12}\Phi^{4.0}$. A lower bound is constrained by fitting the permeability measurements below

10^{-14} m^2, which yields $k_1 = 1.5x10^{-14}\Phi^{1.8}$. An upper bound is defined by the high permeability measurements of Saar and Manga (1999) and of Bai et al. (2010), and is described by a power law of $k_1 = 1.5x10^{-10}\Phi^{4.0}$. Sources of the data are provided in the figure and can be found in the references. (Color on line)

Figure 9 a) Application of the models for the prediction of permeability using the Carman-Kozeny equations of Degruyter et al. (2010) and of Burgisser et al. (2017). The line labelled 1:1 represents a perfect fit of a model to the data; the line labeled "*5x*" represents the modeled values multiplied by 5 and the line labeled "*0.2x*" represents the modeled values multiplied by 0.2. In these models the average pore throat value (Table 2) was used as the characteristic diameter of pore throats. b) Modification of the models of Degruyter et al. and of Burgisser et al. by using the maximum pore throat as the characteristic diameter and an empirical value of $\chi = 10$. Note the excellent fit of the Burgisser et al. model to the measurements. c) Comparison of the modified Burgisser et al. model and measured permeabilities of samples from Bai et al. (2010) and of the isotropic samples from Burgisser et al. (2017) using relationships between the average bubble diameter and the largest throat diameter and between the porosity and the tortuosity, as determined in this study. The data from Bai et al. (2010) and from Burgisser et al. (2017) were not used to calibrate the model. Please see text for further discussion. (Color on line)

Table 1 Starting glass compositions

Table 2 Experimental results

Supplementary Movie Bubble growth in DRB2012-2a

Supplementary Data Table Measured diameters of bubbles and pore throats in the experiments.

Supplementary Figure 1 Connectivity versus porosity in the experimental samples (in color online).

Figure 1a-c

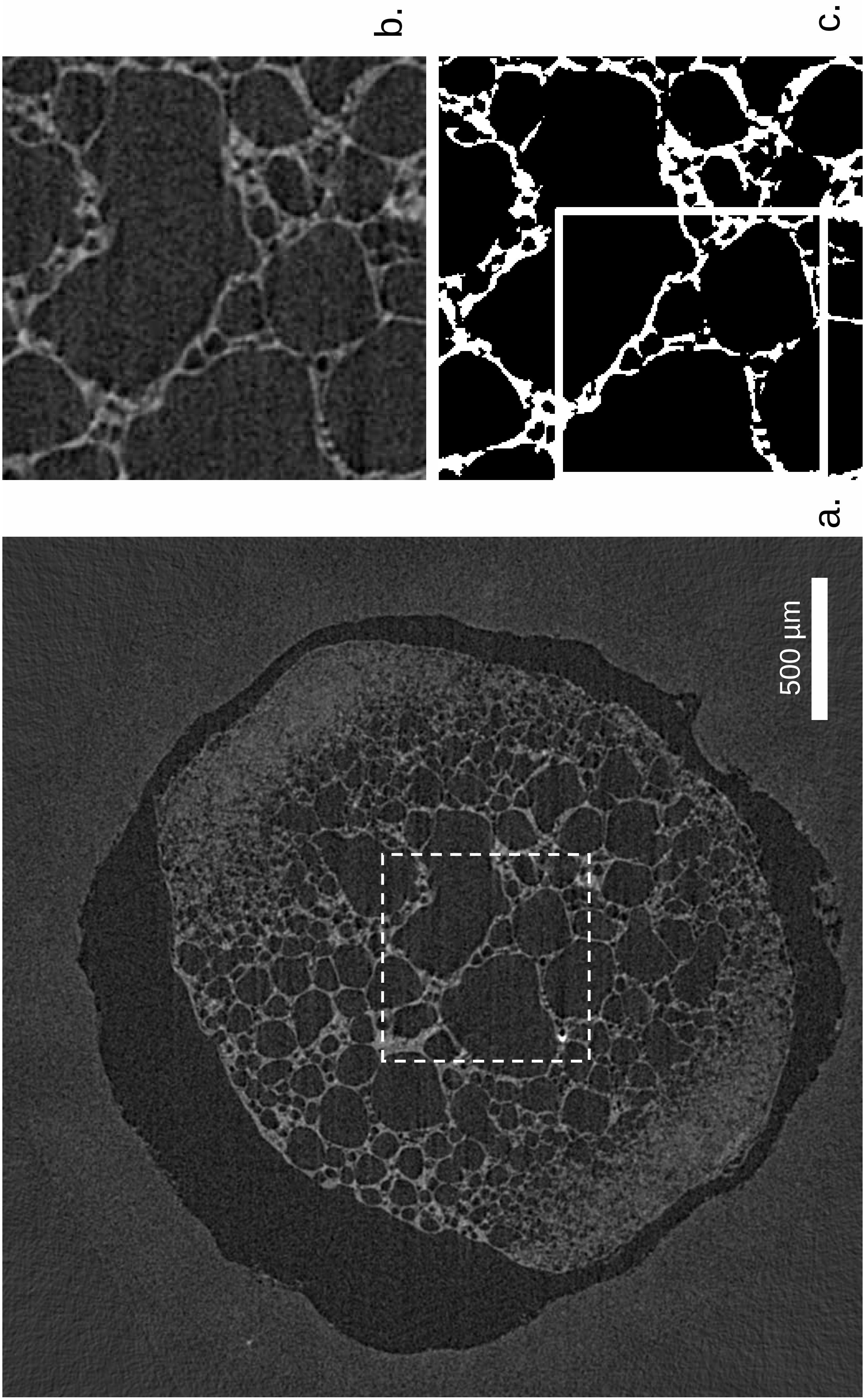

Figure 1d-e

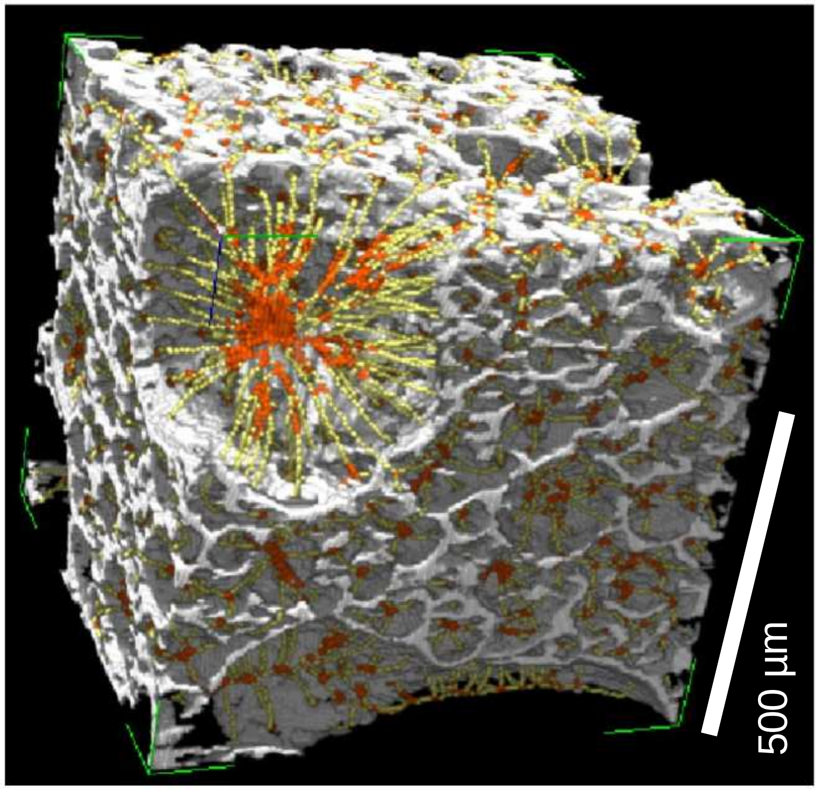

e.

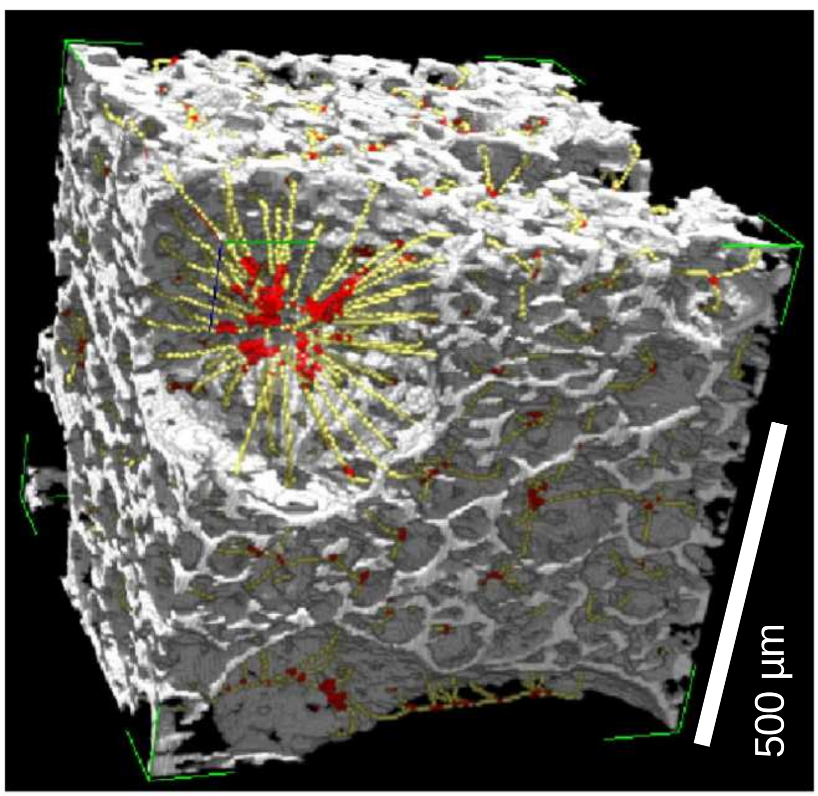

d.

Figure 1f-g

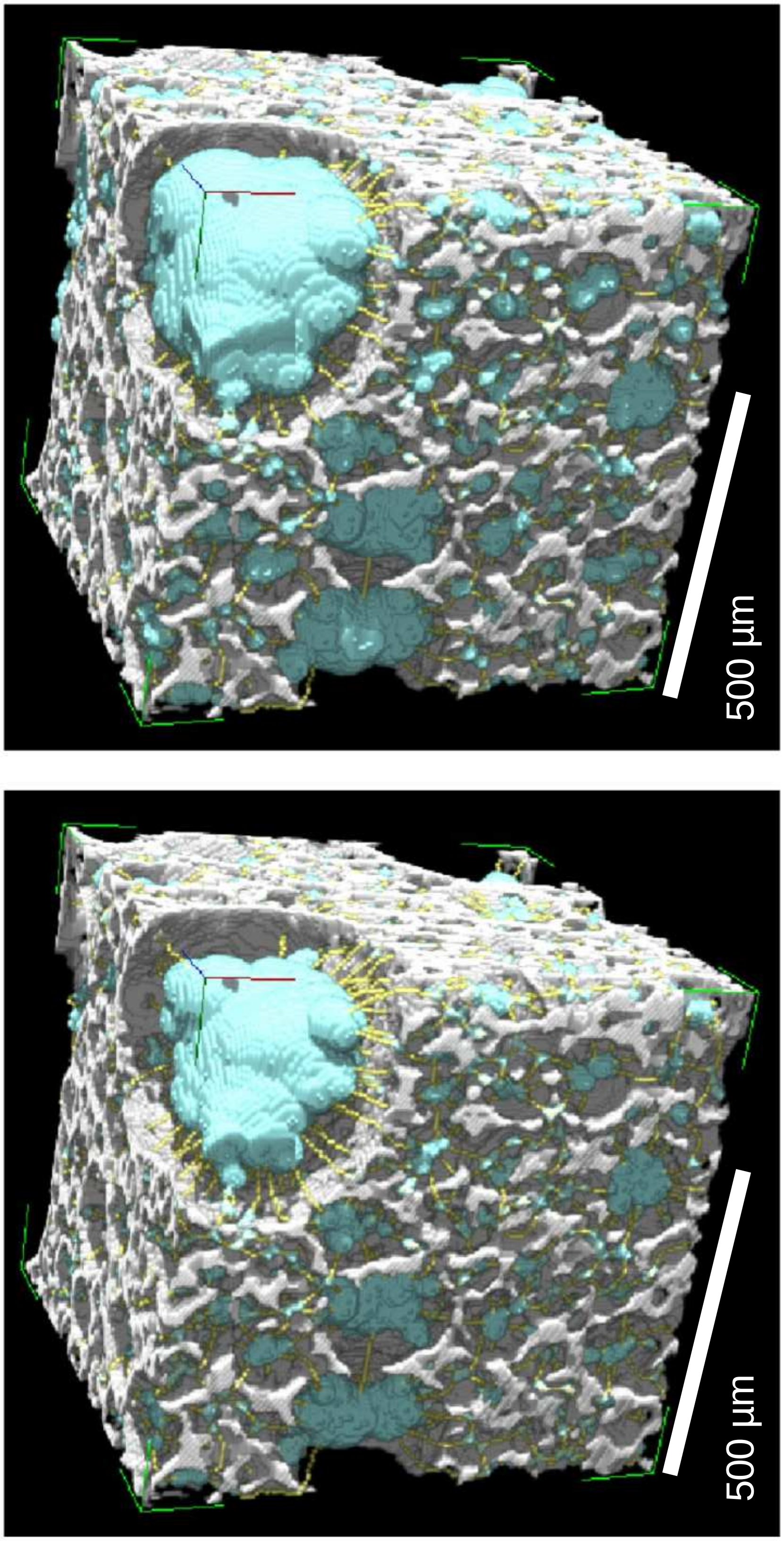

g.

f.

Figure 1h

h.

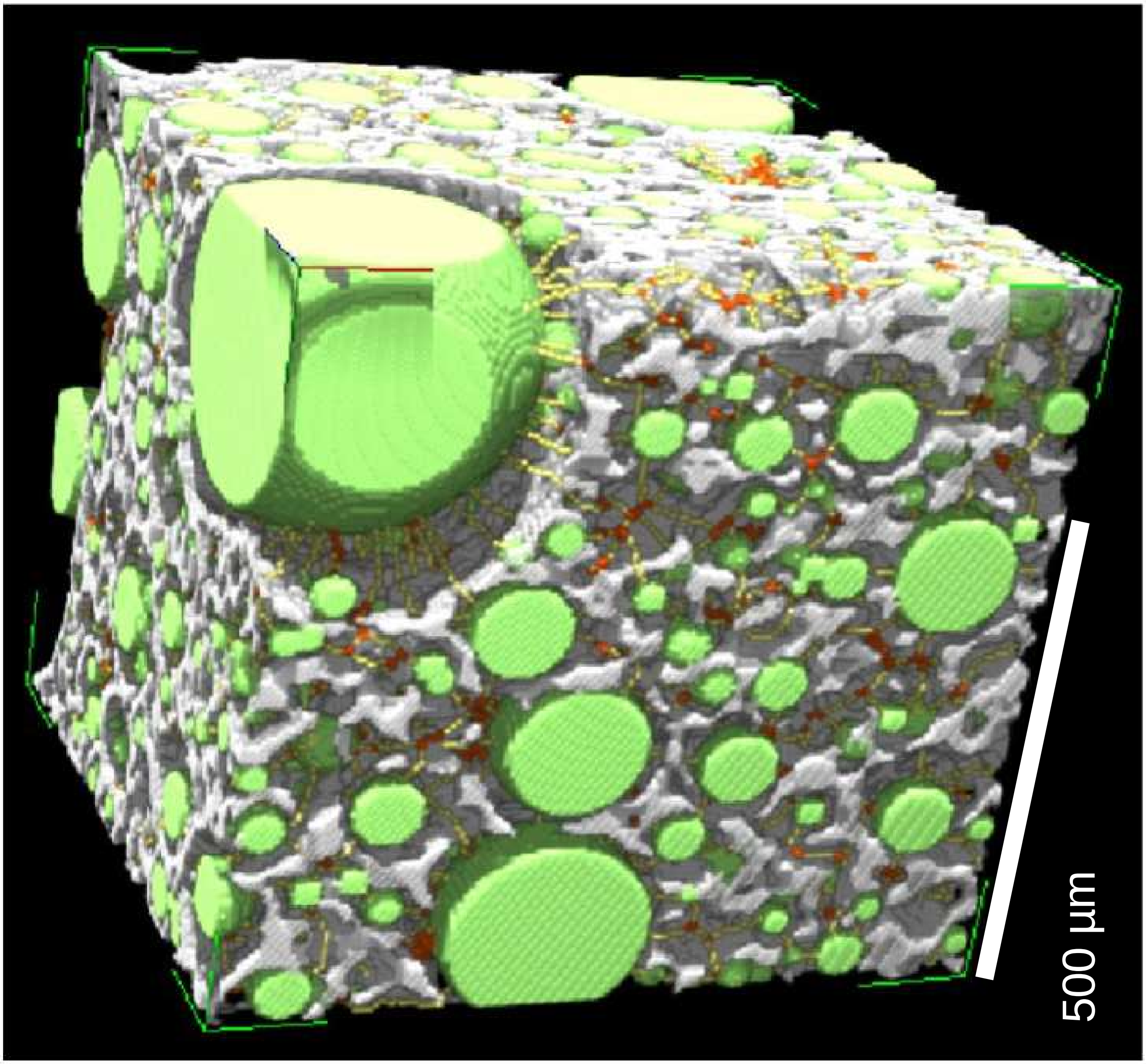

Figure 2

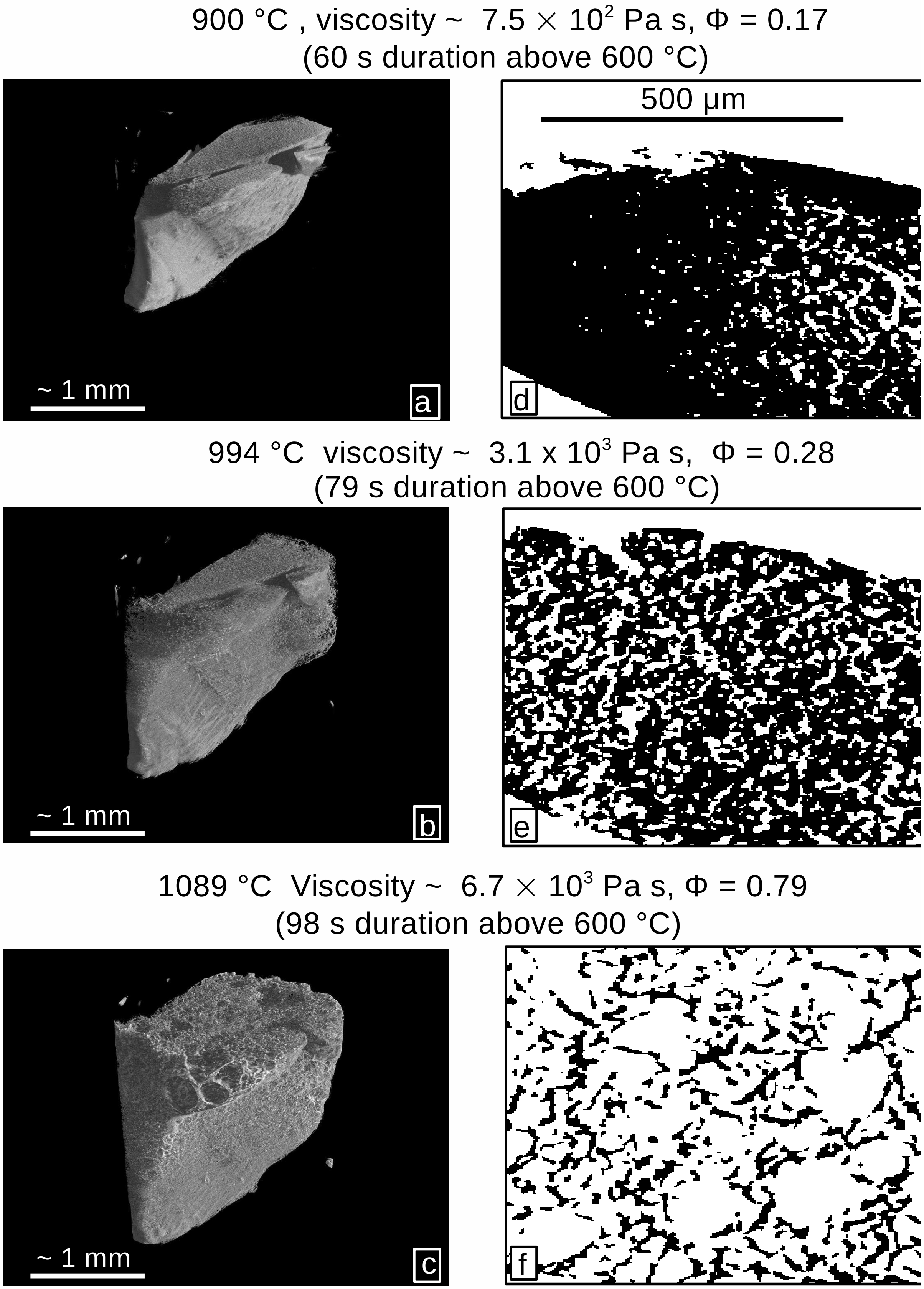

900 °C , viscosity ~ 7.5 × 10^2 Pa s, Φ = 0.17
(60 s duration above 600 °C)
500 μm
~ 1 mm
a
d
994 °C viscosity ~ 3.1 x 10^3 Pa s, Φ = 0.28
(79 s duration above 600 °C)
~ 1 mm
b
e
1089 °C Viscosity ~ 6.7 × 10^3 Pa s, Φ = 0.79
(98 s duration above 600 °C)
~ 1 mm
c
f

Figure 3a

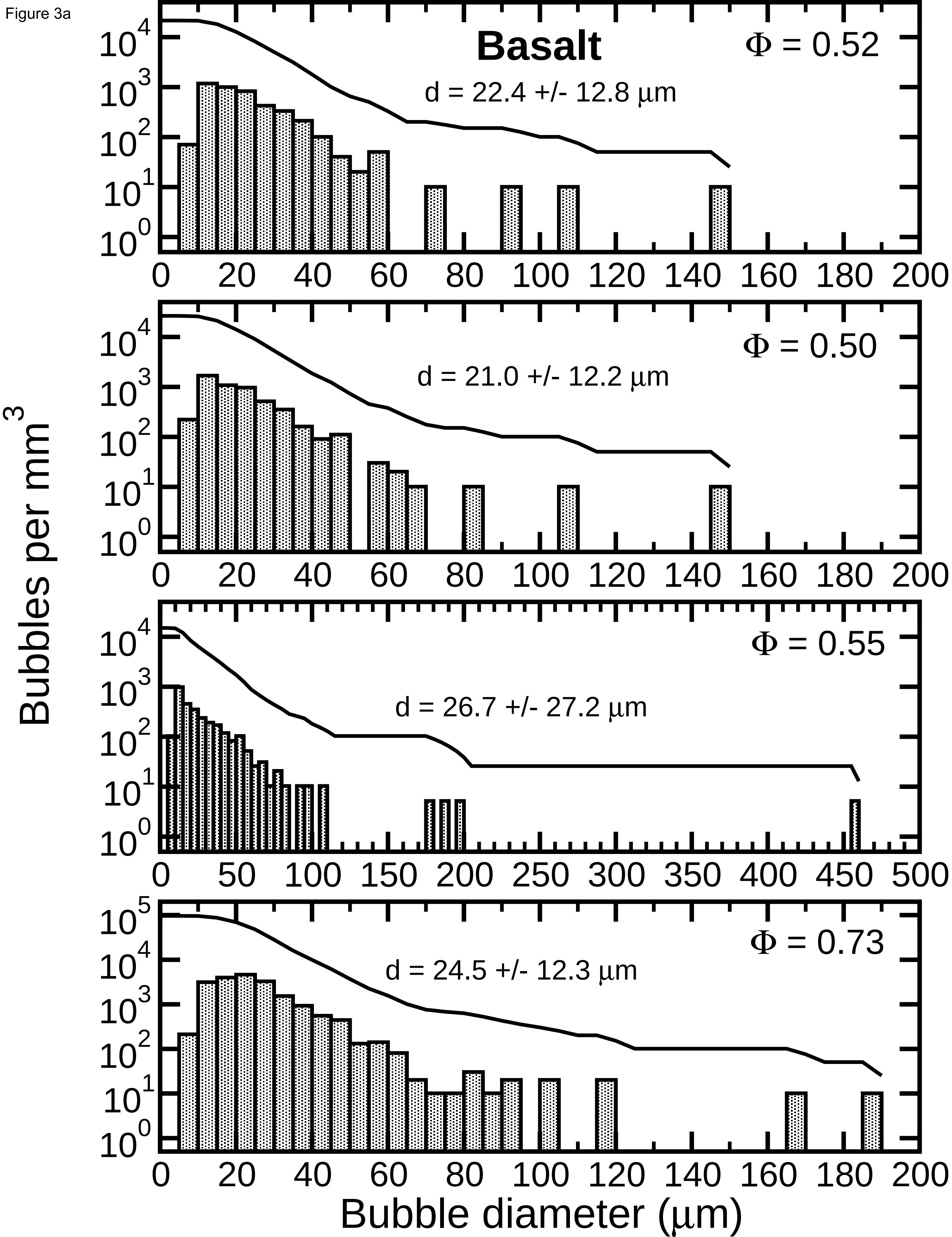
Basalt
Φ = 0.52
d = 22.4 +/- 12.8 μm
Φ = 0.50
d = 21.0 +/- 12.2 μm
Φ = 0.55
d = 26.7 +/- 27.2 μm
Φ = 0.73
d = 24.5 +/- 12.3 μm
Bubbles per mm3
Bubble diameter (μm)

Figure 3b

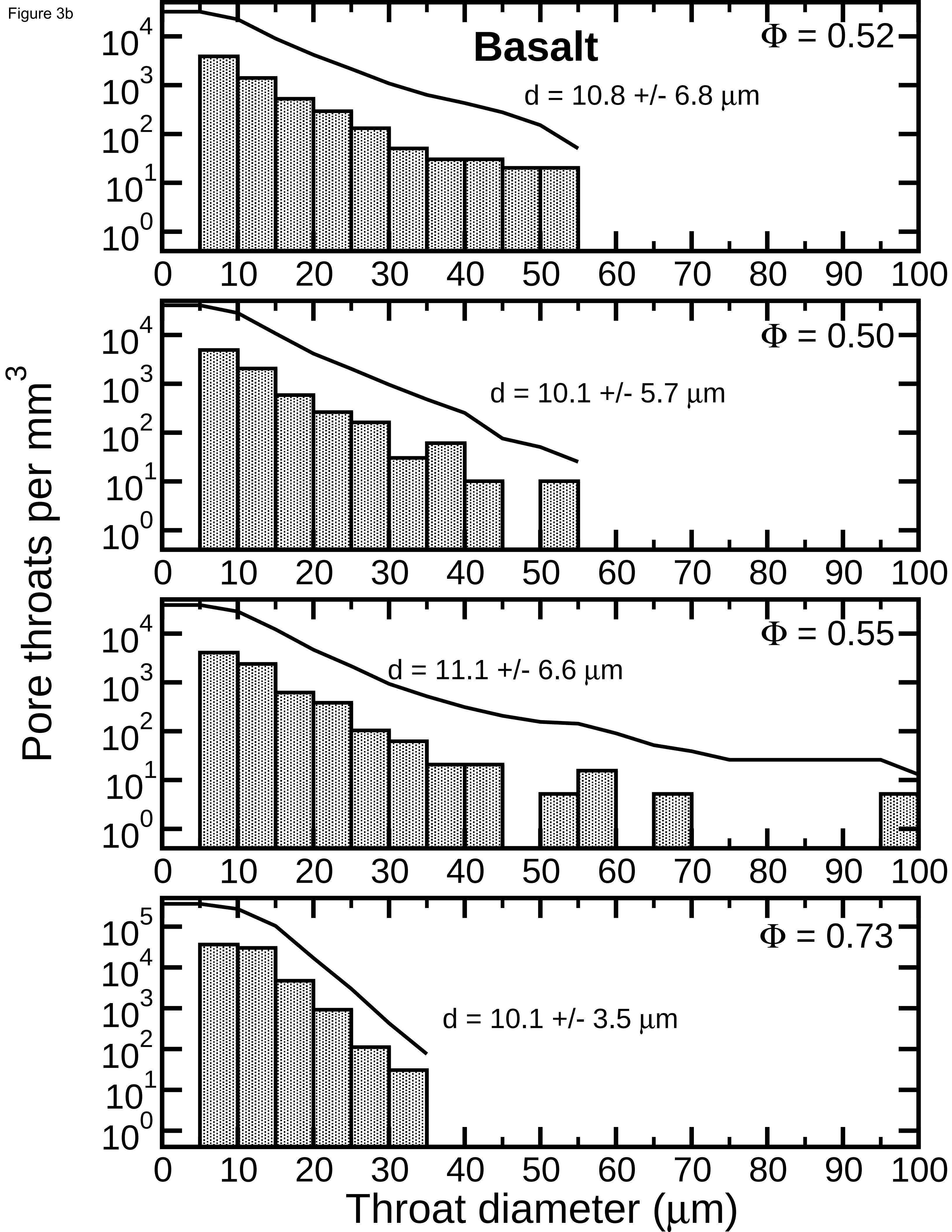
Basalt
Φ = 0.52
d = 10.8 +/- 6.8 µm
Φ = 0.50
d = 10.1 +/- 5.7 µm
Φ = 0.55
d = 11.1 +/- 6.6 µm
Φ = 0.73
d = 10.1 +/- 3.5 µm
Pore throats per mm3
Throat diameter (µm)

Figure 4a

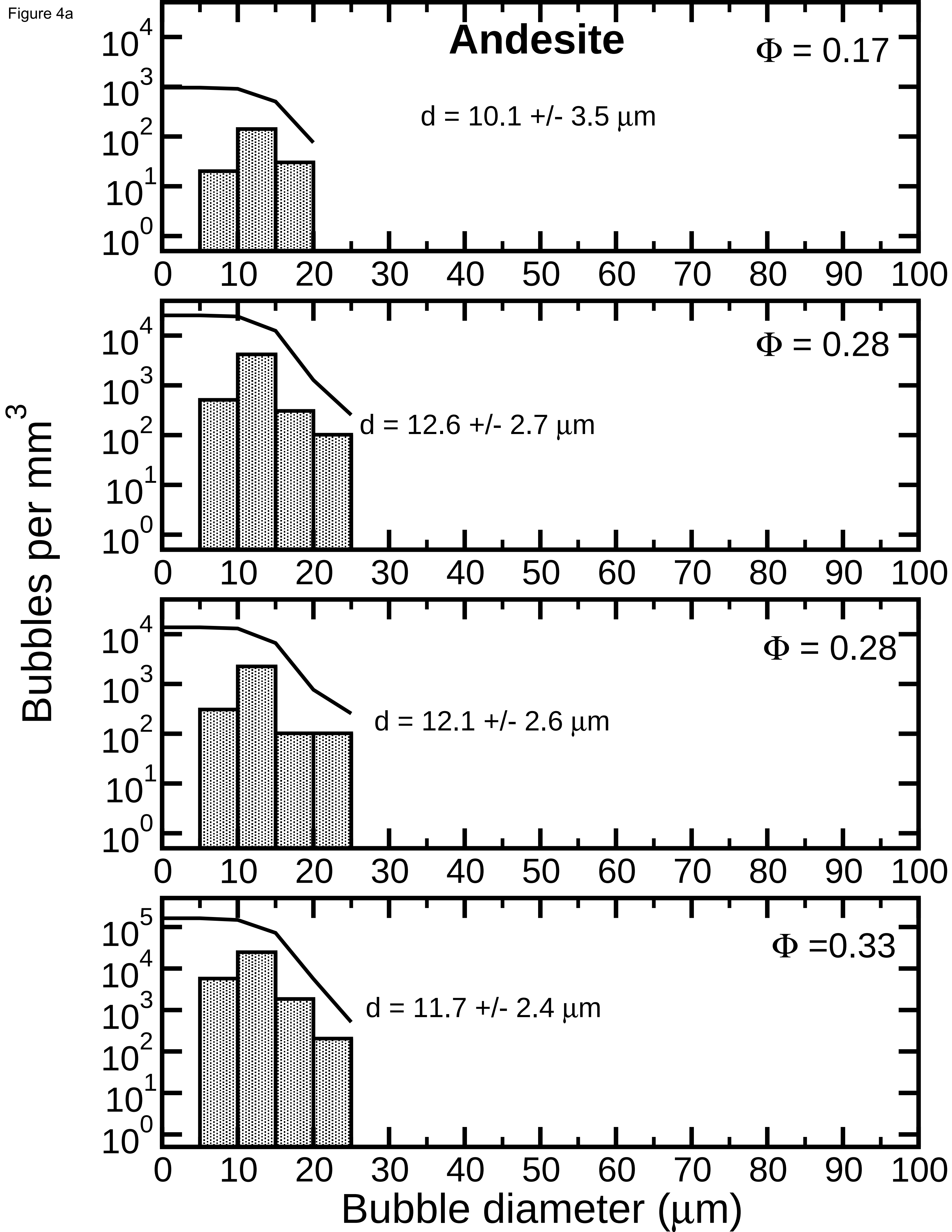

Andesite
Φ = 0.17
d = 10.1 +/- 3.5 μm
Φ = 0.28
d = 12.6 +/- 2.7 μm
Φ = 0.28
d = 12.1 +/- 2.6 μm
Φ =0.33
d = 11.7 +/- 2.4 μm
Bubbles per mm3
Bubble diameter (μm)

Figure 4b

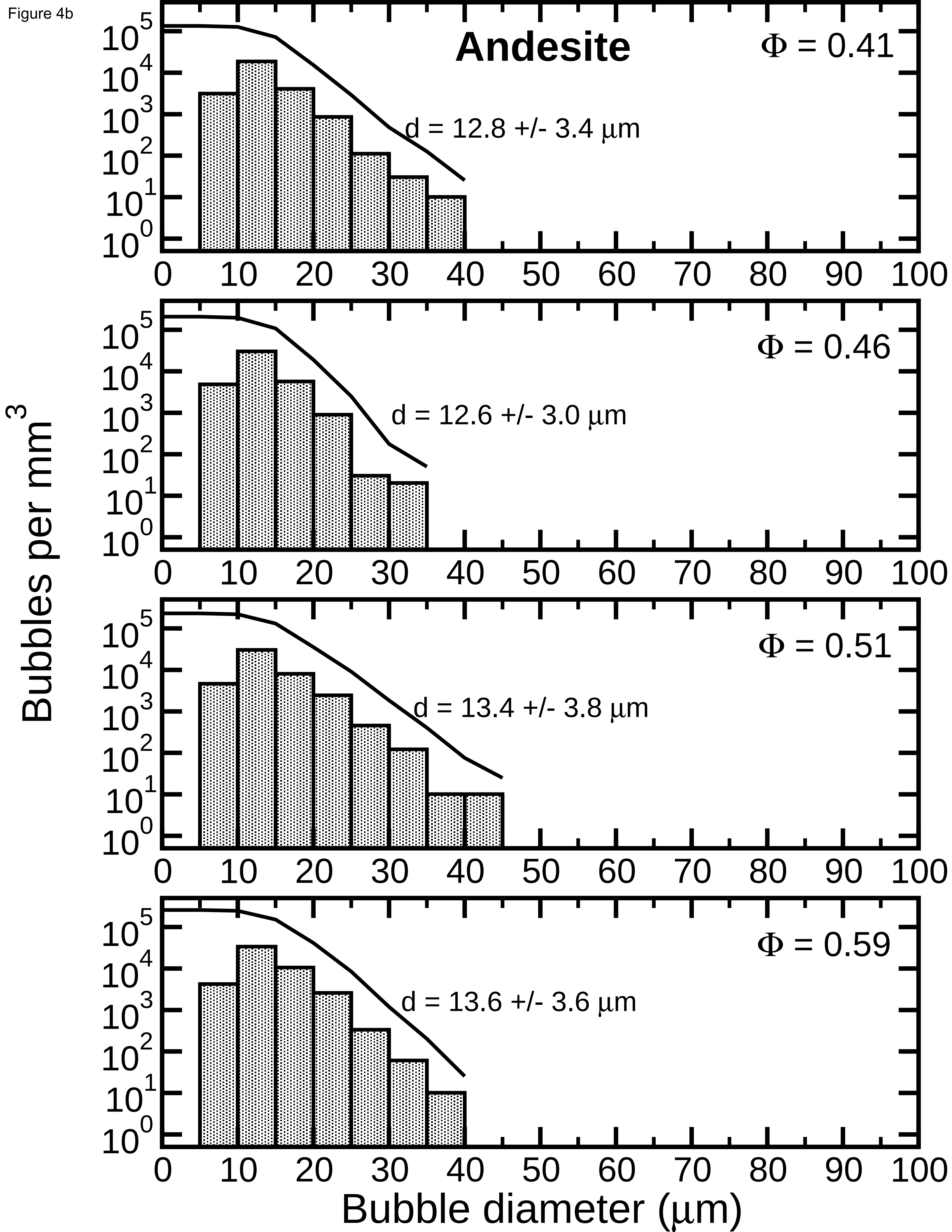

Andesite
Φ = 0.41
d = 12.8 +/- 3.4 μm
Φ = 0.46
d = 12.6 +/- 3.0 μm
Φ = 0.51
d = 13.4 +/- 3.8 μm
Φ = 0.59
d = 13.6 +/- 3.6 μm
Bubbles per mm3
Bubble diameter (μm)

Figure 4c

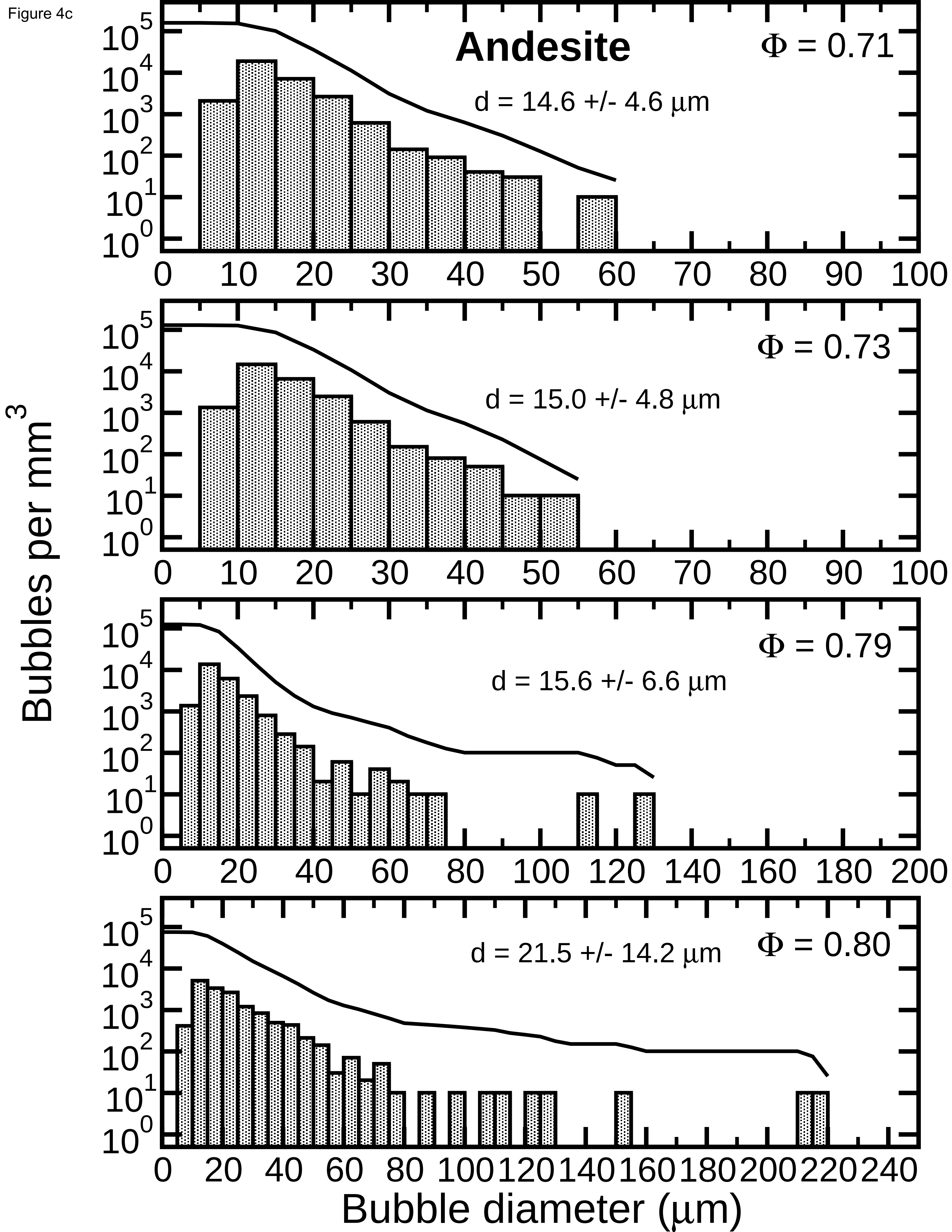

Andesite
Φ = 0.71
d = 14.6 +/- 4.6 μm
Φ = 0.73
d = 15.0 +/- 4.8 μm
Φ = 0.79
d = 15.6 +/- 6.6 μm
Φ = 0.80
d = 21.5 +/- 14.2 μm
Bubbles per mm3
Bubble diameter (μm)

Figure 4d

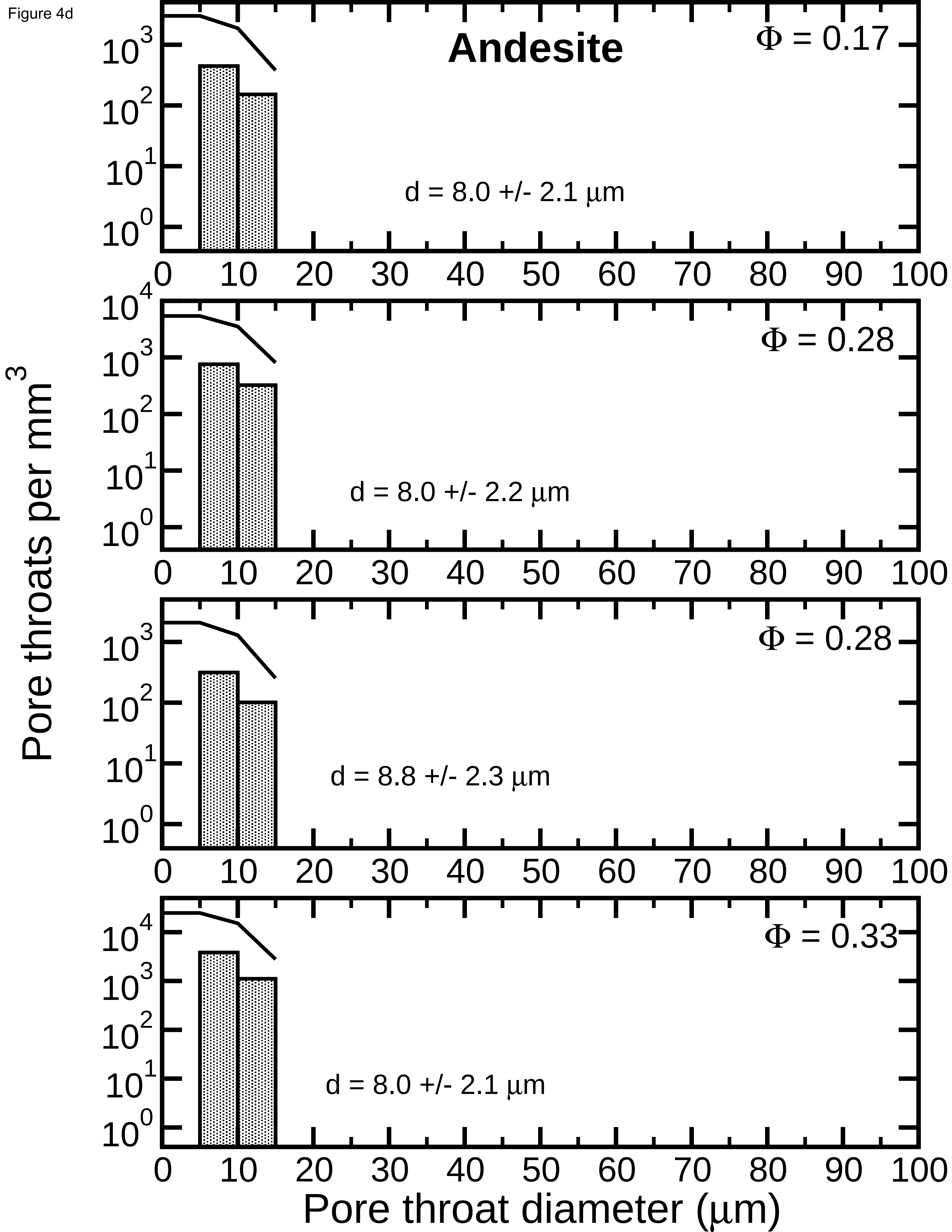

Andesite
Φ = 0.17
d = 8.0 +/- 2.1 μm
Φ = 0.28
d = 8.0 +/- 2.2 μm
Φ = 0.28
d = 8.8 +/- 2.3 μm
Φ = 0.33
d = 8.0 +/- 2.1 μm
Pore throats per mm3
Pore throat diameter (μm)
0 10 20 30 40 50 60 70 80 90 100
10^0 10^1 10^2 10^3 10^4

Figure 4e

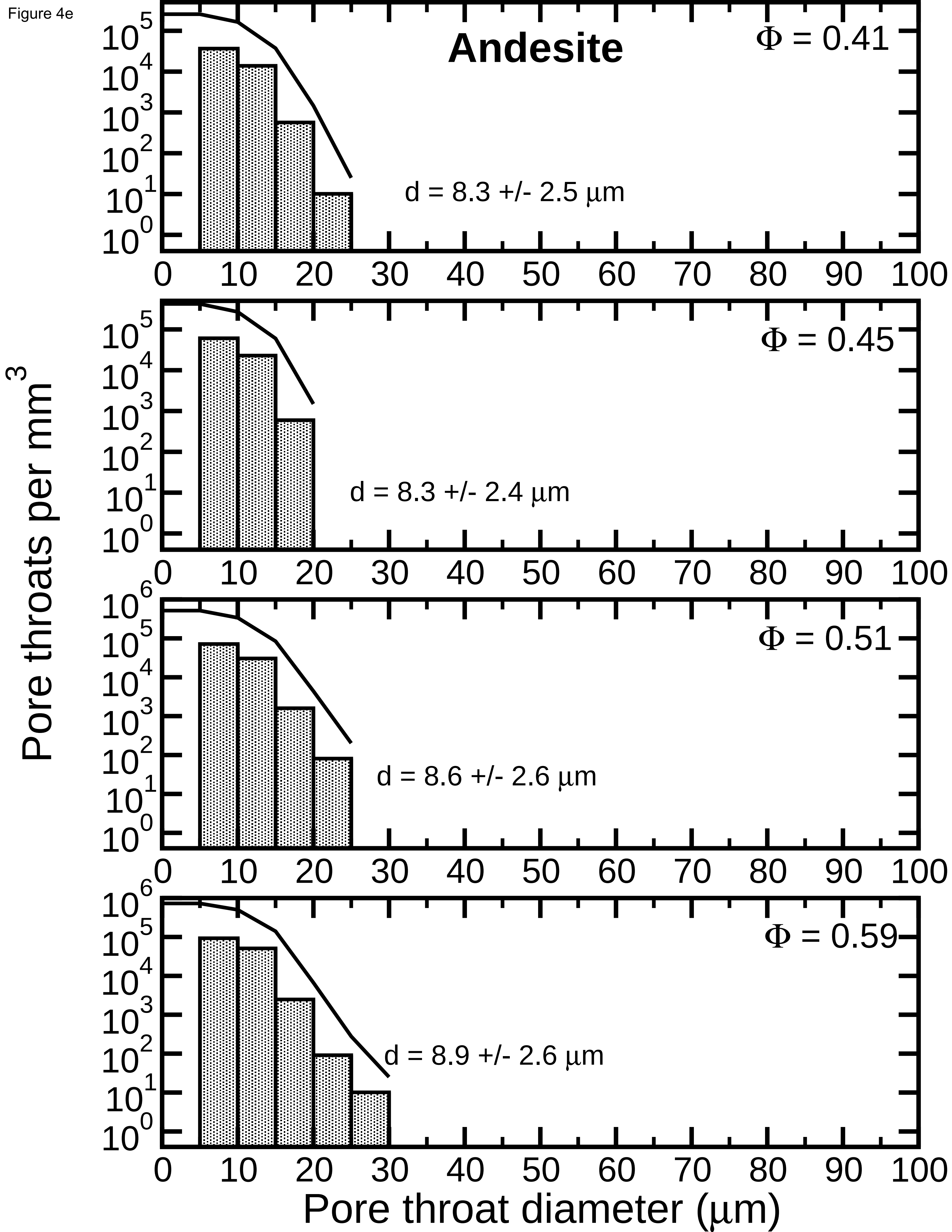

Andesite
Φ = 0.41
d = 8.3 +/- 2.5 μm
Φ = 0.45
d = 8.3 +/- 2.4 μm
Φ = 0.51
d = 8.6 +/- 2.6 μm
Φ = 0.59
d = 8.9 +/- 2.6 μm
Pore throats per mm3
Pore throat diameter (μm)

Figure 4f

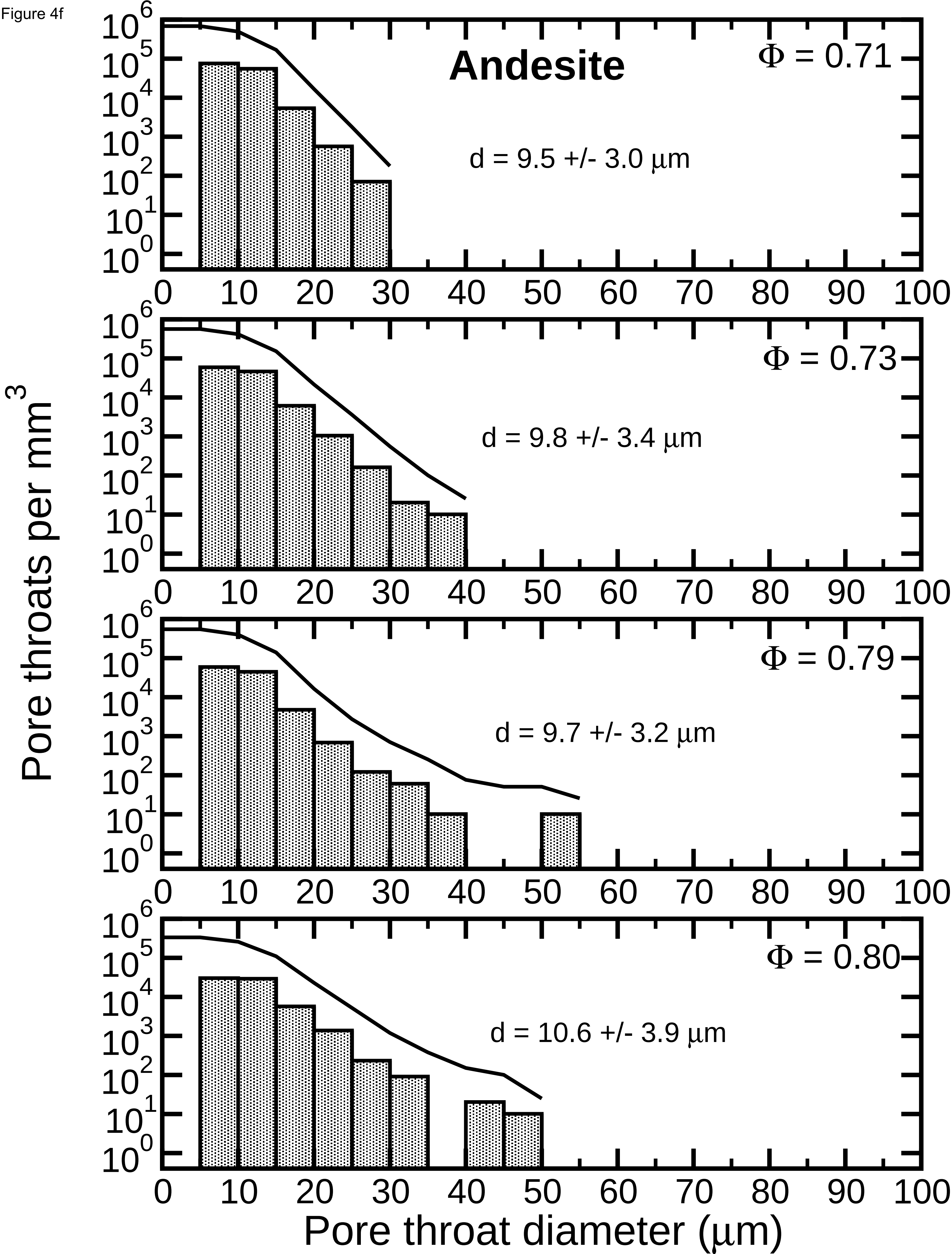
Andesite
Φ = 0.71
d = 9.5 +/- 3.0 μm
Φ = 0.73
d = 9.8 +/- 3.4 μm
Φ = 0.79
d = 9.7 +/- 3.2 μm
Φ = 0.80
d = 10.6 +/- 3.9 μm
Pore throats per mm3
Pore throat diameter (μm)
0 10 20 30 40 50 60 70 80 90 100
10^0 10^1 10^2 10^3 10^4 10^5 10^6

Figure 5a

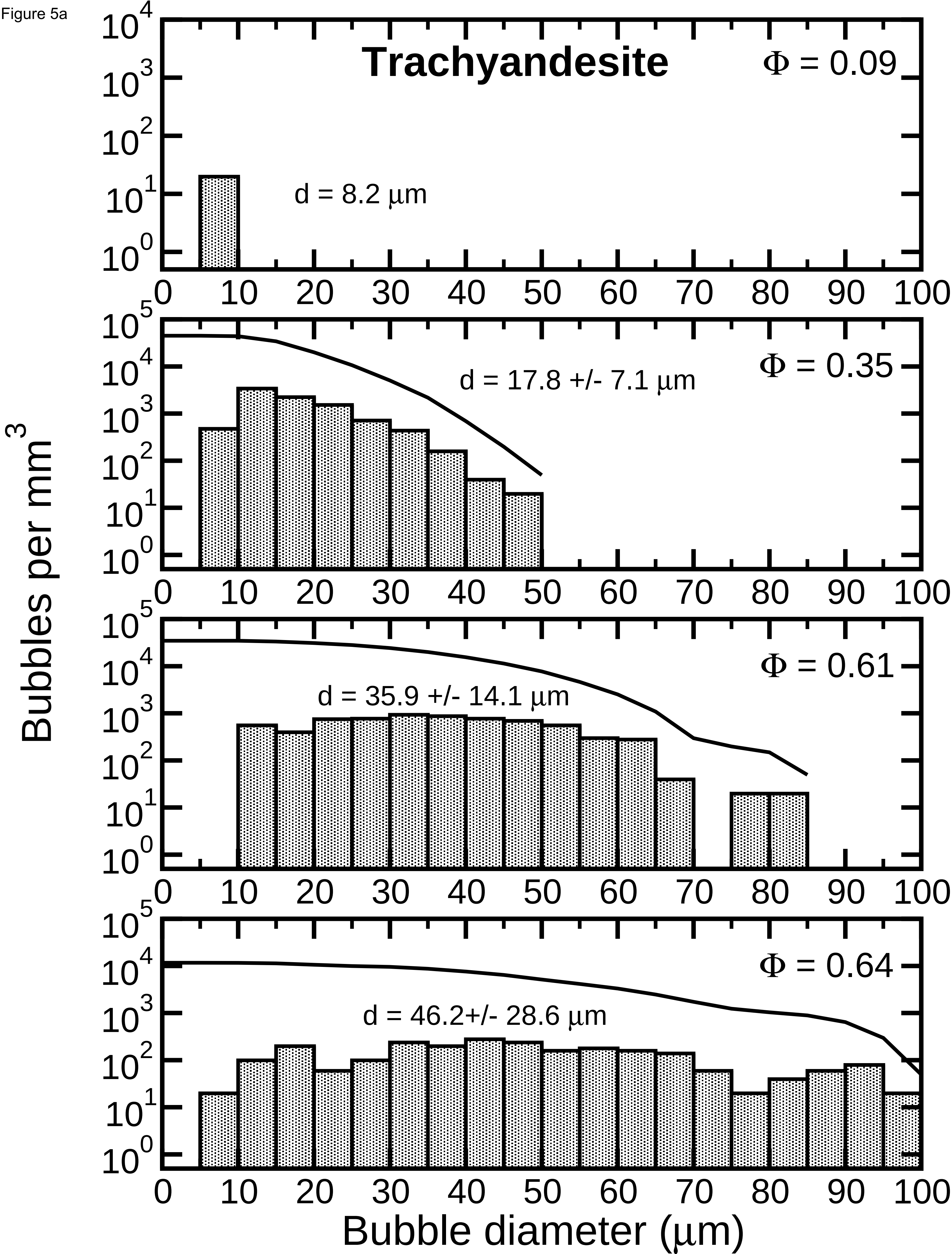

Trachyandesite
Φ = 0.09
d = 8.2 μm
Φ = 0.35
d = 17.8 +/- 7.1 μm
Φ = 0.61
d = 35.9 +/- 14.1 μm
Φ = 0.64
d = 46.2+/- 28.6 μm
Bubbles per mm3
Bubble diameter (μm)

Figure 5b

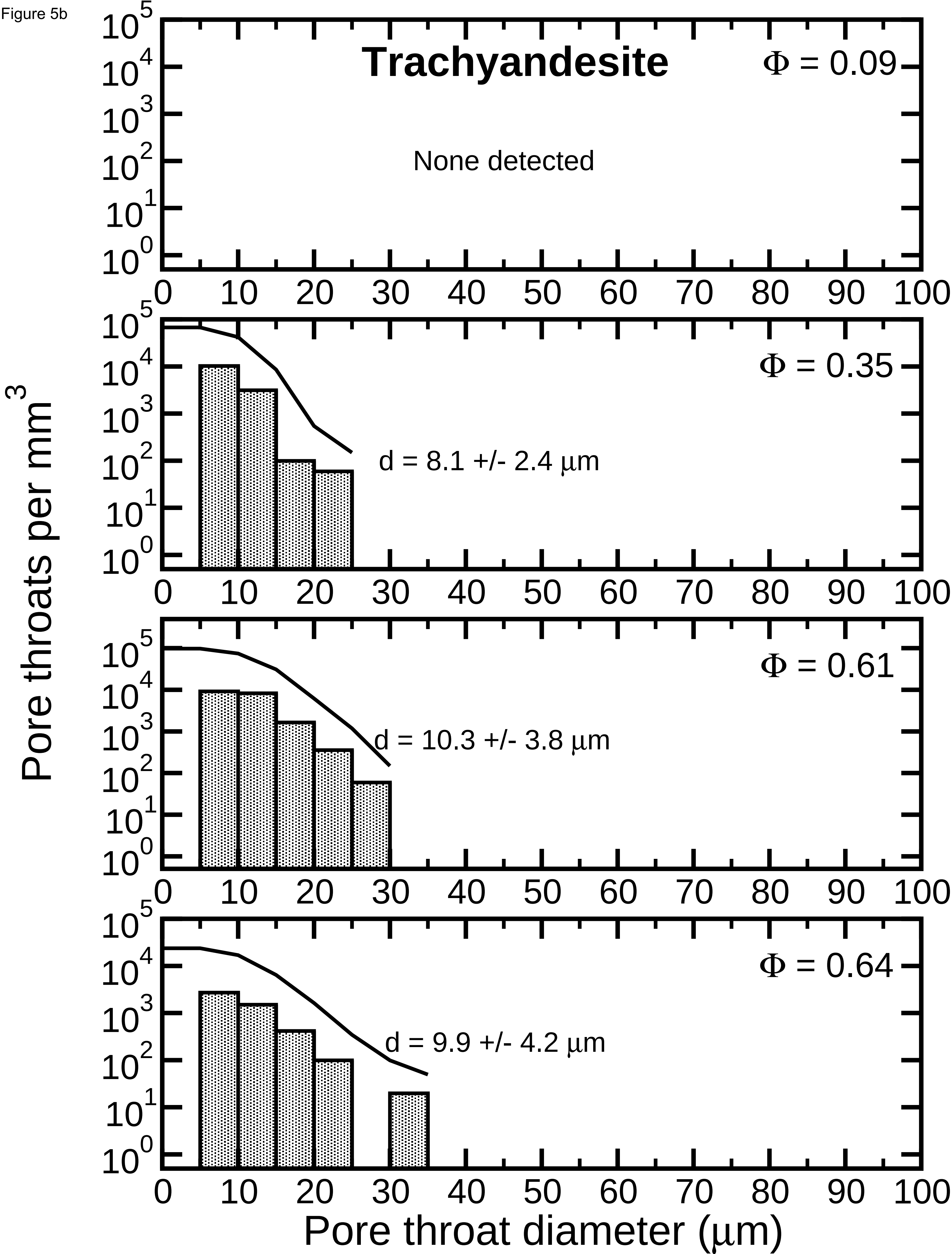
Trachyandesite
Φ = 0.09
None detected
Φ = 0.35
d = 8.1 +/- 2.4 µm
Φ = 0.61
d = 10.3 +/- 3.8 µm
Φ = 0.64
d = 9.9 +/- 4.2 µm
Pore throats per mm3
Pore throat diameter (µm)
10^0 10^1 10^2 10^3 10^4 10^5
0 10 20 30 40 50 60 70 80 90 100

Figure 6a

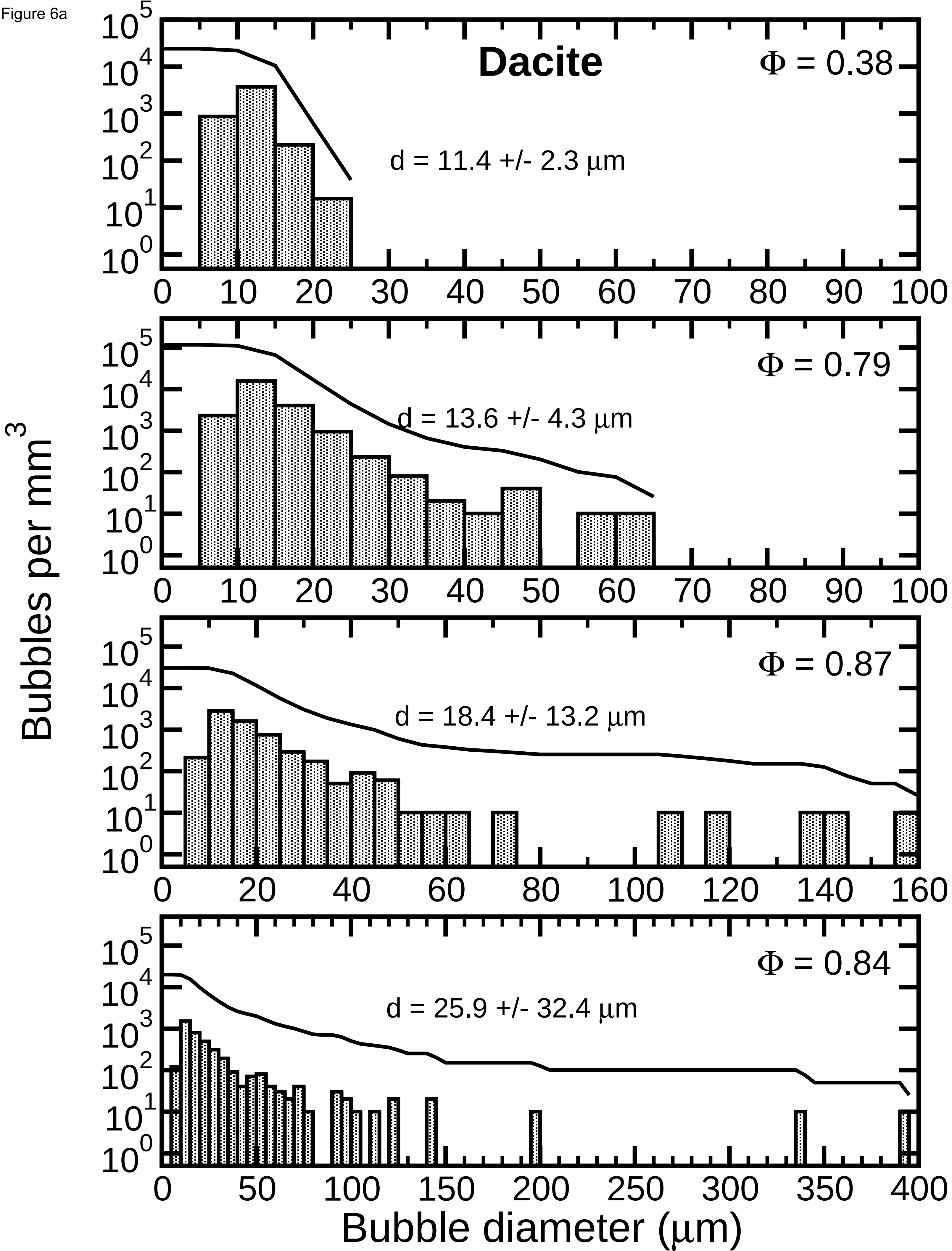

Dacite
Φ = 0.38
d = 11.4 +/- 2.3 μm
Φ = 0.79
d = 13.6 +/- 4.3 μm
Φ = 0.87
d = 18.4 +/- 13.2 μm
Φ = 0.84
d = 25.9 +/- 32.4 μm
Bubbles per mm3
Bubble diameter (μm)

Figure 6b

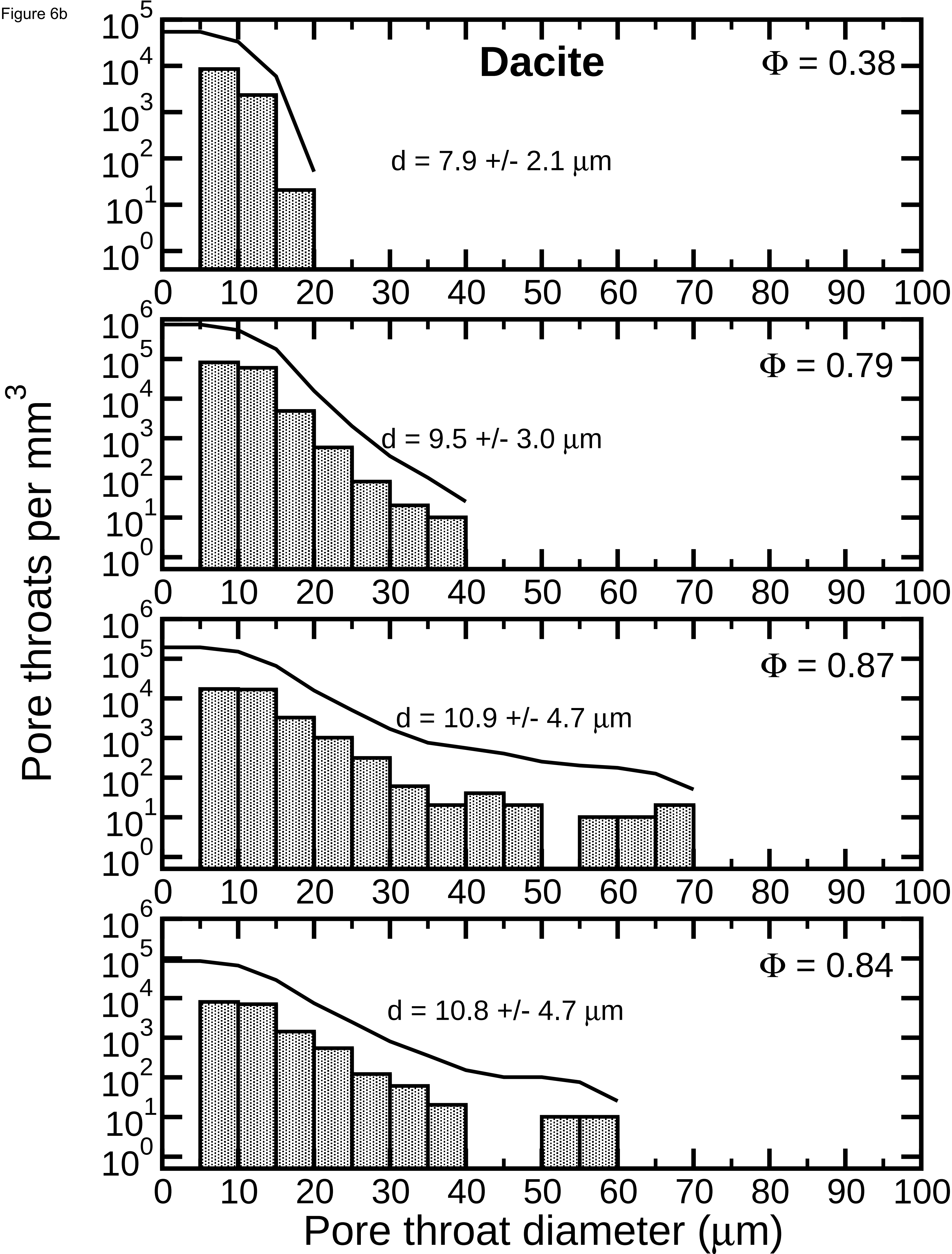

Dacite
Φ = 0.38
d = 7.9 +/- 2.1 μm
Φ = 0.79
d = 9.5 +/- 3.0 μm
Φ = 0.87
d = 10.9 +/- 4.7 μm
Φ = 0.84
d = 10.8 +/- 4.7 μm
Pore throats per mm3
Pore throat diameter (μm)

Figure 7

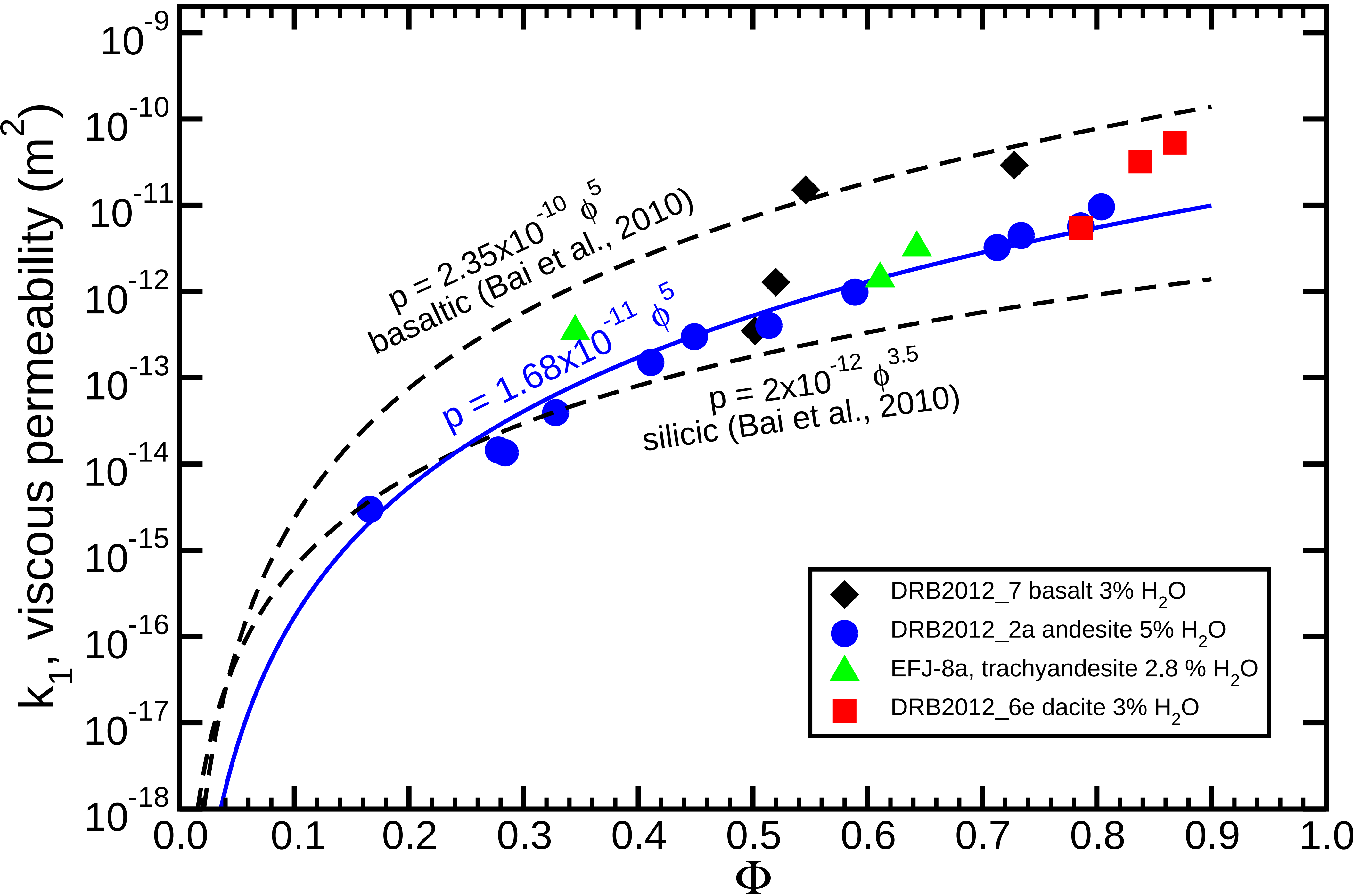

p = 2.35x10^-10 ϕ^5
basaltic (Bai et al., 2010)
p = 1.68x10^-11 ϕ^5
p = 2x10^-12 ϕ^3.5
silicic (Bai et al., 2010)
DRB2012_7 basalt 3% H2O
DRB2012_2a andesite 5% H2O
EFJ-8a, trachyandesite 2.8 % H2O
DRB2012_6e dacite 3% H2O
k1, viscous permeability (m2)
10^-9
10^-10
10^-11
10^-12
10^-13
10^-14
10^-15
10^-16
10^-17
10^-18
0.0
0.1
0.2
0.3
0.4
0.5
0.6
0.7
0.8
0.9
1.0
Φ

Figure 8

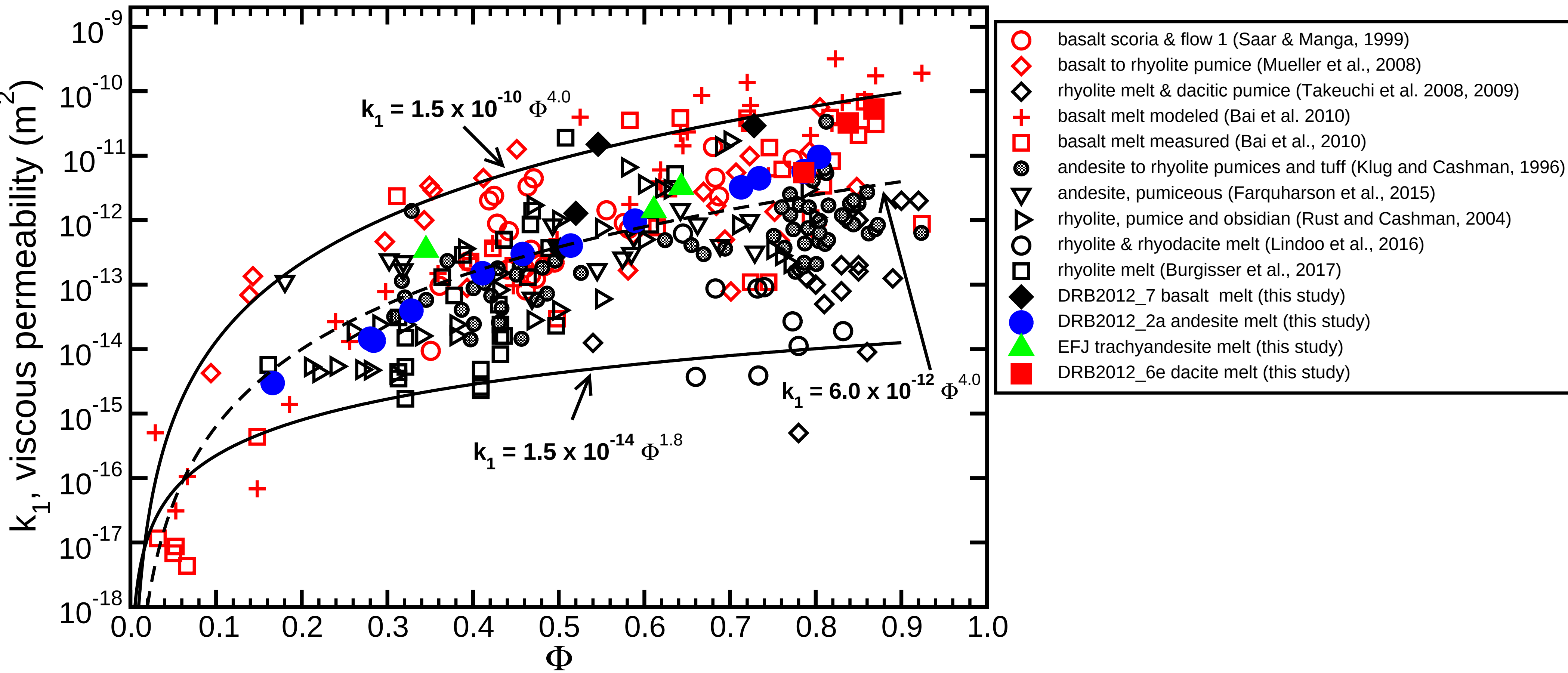

k1, viscous permeability (m2)
10-9
10-10
10-11
10-12
10-13
10-14
10-15
10-16
10-17
10-18
0.0
0.1
0.2
0.3
0.4
0.5
0.6
0.7
0.8
0.9
1.0
Φ
k1 = 1.5 x 10-10 Φ4.0
k1 = 6.0 x 10-12 Φ4.0
k1 = 1.5 x 10-14 Φ1.8
basalt scoria & flow 1 (Saar & Manga, 1999)
basalt to rhyolite pumice (Mueller et al., 2008)
rhyolite melt & dacitic pumice (Takeuchi et al. 2008, 2009)
basalt melt modeled (Bai et al. 2010)
basalt melt measured (Bai et al., 2010)
andesite to rhyolite pumices and tuff (Klug and Cashman, 1996)
andesite, pumiceous (Farquharson et al., 2015)
rhyolite, pumice and obsidian (Rust and Cashman, 2004)
rhyolite & rhyodacite melt (Lindoo et al., 2016)
rhyolite melt (Burgisser et al., 2017)
DRB2012_7 basalt melt (this study)
DRB2012_2a andesite melt (this study)
EFJ trachyandesite melt (this study)
DRB2012_6e dacite melt (this study)

Figure 9a

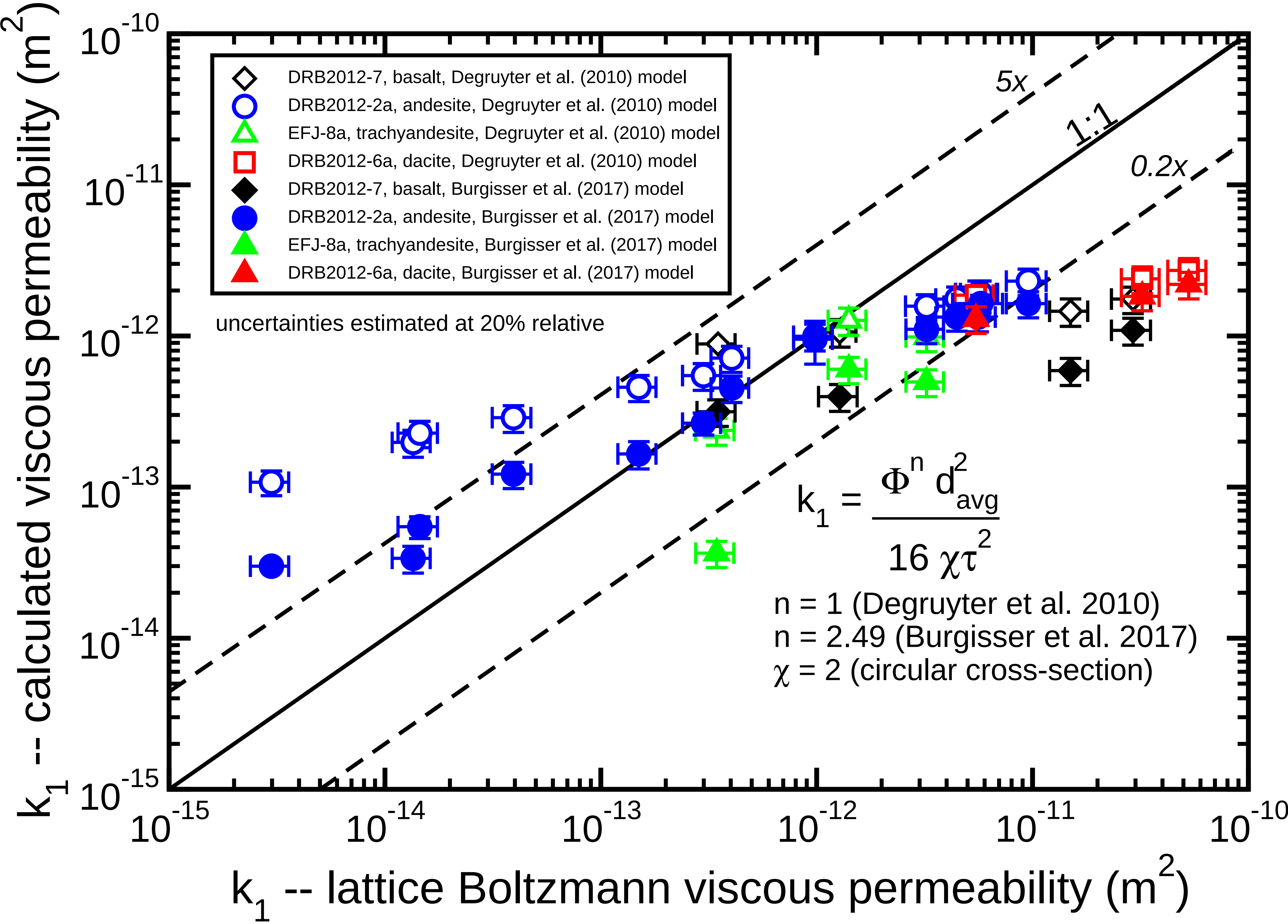

DRB2012-7, basalt, Degruyter et al. (2010) model
DRB2012-2a, andesite, Degruyter et al. (2010) model
EFJ-8a, trachyandesite, Degruyter et al. (2010) model
DRB2012-6a, dacite, Degruyter et al. (2010) model
DRB2012-7, basalt, Burgisser et al. (2017) model
DRB2012-2a, andesite, Burgisser et al. (2017) model
EFJ-8a, trachyandesite, Burgisser et al. (2017) model
DRB2012-6a, dacite, Burgisser et al. (2017) model
uncertainties estimated at 20% relative
5x
1:1
0.2x
$k_1 = \frac{\Phi^n d_{avg}^2}{16 \chi \tau^2}$
n = 1 (Degruyter et al. 2010)
n = 2.49 (Burgisser et al. 2017)
χ = 2 (circular cross-section)
k_1 -- calculated viscous permeability (m^2)
k_1 -- lattice Boltzmann viscous permeability (m^2)
10^{-15}
10^{-14}
10^{-13}
10^{-12}
10^{-11}
10^{-10}

Figure 9b

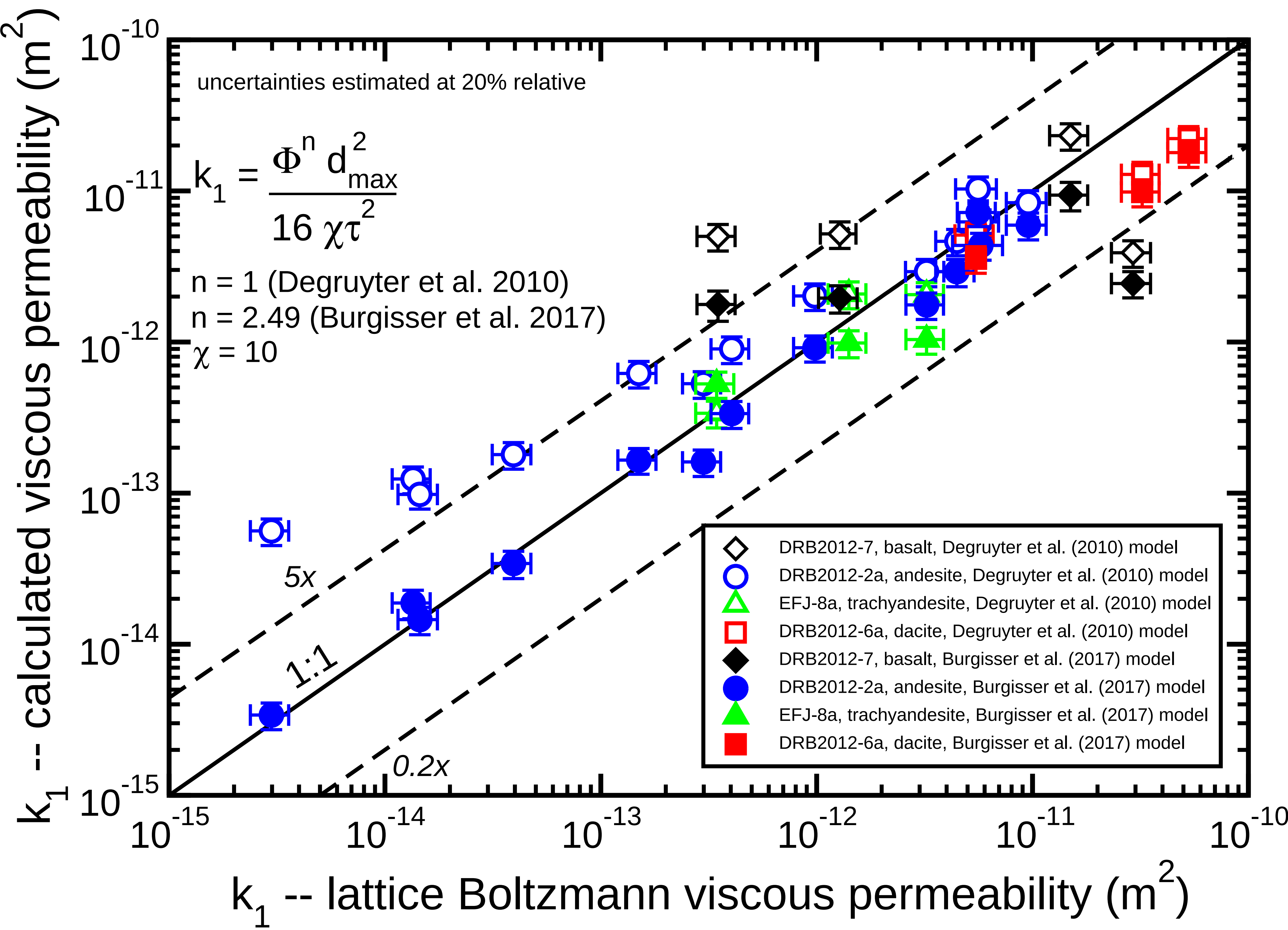

uncertainties estimated at 20% relative
$k_1 = \frac{\Phi^n d_{max}^2}{16\chi\tau^2}$
n = 1 (Degruyter et al. 2010)
n = 2.49 (Burgisser et al. 2017)
χ = 10
5x
1:1
0.2x
DRB2012-7, basalt, Degruyter et al. (2010) model
DRB2012-2a, andesite, Degruyter et al. (2010) model
EFJ-8a, trachyandesite, Degruyter et al. (2010) model
DRB2012-6a, dacite, Degruyter et al. (2010) model
DRB2012-7, basalt, Burgisser et al. (2017) model
DRB2012-2a, andesite, Burgisser et al. (2017) model
EFJ-8a, trachyandesite, Burgisser et al. (2017) model
DRB2012-6a, dacite, Burgisser et al. (2017) model
k_1 -- calculated viscous permeability (m^2)
k_1 -- lattice Boltzmann viscous permeability (m^2)
10^{-15}
10^{-14}
10^{-13}
10^{-12}
10^{-11}
10^{-10}

Figure 9c

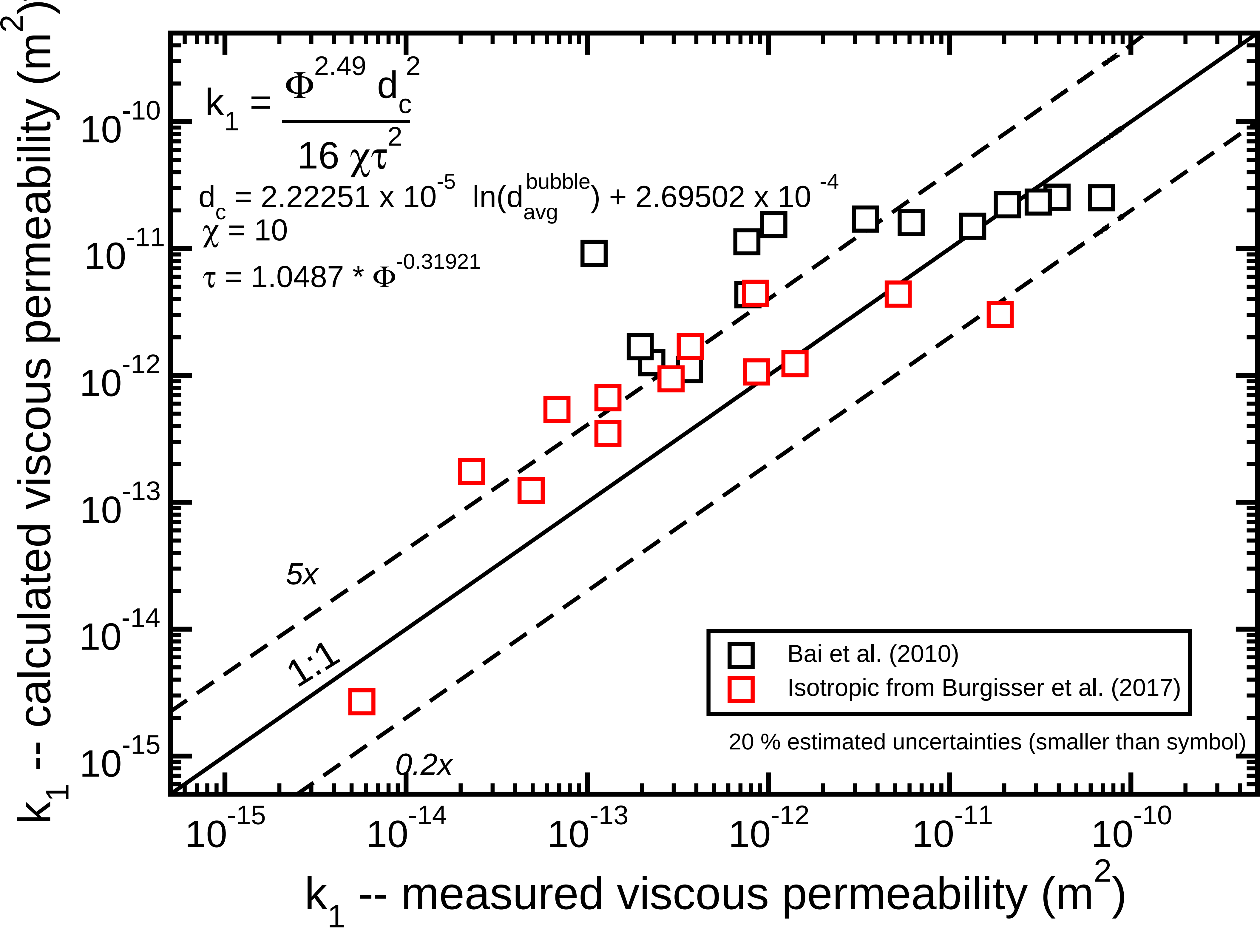

$k_1 = \frac{\Phi^{2.49} d_c^2}{16 \chi \tau^2}$
$d_c = 2.22251 \times 10^{-5} \ln(d^{bubble}_{avg}) + 2.69502 \times 10^{-4}$
$\chi = 10$
$\tau = 1.0487 * \Phi^{-0.31921}$
5x
1:1
0.2x
Bai et al. (2010)
Isotropic from Burgisser et al. (2017)
20 % estimated uncertainties (smaller than symbol)
10^{-10}
10^{-11}
10^{-12}
10^{-13}
10^{-14}
10^{-15}
k_1 -- calculated viscous permeability (m^2)
k_1 -- measured viscous permeability (m^2)

Table 1: Starting compositions

	MORB[1]	Andesite[2] AT-29	Trachyandesite[3] EFJ	Dacite[4] AT-150
SiO_2	49.7	56.8	58.5	64.1
TiO_2	1.41	1.01	1.55	0.61
Al_2O_3	16.1	16.9	14.6	16.4
FeO^{total}	10.3	8.03	9.35	5.19
MnO	0.17	0.17	0.24	
MgO	7.8	3.09	2.97	2.00
CaO	10.8	7.05	4.84	4.78
Na_2O	2.65	3.99	5.19	4.45
K_2O	0.1	2.05	1.83	1.98
P_2O_5	0.11	0.28	0.47	
Total	99.14	99.37	99.52	99.51
H_2O	2.9	5.0	2.8	3.0
Viscosity (Pa s)[5]	14/234	32/6685	115/7505	359/61126

[1]Fortin et al. (2015)
[2]AT-29 from Baker and Eggler (1987)
[3]Average of compositions in LaRue, M.Sc. Thesis (2012)
[4]Liu et al. (2007)
[5]1100 °C melt viscosity at the initial water concentration followed by viscosity in the anhdyrous melt calculated following Giordano et al. (2008)

Table 1: Starting compositions

	MORB[1]	Andesite[2] AT-29	Trachyandesite[3] EFJ
SiO_2	49.7	56.8	58.5
TiO_2	1.41	1.01	1.55
Al_2O_3	16.1	16.9	14.6
FeO^{total}	10.3	8.03	9.35
MnO	0.17	0.17	0.24
MgO	7.8	3.09	2.97
CaO	10.8	7.05	4.84
Na_2O	2.65	3.99	5.19
K_2O	0.1	2.05	1.83
P_2O_5	0.11	0.28	0.47
Total	99.14	99.37	99.52
H_2O	2.9	5.0	2.8
Viscosity (Pa s)[5]	14/234	32/6685	115/7505

[1]Fortin et al. (2015)
[2]AT-29 from Baker and Eggler (1987)
[3]Average of compositions in LaRue, M.Sc. Thesis (2012)
[4]Liu et al. (2007)
[5]1100 °C melt viscosity at the initial water concentration followed by viscosity in the anhdyrous melt calculated following Giordano et al. (2008)

Dacite[4]
AT-150
64.1
0.61
16.4
5.19
2.00
4.78
4.45
1.98
99.51
3.0
359/61126

/

Table 2 for easy reading

Table 2: Results of bubble growth experiments

Sample	Volume[1] (mm^3)	Porosity[2]	Connected Porosity[2]	BND[3] (mm^{-3})	PTD[4] (mm^{-3})	PTD/BND[5]	Average bubble diameter (m)	Median bubble diameter (m)	Average throat diameter (m)	Median throat diameter (m)	Maximum throat diameter (m)	β[6] (mm^{-3})	Tortuosity	Coordination #	Permeability (m^2)	Vesiculation conditions[7]
Basalt, 3 % H_2O, ΔP = 68 MPa[8]																
DRB2012-07a-2	0.0989	0.52	0.52	4309	6403	1.486	2.24×10^{-5}	1.92×10^{-5}	1.08×10^{-5}	8.2×10^{-6}	5.36×10^{-5}	2.10×10^{3}	1.33 ± 0.10	4.4 ± 6.8	1.28×10^{-12}	Manual heating to 970 °C, hold 75 s, 1st bubbles: 616 °C
DRB2012-07a-3	0.0989	0.50	0.50	5290	8092	1.530	2.10×10^{-5}	1.73×10^{-5}	1.01×10^{-5}	8.2×10^{-6}	5.36×10^{-5}	2.81×10^{3}	1.34 ± 0.10	4.3 ± 7.1	3.49×10^{-13}	Re-heating of DRB 2012-07a-2, quenched
DRB2012-7f-10	0.1931	0.55	0.55	3009	7706	2.561	2.67×10^{-5}	1.91×10^{-5}	1.11×10^{-5}	8.2×10^{-6}	9.89×10^{-5}	4.70×10^{3}	1.20 ± 0.07	5.2 ± 6.8	1.50×10^{-11}	1 °C s^{-1} from 600 to 1150, hold 150 s, 1st vesiculation: 740 °C
DRB2012-7c-f	0.0989	0.73	0.73	19228	72157	3.753	2.45×10^{-5}	2.31×10^{-5}	1.01×10^{-5}	8.2×10^{-6}	3.37×10^{-5}	5.29×10^{4}	1.15 ± 0.08	6.8 ± 6.2	2.92×10^{-11}	6 °C s^{-1} from 600 to 1150, hold 40 s, 1st vesiculation: 880 °C
Trachyandesite, 2.8 % H_2O, ΔP =35 MPa																0.8 °C s^{-1} from 600 to 950, hold 150 s, 1st vesiculation: 720 °C
EFJ-8a-06	0.0506	0.09	0.04	20	0	0.000	8.20×10^{-6}					0	n.d.	not connected	4.23×10^{-16}	325 s, 860 °C (1 bubble found)
EFJ-8a-07	0.0506	0.35	0.33	8989	13493	1.501	1.78×10^{-5}	1.73×10^{-5}	8.10×10^{-6}	8.2×10^{-6}	2.16×10^{-5}	4.52×10^{3}	1.57 ± 0.23	3.8 ± 1.4	3.44×10^{-13}	413 s, 930 °C
EFJ-8a-08	0.0506	0.61	0.61	6934	19419	2.801	3.59×10^{-5}	3.56×10^{-5}	1.03×10^{-5}	1.00×10^{-5}	2.95×10^{-5}	1.25×10^{4}	1.26 ± 0.06	5.2 ± 2.2	1.41×10^{-12}	380 s, 980 °C
EFJ-8a-09	0.0506	0.64	0.64	2331	4741	2.034	4.62×10^{-5}	4.44×10^{-5}	9.90×10^{-6}	8.2×10^{-6}	3.20×10^{-5}	2.43×10^{3}	1.40 ± 0.12	3.9 ± 1.1	3.23×10^{-12}	471 s, 950 °C
Andesite, 5 % H_2O, ΔP = 168 MPa																5 °C s^{-1} from 600 to 1100, hold 15 s, 1st vesiculation: 900 °C
DRB2012-2a-01	0.0989	0.17	0.15	233	597	2.565	1.01×10^{-5}	1.16×10^{-5}	8.00×10^{-6}	8.2×10^{-6}	1.29×10^{-5}	3.74×10^{2}	1.68 ± 0.20	4.0 ± 2.3	2.98×10^{-15}	60s, 900 °C
DRB2012-2a-08	0.0989	0.28	0.28	506	1082	2.140	1.26×10^{-5}	1.29×10^{-5}	8.00×10^{-6}	8.2×10^{-6}	1.42×10^{-5}	5.86×10^{2}	1.69 ± 0.50	4.1 ± 3.4	1.35×10^{-14}	77 s, 984 °C
DRB2012-2a-09	0.0989	0.28	0.28	273	415	1.519	1.21×10^{-5}	1.16×10^{-5}	8.80×10^{-6}	8.2×10^{-6}	1.29×10^{-5}	1.51×10^{3}	1.72 ± 0.51	3.8 ± 1.0	1.45×10^{-14}	79 s, 994 °C
DRB2012-2a-10	0.0989	0.33	0.33	3216	4956	1.541	1.17×10^{-5}	1.16×10^{-5}	8.00×10^{-6}	8.2×10^{-6}	1.42×10^{-5}	1.75×10^{3}	1.51 ± 0.35	3.6 ± 1.4	3.94×10^{-14}	81 s, 1005 °C
DRB2012-2a-11	0.0989	0.41	0.41	26915	50876	1.890	1.28×10^{-5}	1.29×10^{-5}	8.30×10^{-6}	8.2×10^{-6}	2.16×10^{-5}	2.40×10^{4}	1.39 ± 0.25	4.0 ± 2.4	1.50×10^{-13}	83 s, 1016 °C
DRB2012-2a-12	0.0989	0.46	0.46	41601	83971	2.018	1.26×10^{-5}	1.29×10^{-5}	8.30×10^{-6}	8.2×10^{-6}	1.83×10^{-5}	4.24×10^{4}	1.33 ± 0.22	4.2 ± 3.1	2.99×10^{-13}	85 s, 1026 °C
DRB2012-2a-13	0.0989	0.51	0.51	46112	103381	2.242	1.34×10^{-5}	1.29×10^{-5}	8.60×10^{-6}	8.2×10^{-6}	2.16×10^{-5}	5.73×10^{4}	1.29 ± 0.20	4.4 ± 3.8	4.04×10^{-13}	87 s, 1037 °C
DRB2012-2a-14	0.0989	0.59	0.59	51453	145761	2.833	1.36×10^{-5}	1.29×10^{-5}	8.90×10^{-6}	8.2×10^{-6}	2.83×10^{-5}	9.43×10^{4}	1.21 ± 0.13	5.2 ± 7.8	9.82×10^{-13}	89 s, 1047 °C
DRB2012-2a-15	0.0989	0.71	0.71	31841	136324	4.281	1.46×10^{-5}	1.29×10^{-5}	9.50×10^{-6}	8.2×10^{-6}	2.89×10^{-5}	1.05×10^{5}	1.13 ± 0.07	5.5 ± 12.3	3.23×10^{-12}	92 s, 1057 °C
DRB2012-2a-16	0.0989	0.73	0.74	26035	112797	4.333	1.40×10^{-5}	1.35×10^{-5}	9.80×10^{-6}	8.2×10^{-6}	3.56×10^{-5}	8.68×10^{4}	1.12 ± 0.06	5.2 ± 7.1	4.46×10^{-12}	94 s, 1168 °C
DRB2012-2a-17	0.0989	0.79	0.79	25003	109611	4.384	1.56×10^{-5}	1.42×10^{-5}	9.70×10^{-6}	8.2×10^{-6}	5.04×10^{-5}	8.46×10^{4}	1.10 ± 0.05	6.3 ± 12.7	5.60×10^{-12}	96 s, 1179 °C
DRB2012-2a-18	0.0989	0.79	0.79	22768	102774	4.514	1.65×10^{-5}	1.42×10^{-5}	9.87×10^{-6}	8.2×10^{-6}	3.92×10^{-5}	8.00×10^{4}	1.10 ± 0.05	6.8 ± 12.7	5.76×10^{-12}	98 s, 1089 °C
DRB2012-2a-19	0.0989	0.80	0.80	15131	66847	4.418	2.14×10^{-5}	1.73×10^{-5}	1.06×10^{-5}	1.00×10^{-5}	4.51×10^{-5}	5.17×10^{4}	1.10 ± 0.04	7.7 ± 12.7	9.56×10^{-12}	100 s, 1100 °C
Dacite, 3 % H_2O, ΔP = 74 MPa																1 °C s^{-1} from 600 to 1150, hold 150 s, 1st vesiculation: 790 °C
DRB2012-6e-7	0.1931	0.37	0.37	4806	10891	2.266	1.14×10^{-5}	1.16×10^{-5}	7.9×10^{-6}	8.2×10^{-6}	1.64×10^{-5}	6.09×10^{3}	1.48 ± 0.31	4.5 ± 6.8	no results	373 s, 980 °C
DRB2012-6e-8	0.0989	0.79	0.79	23344	147612	6.323	1.36×10^{-5}	1.29×10^{-5}	9.5×10^{-6}	8.2×10^{-6}	3.52×10^{-5}	1.24×10^{5}	1.09 ± 0.06	4.7 ± 4.6	5.47×10^{-12}	446 s, 1050 °C
DRB2012-6e-9	0.0989	0.87	0.87	6160	38688	6.281	1.84×10^{-5}	1.64×10^{-5}	1.09×10^{-5}	1.00×10^{-5}	6.96×10^{-5}	3.25×10^{4}	1.09 ± 0.03	4.7 ± 5.6	5.29×10^{-11}	504 s, 1110 °C
DRB2012-6e-10	0.0989	0.84	0.84	4015	17205	4.285	2.59×10^{-5}	1.73×10^{-5}	1.08×10^{-5}	1.00×10^{-5}	5.60×10^{-5}	1.32×10^{4}	1.13 ± 0.03	7.0 ± 11.5	3.22×10^{-11}	585 s, ~1200 °C

[1]Volume used for all analyses

[2]Porosities and connected porosity in these columns were determined on the volumes used for permeability measurements. See text for discussion

[3]Bubble number density (BND)

[4]Pore throat density (PTD)

[5]Pore throat density (PTD) divided by bubble number density

[6]β, or connective density, is defined in Equation 1

[7]Time-temperature histories and heating rates for experiments EFJ-8a, DRB2012-2a, and DRB2012-6e were extracted from time-temperature charts recorded during the experiments.
Time is in seconds after heating above 600 °C. Precision of time is within ~ 2 s and of temperature within ~10 °C, although temperature fluctuations as great as ± 50 °C were sometimes observed (DRB2012-6e-10)

[8]Supersaturation pressure at start of experiment calculated using Papale et al. (2006) as implemented on http://melts.ofm-research.org/CORBA_CTserver/Papale/Papale.php

Table 2 .xls format

Table 2: Results of bubble growth experiments

Sample	Volume[1] (mm^3)	Porosity[2]	Connected Porosity[2]	BND[3] (mm^{-3})	PTD[4] (mm^{-3})
Basalt, 3 % H_2O, ΔP = 68 MPa [8]					
DRB2012-07a-2	0.0989	0.52	0.52	4309	6403
DRB2012-07a-3	0.0989	0.50	0.50	5290	8092
DRB2012-7f-10	0.1931	0.55	0.55	3009	7706
DRB2012-7c-f	0.0989	0.73	0.73	19228	72157
Trachyandesite, 2.8 % H_2O, ΔP =35 MPa					
EFJ-8a-06	0.0506	0.09	0.04	20	0
EFJ-8a-07	0.0506	0.35	0.33	8989	13493
EFJ-8a-08	0.0506	0.61	0.61	6934	19419
EFJ-8a-09	0.0506	0.64	0.64	2331	4741
Andesite, 5 % H_2O, ΔP = 168 MPa					
DRB2012-2a-01	0.0989	0.17	0.15	233	597
DRB2012-2a-08	0.0989	0.28	0.28	506	1082
DRB2012-2a-09	0.0989	0.28	0.28	273	415
DRB2012-2a-10	0.0989	0.33	0.33	3216	4956
DRB2012-2a-11	0.0989	0.41	0.41	26915	50876
DRB2012-2a-12	0.0989	0.46	0.46	41601	83971
DRB2012-2a-13	0.0989	0.51	0.51	46112	103381
DRB2012-2a-14	0.0989	0.59	0.59	51453	145761
DRB2012-2a-15	0.0989	0.71	0.71	31841	136324
DRB2012-2a-16	0.0989	0.73	0.74	26035	112797
DRB2012-2a-17	0.0989	0.79	0.79	25003	109611
DRB2012-2a-18	0.0989	0.79	0.79	22768	102774
DRB2012-2a-19	0.0989	0.80	0.80	15131	66847

Dacite, 3 % H_2O, ΔP = 74 MPa					
DRB2012-6e-7	0.1931	0.37	0.37	4806	10891
DRB2012-6e-8	0.0989	0.79	0.79	23344	147612
DRB2012-6e-9	0.0989	0.87	0.87	6160	38688
DRB2012-6e-10	0.0989	0.84	0.84	4015	17205

[1]Volume used for all analyses

[2]Porosities and connected porosity in these columns were determined on the volumes used for permeabil

[3]Bubble number density (BND)

[4]Pore throat density (PTD)

[5]Pore throat density (PTD) divided by bubble number density

[6]β, or connective density, is defined in Equation 1

[7]Time-temperature histories and heating rates for experiments EFJ-8a, DRB2012-2a, and DRB2012-6e w
Time is in seconds after heating above 600 °C. Precision of time is within ~ 2 s and of temperature with

[8]Supersaturation pressure at start of experiment calculated using Papale et al. (2006) as implemented on

PTD/BND[5]	Average bubble diameter (m)	Median bubble diameter (m)	Average throat diameter (m)	Median throat diameter (m)	Maximum throat diameter (m)	β^6 (mm^{-3})	Tortuosity
1.486	2.24×10^{-5}	1.92×10^{-5}	1.08×10^{-5}	8.2×10^{-6}	5.36×10^{-5}	2.10×10^{3}	1.33 ± 0.10
1.530	2.10×10^{-5}	1.73×10^{-5}	1.01×10^{-5}	8.2×10^{-6}	5.36×10^{-5}	2.81×10^{3}	1.34 ± 0.10
2.561	2.67×10^{-5}	1.91×10^{-5}	1.11×10^{-5}	8.2×10^{-6}	9.89×10^{-5}	4.70×10^{3}	1.20 ± 0.07
3.753	2.45×10^{-5}	2.31×10^{-5}	1.01×10^{-5}	8.2×10^{-6}	3.37×10^{-5}	5.29×10^{4}	1.15 ± 0.08
0.000	8.20×10^{-6}					0	n.d.
1.501	1.78×10^{-5}	1.73×10^{-5}	8.10×10^{-6}	8.2×10^{-6}	2.16×10^{-5}	4.52×10^{3}	1.57 ± 0.23
2.801	3.59×10^{-5}	3.56×10^{-5}	1.03×10^{-5}	1.00×10^{-5}	2.95×10^{-5}	1.25×10^{4}	1.26 ± 0.06
2.034	4.62×10^{-5}	4.44×10^{-5}	9.90×10^{-6}	8.2×10^{-6}	3.20×10^{-5}	2.43×10^{3}	1.40 ± 0.12
2.565	1.01×10^{-5}	1.16×10^{-5}	8.00×10^{-6}	8.2×10^{-6}	1.29×10^{-5}	3.74×10^{2}	1.68 ± 0.20
2.140	1.26×10^{-5}	1.29×10^{-5}	8.00×10^{-6}	8.2×10^{-6}	1.42×10^{-5}	5.86×10^{2}	1.69 ± 0.50
1.519	1.21×10^{-5}	1.16×10^{-5}	8.80×10^{-6}	8.2×10^{-6}	1.29×10^{-5}	1.51×10^{3}	1.72 ± 0.51
1.541	1.17×10^{-5}	1.16×10^{-5}	8.00×10^{-6}	8.2×10^{-6}	1.42×10^{-5}	1.75×10^{3}	1.51 ± 0.35
1.890	1.28×10^{-5}	1.29×10^{-5}	8.30×10^{-6}	8.2×10^{-6}	2.16×10^{-5}	2.40×10^{4}	1.39 ± 0.25
2.018	1.26×10^{-5}	1.29×10^{-5}	8.30×10^{-6}	8.2×10^{-6}	1.83×10^{-5}	4.24×10^{4}	1.33 ± 0.22
2.242	1.34×10^{-5}	1.29×10^{-5}	8.60×10^{-6}	8.2×10^{-6}	2.16×10^{-5}	5.73×10^{4}	1.29 ± 0.20
2.833	1.36×10^{-5}	1.29×10^{-5}	8.90×10^{-6}	8.2×10^{-6}	2.83×10^{-5}	9.43×10^{4}	1.21 ± 0.13
4.281	1.46×10^{-5}	1.29×10^{-5}	9.50×10^{-6}	8.2×10^{-6}	2.89×10^{-5}	1.05×10^{5}	1.13 ± 0.07
4.333	1.40×10^{-5}	1.35×10^{-5}	9.80×10^{-6}	8.2×10^{-6}	3.56×10^{-5}	8.68×10^{4}	1.12 ± 0.06
4.384	1.56×10^{-5}	1.42×10^{-5}	9.70×10^{-6}	8.2×10^{-6}	5.04×10^{-5}	8.46×10^{4}	1.10 ± 0.05
4.514	1.65×10^{-5}	1.42×10^{-5}	9.87×10^{-6}	8.2×10^{-6}	3.92×10^{-5}	8.00×10^{4}	1.10 ± 0.05
4.418	2.14×10^{-5}	1.73×10^{-5}	1.06×10^{-5}	1.00×10^{-5}	4.51×10^{-5}	5.17×10^{4}	1.10 ± 0.04

2.266	1.14×10^{-5}	1.16×10^{-5}	7.9×10^{-6}	8.2×10^{-6}	1.64×10^{-5}	6.09×10^{3}	1.48 ± 0.31
6.323	1.36×10^{-5}	1.29×10^{-5}	9.5×10^{-6}	8.2×10^{-6}	3.52×10^{-5}	1.24×10^{5}	1.09 ± 0.06
6.281	1.84×10^{-5}	1.64×10^{-5}	1.09×10^{-5}	1.00×10^{-5}	6.96×10^{-5}	3.25×10^{4}	1.09 ± 0.03
4.285	2.59×10^{-5}	1.73×10^{-5}	1.08×10^{-5}	1.00×10^{-5}	5.60×10^{-5}	1.32×10^{4}	1.13 ± 0.03

lity measurements. See text for discussion

were extracted from time-temperature charts recorded during the experiments.
in ~10 °C, although temperature fluctuations as great as ± 50 °C were sometimes observed (DRB2012-6e-10)
http://melts.ofm-research.org/CORBA_CTserver/Papale/Papale.php

Coordination #	Permeability (m^2)	Vesiculation conditions[7]
4.4 ± 6.8	1.28×10^{-12}	Manual heating to 970 °C, hold 75 s, 1st bubbles: 616 °C
4.3 ± 7.1	3.49×10^{-13}	Re-heating of DRB 2012-07a-2, quenched
5.2 ± 6.8	1.50×10^{-11}	1 °C s^{-1} from 600 to 1150, hold 150 s, 1st vesiculation: 740 °C
6.8 ± 6.2	2.92×10^{-11}	6 °C s^{-1} from 600 to 1150, hold 40 s, 1st vesiculation: 880 °C
		0.8 °C s^{-1} from 600 to 950, hold 150 s, 1st vesiculation: 720 °C
not connected	4.23×10^{-16}	325 s, 860 °C (1 bubble found)
3.8 ± 1.4	3.44×10^{-13}	413 s, 930 °C
5.2 ± 2.2	1.41×10^{-12}	380 s, 980 °C
3.9 ± 1.1	3.23×10^{-12}	471 s, 950 °C
		5 °C s^{-1} from 600 to 1100, hold 15 s, 1st vesiculation: 900 °C
4.0 ± 2.3	2.98×10^{-15}	60s, 900 °C
4.1 ± 3.4	1.35×10^{-14}	77 s, 984 °C
3.8 ± 1.0	1.45×10^{-14}	79 s, 994 °C
3.6 ± 1.4	3.94×10^{-14}	81 s, 1005 °C
4.0 ± 2.4	1.50×10^{-13}	83 s, 1016 °C
4.2 ± 3.1	2.99×10^{-13}	85 s, 1026 °C
4.4 ± 3.8	4.04×10^{-13}	87 s, 1037 °C
5.2 ± 7.8	9.82×10^{-13}	89 s, 1047 °C
5.5 ± 12.3	3.23×10^{-12}	92 s, 1057 °C
5.2 ± 7.1	4.46×10^{-12}	94 s, 1168 °C
6.3 ± 12.7	5.60×10^{-12}	96 s, 1179 °C
6.8 ± 12.7	5.76×10^{-12}	98 s, 1089 °C
7.7 ± 12.7	9.56×10^{-12}	100 s, 1100 °C

		1 °C s^{-1} from 600 to 1150, hold 150 s, 1st vesiculation: 790 °C
4.5 ± 6.8	no results	373 s, 980 °C
4.7 ± 4.6	5.47 x 10^{-12}	446 s, 1050 °C
4.7 ± 5.6	5.29 x 10^{-11}	504 s, 1110 °C
7.0 ± 11.5	3.22 x 10^{-11}	585 s, ~1200 °C

Supplementary Material: Movie of bubble growth

Click here to access/download
Supplementary Material
SupplementaryMovie_DRB2012_2a_Rendering.gif

Supplementary Material: All poree & thoat sizes

Click here to access/download

Supplementary Material

SupplementaryDataPoreAndThroatSizes.xls

Supplementary Figure 1

Click here to access/download
Supplementary Material
SupplementaryFigure1.eps